

Intravascular OCT tissue type imaging by automated optical attenuation analysis

Muthukaruppan Gnanadesigan

The research described in this thesis was supported by a grant of the Dutch Heart Foundation (No. 2010B064)

Financial support by the Dutch Heart Foundation for the publication of this thesis is gratefully acknowledged.

Layout: Legatron Electronic Publishing, Rotterdam, the Netherlands

Printing: Ipskamp Printing, Enschede, the Netherlands

ISBN: 978-94-028-0229-0

Copyright ©2016 by Muthukaruppan Gnanadesigan. All right reserved. No part of this thesis may be reproduced, stored in a retrieval system of any nature, or transmitted in any form or by any means, without prior written permission of the author.

Intravascular OCT tissue type imaging by automated optical attenuation analysis

Intravasculaire Optical Coherence Tomography weefseltype beeldvorming
door geautomatiseerde analyse van de optische verzwakking

Thesis

to obtain the degree of Doctor from the
Erasmus University Rotterdam
by command of the
rector magnificus

Prof.dr. H.A.P. Pols

and in accordance with the decision of the Doctorate Board.

The public defence shall be held on

Friday 17th June 2016 at 11.30 hrs

by

Muthukaruppan Gnanadesigan

Born in Palayamkottai, India

Doctoral Committee

Promotor(s): Prof.dr. ir. A.F.W. van der Steen

Other members: Dr. E.S. Regar
Prof.dr. A.G.J.M. van Leeuwen
Dr. T.W. Johnson

Copromotor(s): Dr. G. van Soest

Contents

Chapter 1	Introduction	7
Chapter 2	Effect of temperature and fixation on the optical properties of atherosclerotic tissue: a validation study of an ex-vivo whole heart cadaveric model	19
Chapter 3	Optical coherence tomography attenuation imaging for lipid core detection: an ex-vivo validation study	35
Chapter 4	Automated characterization of lipid-core plaques in vivo by quantitative optical coherence tomography tissue type imaging	47
Chapter 5	Qualitative comparison of automated tissue characterization methods in intravascular optical coherence tomography ex-vivo	65
Chapter 6	OCT Assessment of the Long-Term Vascular Healing Response 5 Years After Everolimus-Eluting Bioresorbable Vascular Scaffold	77
Chapter 7	Qualitative and quantitative evaluation of dynamic changes in non-culprit coronary atherosclerotic lesion morphology. A longitudinal OCT study	101
Chapter 8	OCT-measured plaque free wall angle is indicative for plaque burden: overcoming the main limitation of OCT?1	121
Chapter 9	General discussion	131
	Summary	141
	Samenvatting	143
	Acknowledgements	145
	Curriculum Vitae	147
	Publications	149
	PhD Portfolio	151

Chapter 1

Introduction

According to World Health Organization, cardiovascular disease is the leading global cause of death, accounting for 17.3 million deaths per year, a number that is expected to grow to more than 23.6 million by 2030. Of these deaths, an estimated 7.4 million were due to coronary heart disease. Acute coronary syndrome (ACS) is a sudden and severe heart condition that may lead to death [1]. It is usually the manifestation of coronary atherosclerosis, a systemic inflammatory disease causing the formation of plaques [2,3]. ACS is usually associated with the thrombus formation as a result of the rupture of a lipid-core lesion [3,4]. Previous studies have shown that 60% of the thrombi associated with the acute coronary events had a ruptured thin cap fibroatheroma (TCFA) as their substrate [3]. The TCFA are typically characterized by a large necrotic core with a thin cap, probably infiltrated by macrophages [5]. The combination of the inflammation due to the macrophage infiltration and the mechanical strain in the TCFA make them unstable or 'vulnerable' plaque prone to rupture [6-8]. Early detection of these high risk plaques may have important clinical impact on the prevention of acute cardiac events.

Percutaneous coronary intervention (PCI) also known as coronary angioplasty, is an effective non-surgical procedure for treating severe coronary artery disease. It is a minimally invasive method that is done using x-ray angiographic guidance. The procedure involves introduction of a steerable guide wire into coronary artery and across the stenosis through the femoral, radial or brachial arteries. The balloon or stent catheter is passed over it and the lesion dilated and/or stented. Figure 1.1 shows the procedure and an example frame from angiography.

Traditionally coronary angiography has been the tool for morphological assessment in stent placements. The drawback of angiography is that it can only measure the luminal stenosis which may be the result of a rupture but do not visualize the vessel wall where the atherosclerosis, the cause of the disease, may exist. It does not visualize, therefore, the lipid core plaques which have important implications during intervention, as incomplete coverage of them by stent could lead to immediate or long-term complications [9-13]. Also the measurements can be ambiguous at times due to the projection and low resolution.

1.1 | Intravascular imaging

Intravascular imaging techniques have emerged as useful clinical morphological tools. Intravascular ultrasound (IVUS), intravascular optical coherence tomography (IV-OCT), intravascular photoacoustics (IVPA) and coronary angioscopy are few intravascular imaging tools. These are catheter based techniques that provides a tomographic view from inside the lumen. Some of them have also been tried to extend their usability by adding diagnostic values like tissue composition information. IVUS-Virtual histology (VH), IVUS palpography, coronary angioscopy, near-infrared spectroscopy (NIRS) with IVUS, spectroscopic IVPA and OCT attenuation imaging have been studied for potential intravascular diagnostic imaging [14-18]. Few of the intravascular imaging techniques are described below.

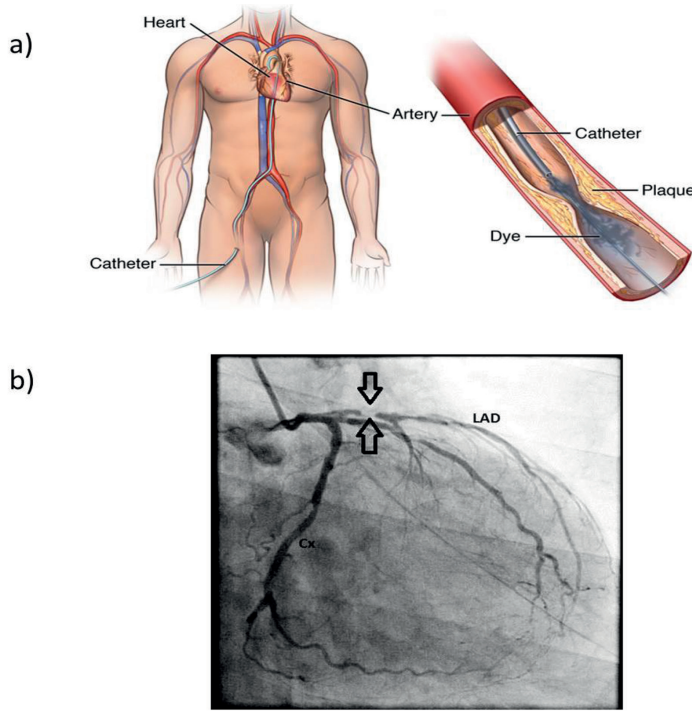


Figure 1.1 | a) The cartoon depicts the PCI procedure (Source: medifitbiologicals.com) b) A frame from angiography showing a high risk stenosis in the left anterior descending artery.

1.1.1 | Intravascular Ultrasound

Ultrasound images are formed by electrically exciting a piezoelectric transducer, which expands and contracts to produce sound waves. The backscattered ultrasound energy from the tissue is received by the transducer which produces electrical signals that is converted into the image [19]. In intravascular ultrasound imaging a high frequency ultrasound transducer is placed on the tip of a catheter which is directly inserted into the blood vessel to obtain reproducible and high resolution images. Typical resolution of a 20 to 40 MHz IVUS transducer is 80 microns axially and 200 to 250 microns laterally.

1.1.2 | Near-infrared spectroscopy

Near-infrared spectroscopy (NIRS) uses spectral signature to determine the chemical composition of substances. Spectroscopic assessment of the arterial plaque by NIRS has the potential to identify Lipid core plaque (LCP) in patients. In the commercial system NIRS is combined with IVUS for morphological information. The NIRS-IVUS images are acquired using a hybrid optical/ultrasound catheter [16,20]. The instrument performs approximately 8000 chemical measurements per 100 mm of artery scanned. An automated pullback (0.5 mm/sec and 16 frames per second (fps)) acquires co-registered images of measured probability of LCP presence by NIRS, displayed as a color-coded ring (yellow is high probability, red is low), and gray-scale IVUS. The measurement of the probability of LCP for each scanned arterial segment is displayed as a map, with the x-axis indicating the pullback position in millimeters and the y-axis the circumferential position of the measurement in degrees.

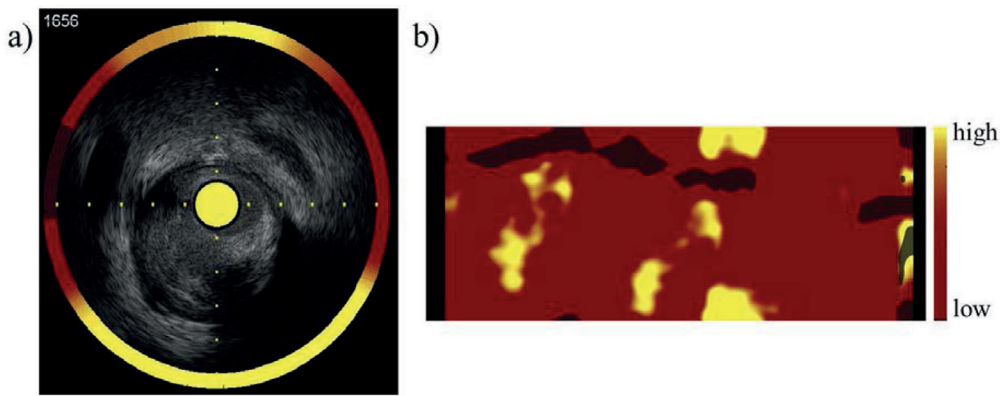


Figure 1.2 | a) A cross section image of an artery by NIRS-IVUS depicting the probability of the presence of lipid as a ring around the gray scale IVUS b) The “chemogram” depicting the probability of lipid in the entire vessel.

1.1.3 | Intravascular Optical Coherence tomography

Intravascular OCT is gaining popularity as the clinical tool for stent assessment and optimization. OCT is technique that uses infrared light to provide high resolution images of the artery wall and implanted stents [21-23]. The imaging is catheter based, so the free lumen is seen as opposed to a projection in angiography and the landing zones for the stents can be better assessed. This is important information in image guided intervention for better results and future outcomes. Also a recent study suggests that OCT guided PCIs have significantly better outcome than those done with angiographic guidance alone [24,25].

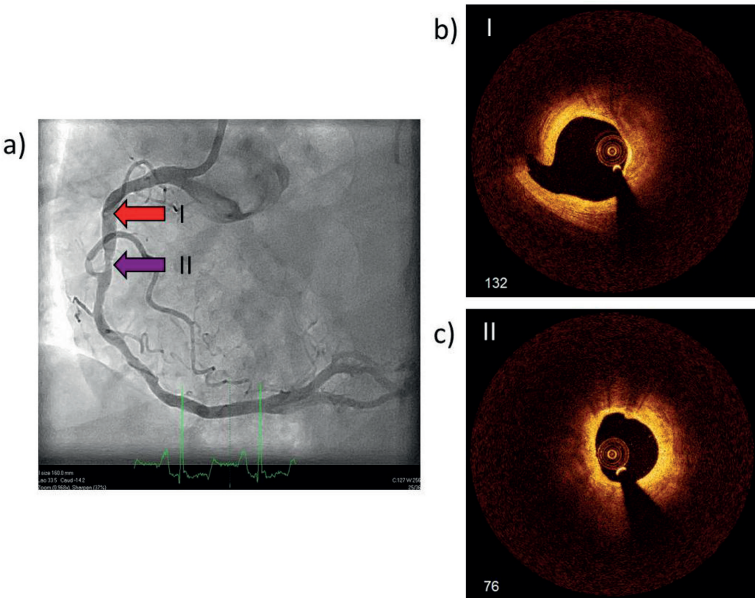


Figure 1.3 | a) An angiographic image showing a section with a sidebranch (I) and a section with stenosis (II) (b&c) corresponding OCT image of the sections (I&II) showing the tomographic view.

1.1.3.1 | Principle

OCT is a low coherence interferometric technique where images are formed as a result of an interference pattern of the reflected light from a reference and sample arm, illustrated in Figure 1.4. When the first generation of OCT (using time-domain scanning) was first demonstrated in the early 90s, the reference arm was moved mechanically. In one dimensional tissue scattering model, the spatial extent of temporal coherence function of the source determines the axial width of the point-spread function therefore, the coherence length is an appropriate measure of the axial resolution of the OCT system [26]. Later the mechanical scanning was replaced by frequency scanning using a swept source laser in the next generation frequency domain system (FD-OCT) [27-29]. These FD OCT systems have a much improved imaging speed and signal to noise ratio [30,31]. IV-OCT uses a single mode fiber in a catheter in the sample arm, the light from which is reflected towards the arterial wall by a prism or mirror. The backscattered light from the tissue results in an A-line that represents the depth-resolved reflectivity profile of the tissue components. When the optical fiber in the catheter is rotated a complete image scan of the artery is obtained and this when combined with a pullback of the fiber results in a volumetric scan of the artery.

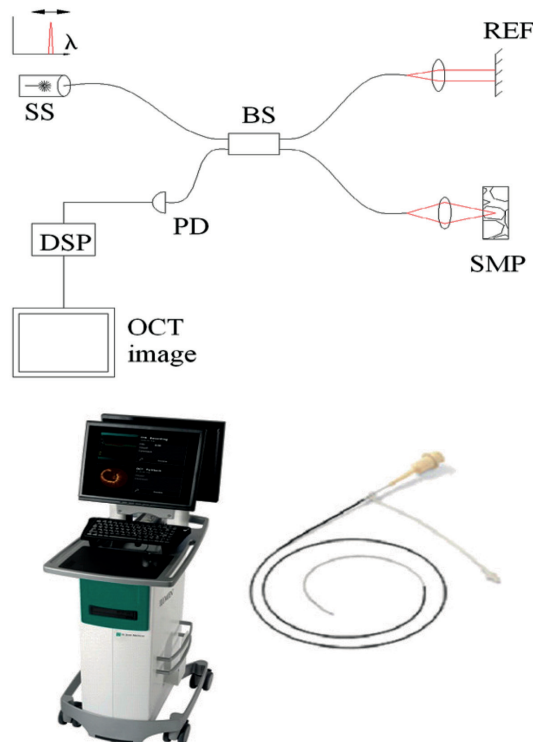


Figure 1.4 | Swept source OCT principle and a typical commercial OCT system and catheter (www.sjm.com). SS-swept source, BS-beam splitter, REF-reference mirror, SMP-sample, PD-photodetector, DSP-digital signal processing

The axial resolution of OCT depends on the sweeping length of the laser source. Typically the axial resolution is around $10\text{ }\mu\text{m}$. The transverse resolution is based on the spot size of the laser beam at the focal point and is typically it is $\sim 30\text{ }\mu\text{m}$. The frame pitch or the frame spacing of OCT is about $200\text{ }\mu\text{m}$. During interventions, the artery to be imaged has to be flushed with a clear medium as the blood highly attenuates light. Usually a contrast medium is used for flushing and the pullback is done at the speed of 20 mm/sec .

1.1.3.2 | Potential uses

Currently OCT is used extensively for guidance in stent implantation. It can provide accurate lumen measurements at the stenosis, the measurements in the proximal and distal landing zones and the segment to be stented. The high-resolution images of the arterial wall allows for qualitative interpretation of its composition [32-35]. This can help in the preventing the incomplete coverage of the lipid core plaques as discussed above [36]. Figure 1.5 shows OCT images of a few cross sections of the artery and the annotations show the qualitative interpretation based on the consensus standard.

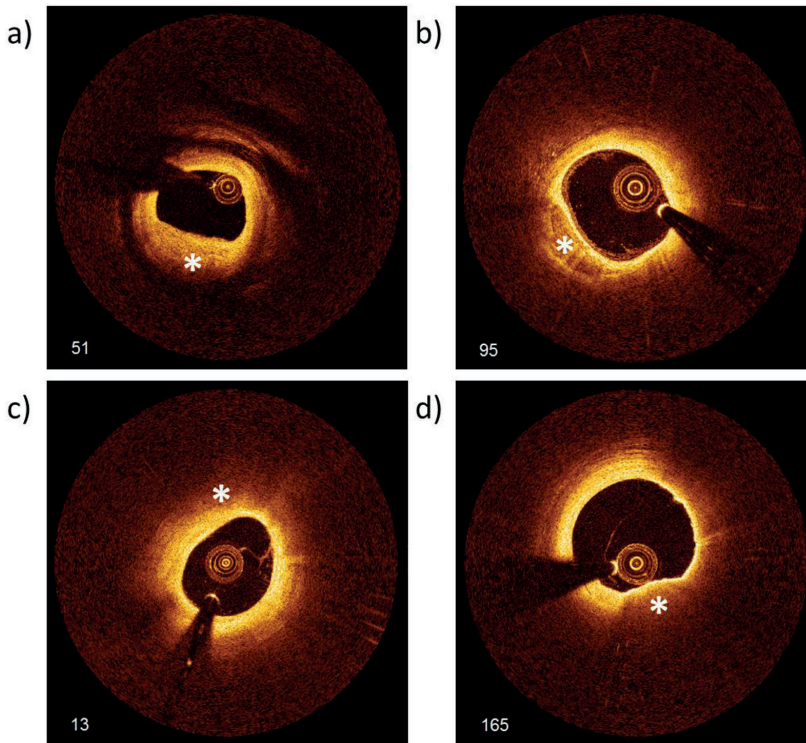


Figure 1.5 | a) OCT cross-section with a fibrotic plaque marked by *. The fibrous plaques have low attenuation coefficients and high backscattering properties. b) An OCT frame with a chunk of calcium denoted by the marker. They are usually exhibit low attenuation and low backscattering properties. c) A OCT cross-section with fibroatheroma (thick cap) as shown by the marker. The lipid content and possible necrosis results in high attenuation and low backscattering. d) A OCT image with a Thin-cap fibroatheroma (TCFA) as shown by the marker. These unstable plaques have characteristic very high backscattering superficially followed by very high attenuation owing to the lipid, necrosis content and the macrophage infiltration.

OCT can be a more useful and easy diagnostic tool if the qualitative tissue characterization can be quantified and made simple to read. Parametric imaging of the attenuation can be a useful tool to achieve that. The increase in popularity of OCT in stent implantations and increase in the usage of the recently introduced bioresorbable vascular scaffolds which warrants the use of OCT for optimal placement, means adding diagnostic value to OCT is a very effective way to proceed.

1.1.3.3 | Parametric imaging

The qualitative interpretations of plaque type are based on the appearance of the tissue constituents and their interaction with light. Different tissue types depict different optical properties and these properties can be quantified from the OCT images. The quantification of OCT-derived tissue optical properties has been proposed to automate tissue characterization. One of the optical properties that can be derived is the attenuation coefficient of a tissue type. Different tissue types attenuate light to different degree and the attenuation coefficient is a robust tissue optical parameter that can be used for tissue characterization or at the least support image interpretation [18,37-39]. Such analyses have recently been augmented with statistical image metrics to achieve tissue identification [40].

The expected value of the backscattered signal of OCT can be modeled using a single scattering model [41]. This model describes the signal as Beer-Lambert decay multiplied by coupling factor i.e. the longitudinal point spread function (PSF) for a single mode fiber (SMF) and a Gaussian coherence function to account for the signal roll off eqn 1-3.

$$\langle I_d(r) \rangle = I_0 t(r) \hat{S}(r) e^{(-\mu_t r)}, \quad (1)$$

$$T(r) = \left[\left(\frac{r-z_0}{z_R} \right)^2 + 1 \right]^{-\frac{1}{2}}, \quad (2)$$

$$\hat{S}(r) = e^{-\left(\frac{r-z_c}{z_c} \right)^2}. \quad (3)$$

where $\langle I_d(r) \rangle$ is the expected value for the detected OCT signal. $T(r)$ is the point spread function for the SMF based OCT system, and $\hat{S}(r)$ describes the signal roll off with depth [42]. The important parameter to be extracted is μ_t which is the optical attenuation coefficient [18]. When eq. 1 is linearized by logarithmic compression, it yields

$$\log[\langle I_d(r) \rangle] - \log[T(r)] - \log[\hat{S}(r)] = \log(I_0) - \mu_t r \quad (4)$$

The log compressed OCT intensity data from the measurement can be fitted in the above model. If the left hand side of eq. 4, the log compressed data compensated for the roll off and point spread function, can be denoted as i_d then it can be least-squares fitted with a linear model eq. 5,

$$i(r) = \log(I_0) - \mu_t r, \quad (5)$$

The attenuation coefficient μ_t can be extracted from data by fitting them in the model in a window of variable length. The optimization of the fitting determines the window length for preserving homogeneity. This is a fast, reliable and robust method for parametric imaging. Such an attenuation image overlaid on the grayscale OCT image is shown in Figure 1.6.

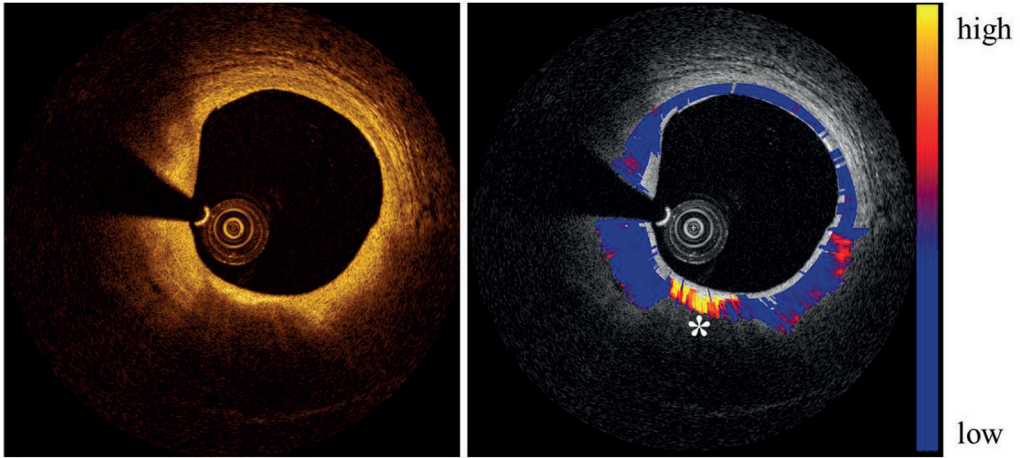


Figure 1.6 | An OCT cross sectional image (left) and its corresponding attenuation image (right) derived from the model. The marker denotes a fibroatheromatic plaque with inflammation which has high attenuation as expected. The colorbar shows the low to high attenuation colors.

There have been studies using different approaches other than the attenuation coefficient for tissue characterization some of which are automatic and others semi-automatic. An automatic classification using texture analysis, automatic thresholding and classification algorithm has been demonstrated [43]. Correlating the bright spots to macrophages and using normalized standard deviation for macrophage quantification has been studied [44,45]. Also a semi-automatic segmentation and quantification of calcified plaques was shown before [46].

Plaques with a lipid-rich necrotic core are generally considered to be high-risk lesions, and may require special care in planning or performing PCI. Such plaques with macrophage infiltration usually exhibit high attenuation compared to calcium or fibrous tissue types [17]. Identifying these fibroatherotic plaques is an important aim for tissue characterization and if possible to distinguish thin and thick cap fibroatheromas, which could be clinically relevant. The parametric imaging can be a very useful tool if it can be demonstrated to be reliable predictor of the presence of unstable TCFAs.

1.2 | Thesis outlines

A quantitative measurement of IV-OCT can be a potential tool for atherosclerotic tissue characterization. We propose the tissue dependent parameter of OCT, the attenuation coefficient, as the quantitative measure for tissue characterization. In this thesis we did ex and in-vivo validation of attenuation imaging as a tissue characterization tool and demonstrated some of its clinical research utilities.

Chapter 2 shows the study of the effects of temperature and fixation on the attenuation coefficients of the ex-vivo tissues. The developed en-face maps of attenuation of the arteries at different conditions were systematically compared.

Chapter 3 describes the IPA, a bias free and reproducible summary measurement of attenuation, as a lipid core detection tool. The IPA was qualitatively assessed for the sensitivity of lipid and was compared against the manual lipid score in OCT images.

Chapter 4 describes the clinical study aimed to validate the attenuation imaging as a plaque characterization tool in-vivo. The quantitative attenuation measure, the IPA, was compared against LCBI of near infra-red spectroscopy for detecting lipid. The ability to differentiate thin and thick cap fibroatheroma was demonstrated which can be a potential clinical utility.

Chapter 5 describes a qualitative comparative study of some of the available methods of tissue characterization in OCT. The different algorithms were performed on a set of ex-vivo data. The value of each method to the atherosclerotic tissue characterization is demonstrated.

Chapter 6 presents the first in-vivo long term OCT data after 5 years of implantation. The long-term vascular response was studied and the attenuation imaging depicts the newly formed adluminal sealing layer formed by the plaque underneath the disappeared struts.

Chapter 7 describes the study to evaluate dynamic changes of coronary atherosclerosis under standard medical therapy. A comprehensive patient-level and segment-level analysis of non-culprit lesions were done. The automated attenuation analysis was used to study objectively the plaque morphology.

Chapter 8 presents the study to evaluate the relationship between plaque free wall measured in OCT and the plaque burden measured in IVUS. The ability of OCT as morphological and diagnostic tool is demonstrated.

Chapter 9 summarizes the main findings of the thesis and their potential clinical implications.

References

1. Falk E, Shah PK, Fuster V. Coronary plaque disruption. *Circulation* 1995;92:657-71.
2. Schaar JA, Muller JE, Falk E et al. Terminology for high-risk and vulnerable coronary artery plaques. Report of a meeting on the vulnerable plaque, June 17 and 18, 2003, Santorini, Greece. *Eur Heart J* 2004;25:1077-82.
3. Virmani R, Kolodgie FD, Burke AP, Farb A, Schwartz SM. Lessons from sudden coronary death: a comprehensive morphological classification scheme for atherosclerotic lesions. *Arterioscler Thromb Vasc Biol* 2000;20:1262-75.
4. Burke AP, Farb A, Malcom GT, Liang YH, Smialek J, Virmani R. Coronary risk factors and plaque morphology in men with coronary disease who died suddenly. *N Engl J Med* 1997;336:1276-82.
5. Kolodgie FD, Burke AP, Farb A et al. The thin-cap fibroatheroma: a type of vulnerable plaque: the major precursor lesion to acute coronary syndromes. *Curr Opin Cardiol* 2001;16:285-92.
6. Kolodgie FD, Narula J, Burke AP et al. Localization of apoptotic macrophages at the site of plaque rupture in sudden coronary death. *Am J Pathol* 2000;157:1259-68.
7. Loree HM, Kamm RD, Stringfellow RG, Lee RT. Effects of fibrous cap thickness on peak circumferential stress in model atherosclerotic vessels. *Circ Res* 1992;71:850-8.
8. Richardson PD, Davies MJ, Born GV. Influence of plaque configuration and stress distribution on fissuring of coronary atherosclerotic plaques. *Lancet* 1989;2:941-4.
9. Waxman S, Freilich MI, Suter MJ et al. A case of lipid core plaque progression and rupture at the edge of a coronary stent: elucidating the mechanisms of drug-eluting stent failure. *Circ Cardiovasc Interv* 2010;3:193-6.
10. Goldstein JA, Grines C, Fischell T et al. Coronary embolization following balloon dilation of lipid-core plaques. *JACC Cardiovasc Imaging* 2009;2:1420-4.
11. Goldstein JA, Maini B, Dixon SR et al. Detection of lipid-core plaques by intracoronary near-infrared spectroscopy identifies high risk of periprocedural myocardial infarction. *Circ Cardiovasc Interv* 2011;4:429-37.
12. Tanaka A, Imanishi T, Kitabata H et al. Lipid-rich plaque and myocardial perfusion after successful stenting in patients with non-ST-segment elevation acute coronary syndrome: an optical coherence tomography study. *Eur Heart J* 2009;30:1348-55.
13. Kini AS, Motoyama S, Vengrenyuk Y et al. Multimodality Intravascular Imaging to Predict Periprocedural Myocardial Infarction During Percutaneous Coronary Intervention. *JACC Cardiovasc Interv* 2015;8:937-45.
14. Nasu K, Tsuchikane E, Katoh O et al. Accuracy of in vivo coronary plaque morphology assessment: a validation study of in vivo virtual histology compared with in vitro histopathology. *J Am Coll Cardiol* 2006;47:2405-12.
15. Ueda Y, Ohtani T, Shimizu M, Hirayama A, Kodama K. Assessment of plaque vulnerability by angioscopic classification of plaque color. *Am Heart J* 2004;148:333-5.
16. Waxman S, Dixon SR, L'Allier P et al. In vivo validation of a catheter-based near-infrared spectroscopy system for detection of lipid core coronary plaques: initial results of the SPECTACL study. *JACC Cardiovasc Imaging* 2009;2:858-68.
17. Jansen K, van der Steen AF, Wu M et al. Spectroscopic intravascular photoacoustic imaging of lipids in atherosclerosis. *J Biomed Opt* 2014;19:026006.
18. van der Meer FJ, Faber DJ, Baraznji Sassoon DM, Aalders MC, Pasterkamp G, van Leeuwen TG. Localized measurement of optical attenuation coefficients of atherosclerotic plaque constituents by quantitative optical coherence tomography. *IEEE Trans Med Imaging* 2005;24:1369-76.
19. Mintz GS, Nissen SE, Anderson WD et al. American College of Cardiology Clinical Expert Consensus Document on Standards for Acquisition, Measurement and Reporting of Intravascular Ultrasound Studies (IVUS). A report of the American College of Cardiology Task Force on Clinical Expert Consensus Documents. *J Am Coll Cardiol* 2001;37:1478-92.
20. Gardner CM, Tan H, Hull EL et al. Detection of lipid core coronary plaques in autopsy specimens with a novel catheter-based near-infrared spectroscopy system. *JACC Cardiovasc Imaging* 2008;1:638-48.
21. Tearney GJ, Boppart SA, Bouma BE et al. Scanning single-mode fiber optic catheter-endoscope for optical coherence tomography. *Opt Lett* 1996;21:543-5.
22. Tearney GJ, Brezinski ME, Boppart SA et al. Images in cardiovascular medicine. Catheter-based optical imaging of a human coronary artery. *Circulation* 1996;94:3013.

23. Tearney GJ, Brezinski ME, Bouma BE et al. In vivo endoscopic optical biopsy with optical coherence tomography. *Science* 1997;276:2037-9.
24. Prati F, Di Vito L, Biondi-Zoccai G et al. Angiography alone versus angiography plus optical coherence tomography to guide decision-making during percutaneous coronary intervention: the Centro per la Lotta contro l'Infarto-Optimisation of Percutaneous Coronary Intervention (CLI-OPCI) study. *EuroIntervention* 2012;8:823-9.
25. Prati F, Romagnoli E, Burzotta F et al. Clinical Impact of OCT Findings During PCI: The CLI-OPCI II Study. *JACC Cardiovasc Imaging* 2015;8:1297-305.
26. Schmitt JM. Optical coherence tomography (OCT): A review. *Ieee J Sel Top Quant* 1999;5:1205-1215.
27. Chinn SR, Swanson EA, Fujimoto JG. Optical coherence tomography using a frequency-tunable optical source. *Opt Lett* 1997;22:340-2.
28. Golubovic B, Bouma BE, Tearney GJ, Fujimoto JG. Optical frequency-domain reflectometry using rapid wavelength tuning of a Cr4+:forsterite laser. *Opt Lett* 1997;22:1704-6.
29. Yun S, Tearney G, de Boer J, Ifimia N, Bouma B. High-speed optical frequency-domain imaging. *Opt Express* 2003;11:2953-63.
30. Choma M, Sarunic M, Yang C, Izatt J. Sensitivity advantage of swept source and Fourier domain optical coherence tomography. *Opt Express* 2003;11:2183-9.
31. de Boer JF, Cense B, Park BH, Pierce MC, Tearney GJ, Bouma BE. Improved signal-to-noise ratio in spectral-domain compared with time-domain optical coherence tomography. *Opt Lett* 2003;28:2067-9.
32. Regar E, Ligthart J, Bruining N, van Soest G. The diagnostic value of intracoronary optical coherence tomography. *Herz* 2011;36:417-428.
33. Tearney GJ, Regar E, Akasaka T et al. Consensus standards for acquisition, measurement, and reporting of intravascular optical coherence tomography studies: a report from the International Working Group for Intravascular Optical Coherence Tomography Standardization and Validation. *J Am Coll Cardiol* 2012;59:1058-72.
34. Yabushita H, Bouma BE, Houser SL et al. Characterization of human atherosclerosis by optical coherence tomography. *Circulation* 2002;106:1640-5.
35. Kume T, Akasaka T, Kawamoto T et al. Assessment of coronary arterial plaque by optical coherence tomography. *Am J Cardiol* 2006;97:1172-5.
36. Guagliumi G, Costa MA, Sirbu V et al. Strut coverage and late malapposition with paclitaxel-eluting stents compared with bare metal stents in acute myocardial infarction: optical coherence tomography substudy of the Harmonizing Outcomes with Revascularization and Stents in Acute Myocardial Infarction (HORIZONS-AMI) Trial. *Circulation* 2011;123:274-81.
37. Levitz D, Thrane L, Frosz M et al. Determination of optical scattering properties of highly-scattering media in optical coherence tomography images. *Opt Express* 2004;12:249-59.
38. van Soest G, Goderie T, Regar E et al. Atherosclerotic tissue characterization in vivo by optical coherence tomography attenuation imaging. *J Biomed Opt* 2010;15:011105.
39. Xu C, Schmitt JM, Carlier SG, Virmani R. Characterization of atherosclerosis plaques by measuring both backscattering and attenuation coefficients in optical coherence tomography. *J Biomed Opt* 2008;13:034003.
40. Ughi GJ, Adriaenssens T, Sinnaeve P, Desmet W, D'Hooge J. Automated tissue characterization of in vivo atherosclerotic plaques by intravascular optical coherence tomography images. *Biomed Opt Express* 2013;4:1014-30.
41. van Leeuwen TG, Faber DJ, Aalders MC. Measurement of the axial point spread function in scattering media using single-mode fiber-based optical coherence tomography. *Ieee J Sel Top Quant* 2003;9:227-233.
42. Leitgeb R, Hitznberger CK, Fercher AF. Performance of fourier domain vs. time domain optical coherence tomography. *Optics Express* 2003;11:889-894.
43. Athanasiou LS, Bourantas CV, Rigas G et al. Methodology for fully automated segmentation and plaque characterization in intracoronary optical coherence tomography images. *J Biomed Opt* 2014;19:026009.
44. Phipps JE, Vela D, Hoyt T et al. Macrophages and intravascular OCT bright spots: a quantitative study. *JACC Cardiovasc Imaging* 2015;8:63-72.

45. Tearney GJ, Yabushita H, Houser SL et al. Quantification of macrophage content in atherosclerotic plaques by optical coherence tomography. *Circulation* 2003;107:113-9.
46. Wang Z, Kyono H, Bezerra HG et al. Semiautomatic segmentation and quantification of calcified plaques in intracoronary optical coherence tomography images. *J Biomed Opt* 2010;15:061711.

Chapter 2

Effect of temperature and fixation on the optical properties of atherosclerotic tissue: a validation study of an ex-vivo whole heart cadaveric model

Muthukaruppan Gnanadesigan, Gijs van Soest, Stephen White, Simon Scoltock, Giovanni J Ughi, Andreas Baumbach, Antonius FW van der Steen, Evelyn Regar, and Thomas W Johnson

Biomed Opt Express 5, 1038-1049 (2014).

Abstract

Atherosclerotic plaque composition can be imaged using the optical attenuation coefficient derived from intravascular optical coherence tomography (OCT) data. The relation between optical properties and tissue type has been established on autopsy tissues. In this study, we validate an ex-vivo model for the effect of temperature and tissue fixation on optical parameters. We studied the optical attenuation of human coronary arteries at three temperatures, before and after formalin fixation. We developed an en-face longitudinal display of attenuation data of the OCT pullbacks. Using the unfixed, body-temperature condition image as a standard, and after extensive registration with other condition images, we quantify the differences in optical attenuation and the backscattered intensity. The results suggest that tissue fixation and temperature do not introduce systematic errors in studies of arterial optical properties.

2.1 | Introduction

Ischemic heart disease is a major cause of death globally and rupture of vulnerable atherosclerotic plaques, precipitating myocardial infarction, is the largest contributor to the phenomenon [1]. A vulnerable plaque commonly consists of a lipid-rich necrotic core contained by a fragile layer of fibrous tissue that can be compromised by inflammation and mechanical forces [2]. Release of the necrotic material into the bloodstream may cause thrombus formation leading to a myocardial infarction. Hence, the tissue composition of the plaque is an important predictor of its vulnerability [3]. Likewise, the presence of a lipid-core in a plaque may have an adverse effect on outcome of coronary interventions [4-6]. Intravascular optical coherence tomography (OCT) is gaining widespread use in the interventional cardiology community for guidance of stent placement and optimization [7-10]. OCT facilitates high resolution imaging of the atherosclerotic plaque and tissue components can be distinguished to ascertain plaque composition [8,11,12]. The contrast of tissue types derives from differences in optical properties of the tissues in the artery wall, which can be quantified for tissue characterization in OCT images. The attenuation coefficient has been a popular metric to achieve this [13,14]: necrotic core and inflammation, associated with plaque vulnerability, have high attenuation compared to fibrous and calcified tissues [15]. This finding is currently being clinically validated and appears to be robust in vivo [16]. The analysis has recently been augmented with statistical image metrics to achieve better specificity [17].

Validation of tissue characterization requires comparison of the optical attenuation against histological analysis of atherosclerotic tissue specimens; currently this can only be achieved using ex-vivo models. For ease of processing and analysis ex-vivo specimens of atherosclerotic tissue are commonly dissected from the myocardium, fixed with formalin and kept at low temperature for preservation. The effects of such processing on the acoustic properties of tissue have been studied extensively [18-23]. The knowledge of effects of such processing on tissue optics in the artery wall however is very scarce [24]. In comparison with in-vivo assessment of optical attenuation, refrigeration and fixation of tissue may significantly alter the optical attenuation characteristics of lipid and cellular components of atherosclerotic plaque. Assessment of the impact of temperature and fixation on the optical attenuation of atherosclerotic tissue is necessary to validate our ex-vivo whole heart cadaveric model, thereby facilitating translation into the clinical arena.

The assessment of the effect of temperature and fixation on optical attenuation requires co-registration of multiple OCT attenuation datasets, across varying conditions. It is important to recognize that accurate co-registration of OCT images is limited by a number of factors. Firstly, the helical rotation of the imaging probe during an OCT pullback combined with a narrow lateral width of imaging results in longitudinal under-sampling [25]. Furthermore, non-uniform rotation of the catheter, catheter movement and anatomical distortion can lead to misalignment of datasets.

The aim of this study is to assess the effect of temperature and fixation on optical attenuation in an ex-vivo whole heart cadaveric model, thereby facilitating development of a novel method of intra-vascular OCT tissue characterization.

2.2 | Materials and methods

2.2.1 | Tissue handling and imaging procedure

The ex-vivo model we used consists of a whole heart cadaveric specimen obtained from the Valve Bank of West-England within 48 hrs from post-mortem and stored at or below 4°C [26]. The heart specimen was mounted in a set up as shown in Figure 2.1. A short guide catheter was introduced into the right coronary artery and fixed in position with sutures. All tissues were handled in accordance with the local ethics regulations. The cadaveric specimen is held within a purpose-built Perspex container, with adaptors on both sides of the container's lid allowing connection of the guide catheter internally, and a Y-connector and pressure/injector manifold externally.

The OCT system used for imaging was a C7-XR with Dragonfly catheter (St. Jude Medical Inc. St. Paul, MN, USA). Pullback OCT imaging of one of the three major coronary arteries was performed at a pullback speed of 20 mm/s. The end of the guide catheter served as a reference point to relate the different pullback data sets longitudinally.

Three different temperature conditions were induced in the vessel by flushing with phosphate buffered saline (PBS) solution at 4°C, 20°C, and 37°C, resulting in tissue temperatures of 5-8°C (cold), 18-21°C (room temperature) and 35-37°C (body temperature). A needle-probe thermometer (Water resistant thermometer, Traceable®, VWR International, LLC) was inserted into the peri-adventitial tissue of the coronary artery and imaging was delayed until steady state temperature was achieved. During imaging, intracoronary pressure was maintained at 100 mmHg. OCT imaging was undertaken at these three temperatures. Subsequently, the tissues were pressure fixed with buffered formalin at 100 mmHg for 15 minutes, preserving vessel morphology, and typically 500 ml of formalin was perfused into the heart, which was left in situ overnight at 4°C. The next day, a new temperature series was collected in the fixed tissue, creating a dataset of 6 different conditions. A total of 6 coronary arteries were imaged for the study.

After imaging the formalin fixed series, the study vessel was excised from the heart, fixed for a further 24 hours, embedded in paraffin, and cut into 4-mm blocks. The end of the guide catheter served as a reference. The end face of each block is serially sectioned into slices of 3 µm thickness and stained for histologic analysis. In case of extensive disease seen on OCT, serial sections through the entire tissue block are generated. OCT data were matched to the histology cross-sections based on longitudinal position and general anatomy (side branches and presence of plaque).

In the description of the results in this paper we will adopt the following labels: data acquired on unfixed tissues will be designated by “U”; on fixed tissues by “F”. The temperatures will be indicated by “C” for cold, “R” for room, and “B” for body temperature. For example, our base condition of unfixed tissue at 37°C will be referred to as “UB”.

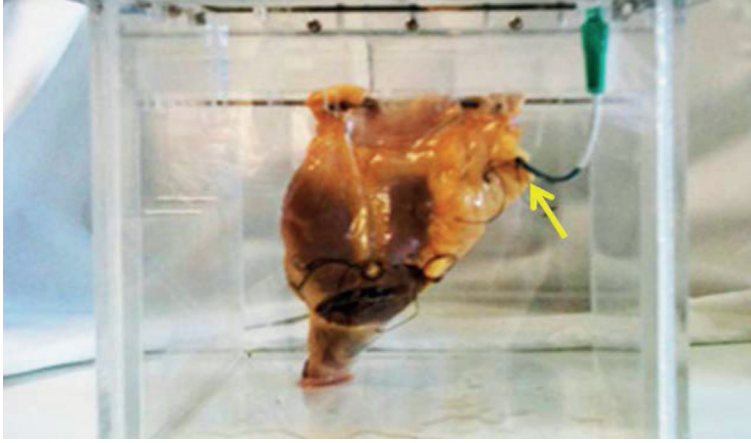


Figure 2.1 | Whole heart cadaveric model; the arrow points to the guide catheter that is fixed in the study vessel.

2.2.2 | Parameter extraction

The OCT images are then analyzed, to quantify the attenuation exhibited by the tissues. We derive the attenuation co-efficient from the OCT signal by fitting a single scattering model [15]:

$$\langle I_d \rangle = T(r) \cdot S(r) \cdot I_0 \cdot e^{-\mu_t r} \quad (1)$$

where $T(r)$ is the point spread function of the catheter [27], $S(r)$ is the signal roll-off, and the parameter of interest is μ_t , the attenuation coefficient. The attenuation calculation and the model implementation were done in Matlab Release 2012b (The Mathworks, Inc., Natick, MA, USA). The model is fitted in the polar image, in every A-line starting from the edge of the lumen [15,28], in small windows of varying length to extract the attenuation coefficients. The accuracy of the extracted μ_t is approximately 1 mm^{-1} [15]. The data analysis results in an attenuation image per cross section of the pullback.

2.2.3 | Image formation and registration

In every vessel in the study, attenuation data sets are generated in six different conditions, resulting in six data sets that need to be registered for comparison. As a first step, the variation in the angle of view of a structure due to the different positioning of the catheter in different pullbacks should be compensated.

To do so, the polar attenuation image is converted to the Cartesian domain, the center of the image is shifted from the catheter to the centroid of the lumen, and the image is converted back to the polar domain relative to the new image center. Figure 2.2 depicts the OCT and the attenuation images with the lumen border, the centroid and the corresponding polar image before and after the origin shift.

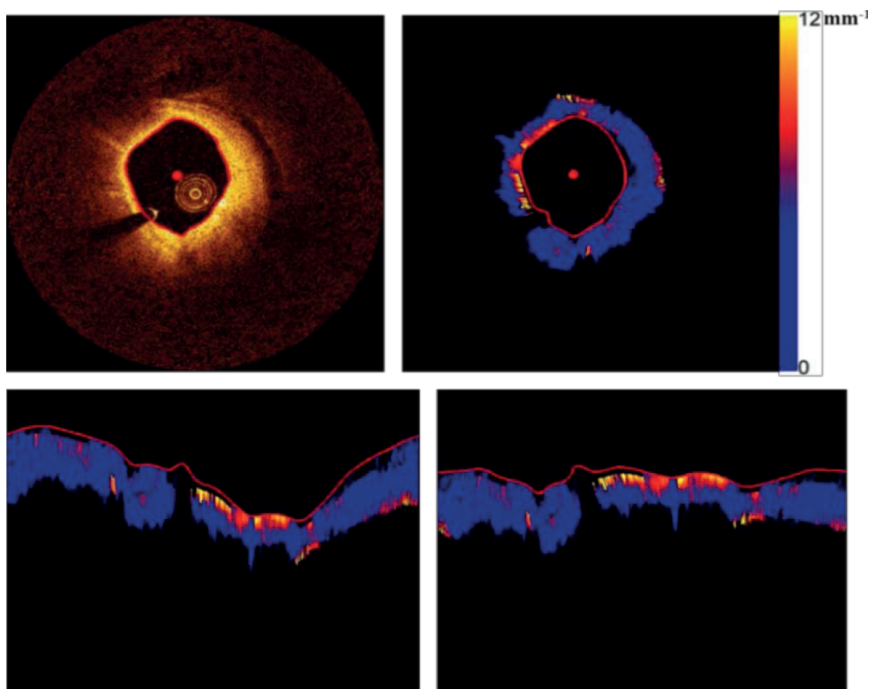


Figure 2.2 | Top left and right: OCT and attenuation images with lumen border and the centroid. Bottom left and right: Polar image before and after the shift of origin.

In the next step, we make a longitudinal attenuation map of the vessel. This mapping display of OCT attenuation depicts tissue optical properties in the entire pullback, sampling a user specified depth window from the lumen border, which at different conditions can be compared to quantify any difference. Such a map image is shown in Figure 2.3.

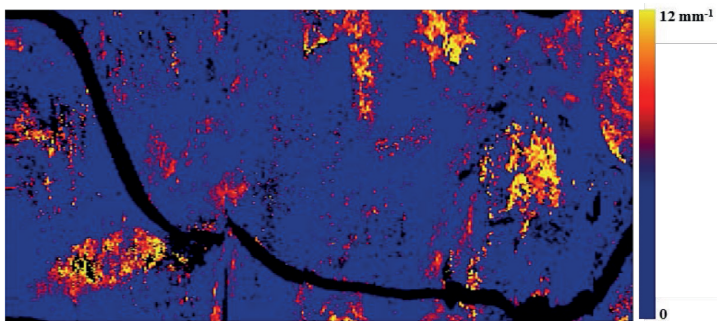


Figure 2.3 | Longitudinal attenuation map of a vessel sampled at a depth of 100-200 μm depicting the highly attenuating features in the entire pullback.

The attenuation map is made by taking the mean of 20 pixels from the depth of 100 μm from the lumen border (100-200 μm) along each A-line in all the frames across the pullback. The resulting longitudinal map has dimensions of frame number (x-axis), rotational angle (y-axis) and color codes the mean attenuation coefficient from 0-12 mm^{-1} . Such a map may highlight the lipid plaques and other high attenuating features in the entire pullback.

Even though the OCT pullbacks at different conditions are undertaken on the same vessel, it cannot be expected to exactly match due to factors such as non-uniform rotation, frame spacing and catheter orientation. To undertake quantitative comparison the attenuation map at different conditions should ideally be co-registered.

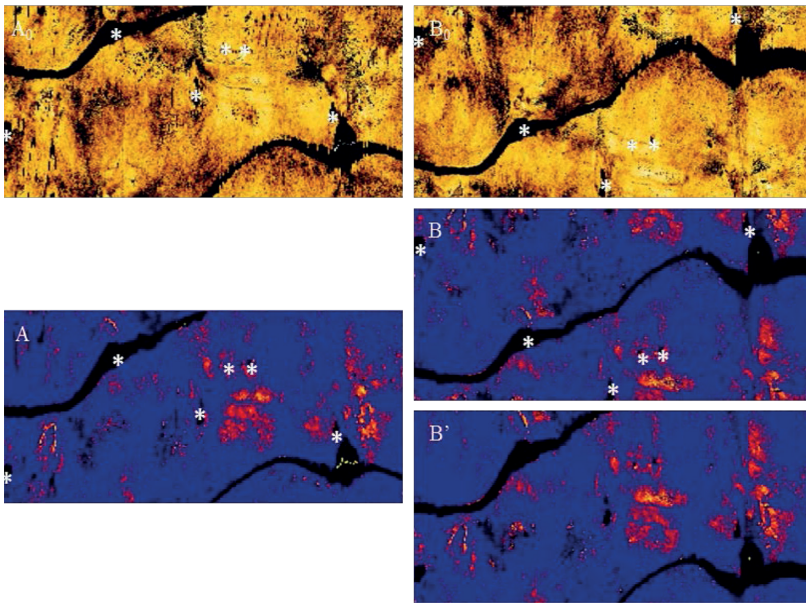


Figure 2.4 | Top: The en-face OCT map of pullbacks performed at UB (A_0) and FB (B_0) conditions; before registration. Bottom: The attenuation maps of the same pullbacks (A and B) where * indicates the control points used for registration, leading to (B'), the attenuation map after registration.

The registration procedure involves three steps. There is a first step of circularly shifting the images in the angular (y) direction. In the next step, an OCT intensity image map, folded out in the same manner as the attenuation data is used to select control points at side branches and other landmarks. A 2nd degree polynomial is fitted to the control points to derive a non-rigid transformation, which is then applied to the images. Finally, the data sets are cropped to represent the same physical length, as the pullback distal end can vary slightly and to avoid the guide catheter. Figure 2.4 shows an example of the unregistered OCT and attenuation maps with the control points and registered attenuation map images.

2.2.4 | Image analysis

In order to establish the presence and possible magnitude of the differences between OCT data at different temperatures and fixation conditions, we analyzed the images qualitatively [11], assessing image appearance, and quantitatively, quantifying the difference in attenuation coefficient.

A quantitative comparison between the attenuation maps will be dominated by mismatched data if it depends on pixel-perfect alignment, even with the elaborate registration applied here. To avoid this pitfall, the registered images are processed in overlapping kernels of 60×15 pixels, with a step size of 15 pixels in the angular direction and 5 pixels in the longitudinal direction. We analyze the median value of the attenuation coefficient within this kernel size. Any difference between tissue optical attenuation in both conditions can be studied by analyzing a scatter plot of the median attenuation, comparing a modified condition to the one that most accurately approximates in vivo circumstances (37°C , unfixed tissue). Differences in attenuation are quantified by finding the ratio of the median value of the kernels of other conditions against unfixed body temperature condition. We fit a line through the origin, the slope of which yields the root mean square difference. The size of the kernel is determined by maximizing R^2 of this linear fit. The statistical evaluation of the data is completed by a Bland-Altman analysis.

A similar analysis as the one discussed above was performed on the OCT image intensity itself, to assess any effect of fixation or temperature on the backscatter coefficient μ_b , which is implicit in I_0 in (1) [15]. We studied the mean intensity at a depth of 100-200 μm from the lumen boundary, as shown in Figure 2.4 (A_0 and B_0).

2.3 | Results

2.3.1 | Qualitative assessment

The potential similarities and differences of the parametric OCT images of tissues acquired under the different conditions are assessed qualitatively and quantitatively. Figure 2.5 illustrates a qualitative comparison of the cross-sectional OCT images before and after fixation matched with histology from that site in the vessel.

The histology shows a prominent streak of macrophages extending from the luminal surface into a fibro-lipidic plaque. The macrophage infiltration is evident in the OCT images pre- and post-fixation. In support of this observation, the corresponding attenuation images demonstrate a highly attenuating region consistent with macrophages [15,29].

Qualitatively, no systematic differences were found between the data acquired before and after fixation, neither in the OCT images themselves, nor in the attenuation coefficients. We did observe variations in image intensity or attenuation, but these could be attributed to position mismatches in the undersampled pullbacks.

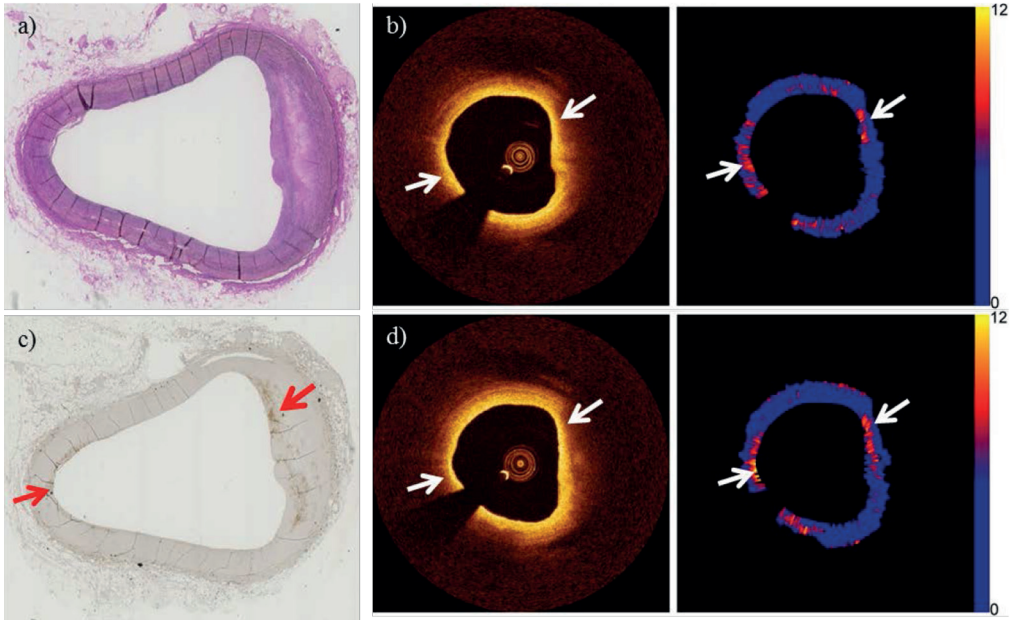


Figure 2.5 | (a) H&E and (c) CD68 stained histology image of a cross section. OCT and attenuation images of the cross section before (b) and after (d) fixation. The arrows indicate a streak of macrophages in the intima overlying a lipid pool. Additionally, luminal macrophage are evident on CD68 staining (arrowheads) with associated attenuation.

Likewise, we did not find any systematic difference between the OCT images of the same cross section acquired at different temperature conditions. Figure 2.6 shows the CD68 histology stain of a different cross section, compared to the OCT and attenuation images of the cross section in cold, room and body temperature conditions. The significant plaque feature in the cross section, the macrophages, are distinguishable at all temperature conditions. The attenuation values are comparable for all temperatures.

2.3.2 | Quantitative assessment

The repeatability of OCT is well established but subject to effects including variation in pullback starting point, heart motion and more importantly the luminal position of the catheter. Despite the use of our cadaveric heart rig and sequential imaging without removal of guidewire or imaging catheter, comparison of the OCT maps demonstrate variability preventing a pixel by pixel comparison. Consequently, comparison was limited to the median attenuation values in 60x15 pixel kernels in the longitudinal en-face map. The control condition for comparison is unfixed tissue at 37°C, considered to most closely match in-vivo conditions.

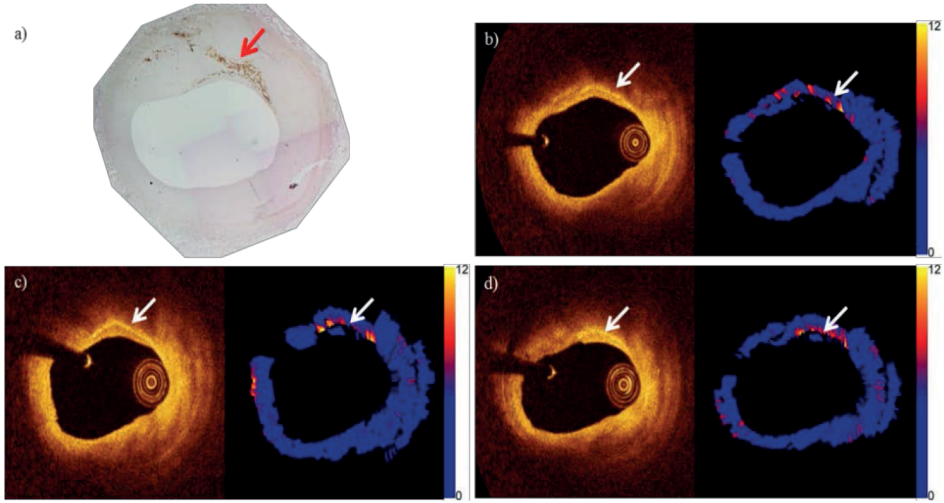


Figure 2.6 | a) CD68 stained histology image of a cross section. The arrow indicate the streak of macrophages. OCT and attenuation images (in units of mm^{-1}) of the cross section in b) UC, c) UR and d) UB conditions. The arrows indicate the streak of macrophages.

When comparing the medians from all other conditions to control, ideally they should have identical values. So the reasonable quantities to be checked are the ratio of the median attenuation coefficient in matching regions in different conditions, and the slope of the line through the origin of the scatter plot of medians (the coefficient of proportionality).

Figures 2.7(a) and 2.7(b) show the attenuation map of fresh body temperature of a vessel with the considered kernels of 60×15 pixels and the moving kernel step size. Figure 2.7(c) depicts the scatter plot of the median of the kernels between the two conditions with the fitted line through the origin and the R^2 value.

Figure 2.8 shows the box plot of the ratio of the median attenuation values of all conditions against UB condition and the resulting coefficient of proportionality in each case.

Bland-Altman analysis produced mean differences close to zero for all comparisons (ranging from 0 to 0.2 mm^{-1}) and 95% confidence intervals between 0.5 and 1.5 mm^{-1} , which is consistent with the accuracy of the attenuation algorithm. No statistically significant trends were found.

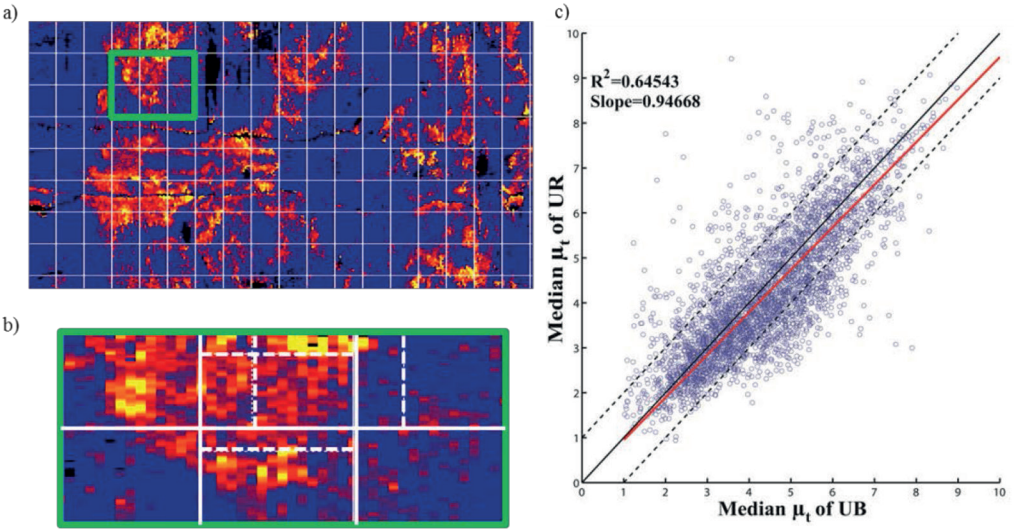


Figure 2.7 | a) Attenuation map of a vessel with the considered kernels b) the part of the map (in a) highlighted in green depicting the overlapping kernels c) scatter plot of the medians of the kernels in UB and UR conditions with the fitted straight line through origin (red) and the line with slope 1 (black) and the lines with $\pm 1 \text{ mm}^{-1}$ (dotted).

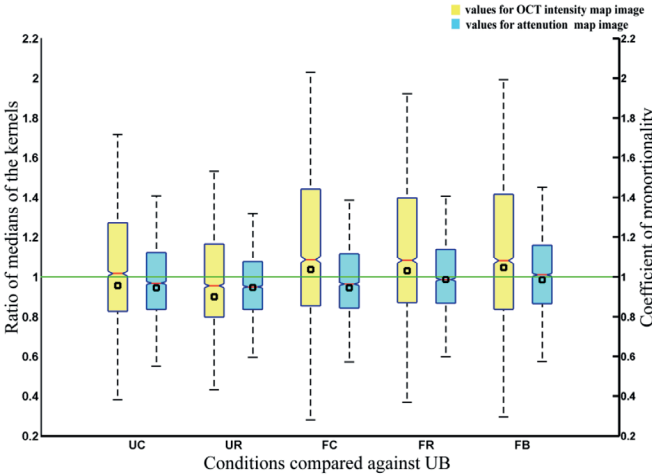


Figure 2.8 | (left y-axis) Box plot of the ratio of the median values of OCT intensity and attenuation in 60x15 kernels, plotted as median (red), 25th and 75th percentile (blue box), and 1.5 times the interquartile (whiskers). (right y-axis) Black squares: coefficient of proportionality extracted from the slope of the fit line for all the conditions.

In an analysis of the OCT image intensities, we found that the scatter in the data is much larger than for the attenuation coefficient, with typically $R^2 \approx 0.4$ for the linear fit and a median intensity ratio interquartile range of 0.6. One finding which appears to be robust, however, is that the image intensity is 11% higher in the OCT data of fixed tissue compared to unfixed, as measured by the ratio of the region medians as shown in Figure 2.8.

2.4 | Discussion

This study quantifies the effects of common tissue preparation steps on the optical properties of the artery wall. As new OCT analysis techniques are routinely developed on ex vivo tissues, it is important to know how temperature and tissue fixation affect the parameters that can be quantified from the OCT images. We extract the attenuation coefficient from the OCT images, a parameter that is relevant for tissue type. In our data, we see very small differences induced by temperature and fixation: relative to unfixed tissue at 37°C, the attenuation coefficient differs by a few percent at most in other conditions.

We studied the ratios of median attenuation values in different conditions, and the coefficient of proportionality. The ratios are scattered in a narrow range around unity, while the coefficient of proportionality, which is more sensitive to outliers, is around 0.95. A 5% deviation converts to 0.5 mm^{-1} error on 10 mm^{-1} attenuation. We typically find that the attenuation of a single tissue type varies within a range larger than 0.5 mm^{-1} , so the variation in the condition is not resolvable. This result supports the main conclusion of this work: tissue attenuation in coronary arteries ex vivo can be studied in fixed tissues, without special precautions for temperature, which may greatly facilitate data collection. The image intensity itself does appear to be affected by fixation. In the absence of attenuation changes, this suggests that the scattering phase function is modified by the microstructural changes in the tissue, leading to a larger backscattering coefficient. This observation is consistent with our experience that OCT images in fixed tissues appear brighter than matched unfixed images.

We base our attenuation comparison partially on linear fits through the scatter plots of the median attenuation in different conditions. However, the influence of temperature and fixation on the optical properties of different tissues need not be the same, which potentially causes a regression to the mean. In general, a linear relationship cannot be expected between the maps of different conditions, but we did not find any evidence for deviations from simple proportionality. This finding is further supported by the absence of trends in the Bland-Altman analysis. We chose to minimize the number of degrees of freedom by fitting a line through the origin.

We compare the median, and not the mean, because it is less sensitive to skewed distributions of the attenuation values in a region of interest. Other signal or image statistics could be studied as well: it is conceivable that changes to the tissue microstructure caused by handling or preservation affect the intensity variation or the scattering phase function. Such changes could show up in higher order intensity statistics, or the backscatter coefficient, respectively. The latter is proving to be a parameter

that is surprisingly resistant to quantitation. As we have demonstrated the relation between attenuation and tissue type [15], while other parameters are less studied, we chose to restrict the present study to attenuation only.

We have developed an analysis method that is robust against common registration errors. The OCT pullback has a large frame pitch relative to the width of the point spread function (the “frame thickness”) that can make it difficult to find the same cross section even in pullbacks of the same region of a vessel. Each frame of the OCT pullback is effectively made up of a spiral image of 200 μm through the vessel and therefore may not be accurately represented by a 3 μm thick histology section. This is essentially a sampling problem, that we deal with by constructing a longitudinal representation of the pullback to make quantitative comparisons. This has several advantages over analysis in cross section images. A longitudinal map brings out tissue features as a whole, along the vessel, while in a cross section only a part of it can be located. It also allows for non-rigid registration to correct for non-uniform rotation and variations in effective pullback speed (due to cardiac motion in vivo). The longitudinal representation remains a two-dimensional cross section through a three-dimensional data set, and sacrifices depth resolution. For detailed analyses, several longitudinal maps at different depths from the lumen boundary can be extracted. In order to eliminate sensitivity of the comparison to pixel-perfect alignment, we studied the median values of kernels of 60×15 pixels. This is necessary to extract meaningful differences, as any parametric difference between the various conditions would be obscured by large differences introduced by mismatches. The size of the kernel 60×15 pixels was chosen by maximizing the R^2 values of the fit.

The accuracy of the non-rigid registration step depends on the number of landmarks that are usable as control points. We attribute the remaining scatter in the data sets to persisting registration errors. These introduce a variance that is not explained by the analysis model and affect the R^2 of the fit for the medians. We find $R^2 \approx 0.6$, which still represents significant accuracy of the fit.

2.4.1 | Study limitations

Co-registration of multiple OCT images acquired at varying conditions, and comparison against histology is challenging. Despite careful reproduction of OCT imaging at all conditions and computational co-registration we concede that exact matching of images is not possible. However, we believe our methods of matching generate accurate comparisons. The inherent differences in longitudinal resolution between OCT (200 μm) & histology (3 μm) highlight OCT’s tendency to under-sample the vessel. We have overcome this by undertaking extensive histological preparation of vessel segments containing plaque of interest, allowing ‘best-fit’ matching with the lower resolution OCT images. Maintenance of steady-state temperature in the cadaveric heart model required prolonged infusion of PBS, incubated to the selected condition temperature. Despite measurement of vessel temperature with a needle-probe thermometer, it is possible that a temperature gradient existed from the vessel lumen into deeper tissue but not expected to be very significant considering the penetration depth of the OCT. The ultimate aim of this work is to facilitate translation into the clinical setting; however, we must concede that despite evaluation of variations in attenuation generated by temperature and fixation, other significant differences exist

between the ex-vivo & in-vivo environment. Particularly, the influence of cardiac motion on image acquisition and the potential influence of luminal blood on image quality.

2.5 | Conclusion

The results show that the ratio of the median attenuation values of kernels and the coefficient of proportionality or the slope of the line through the origin fitted for the medians is close to unity for every condition against the base condition. The largest deviation in slope from one is 0.06, leading to a change in tissue attenuation of less than 1 mm^{-1} , which is the approximate accuracy of the algorithm. The results suggest that fixation and room temperature conditions in the ex-vivo OCT experiments do not induce a systematic error.

2.6 | Acknowledgments

This work was funded by the Netherlands Heart Foundation grant (2010B064) and Heart Research UK (RG2608/12/14) and supported by researchers at the National Institute for Health Research Bristol Cardiovascular Biomedical Research Unit. We thank Pieter Kruizinga and Takeyoshi Kameyama for providing insight and expertise that greatly assisted the research and Jolanda Wentzel for helpful discussion. We also thank Mr. Paul Chappell of the workshop in BHI.

References and links

1. E. Falk, P. K. Shah, and V. Fuster, "Coronary Plaque Disruption," *Circulation* 92, 657-671 (1995).
2. Schaar, J. A., J. E. Muller, E. Falk, R. Virmani, V. Fuster, P. W. Serruys, A. Colombo, C. Stefanadis, S. Ward Casscells, P. R. Moreno, A. Maseri and A. F. van der Steen (2004). "Terminology for high-risk and vulnerable coronary artery plaques. Report of a meeting on the vulnerable plaque, June 17 and 18, 2003, Santorini, Greece." *Eur Heart J* 25(12):1077-1082.
3. R. Virmani, F. D. Kolodgie, A. P. Burke, A. Farb, and S. M. Schwartz, "Lessons from sudden coronary death - A comprehensive morphological classification scheme for atherosclerotic lesions," *Arterioscler Thromb Vasc Biol* 20, 1262-1275(2000).
4. S. Waxman, M. I. Freilich, M. J. Suter, M. Shishkov, S. Bilazarian, R. Virmani, B. E. Bouma, and G. J. Tearney, "A case of lipid core plaque progression and rupture at the edge of a coronary stent: Elucidating the mechanisms of drug-eluting stent failure," *Circ.-Cardiovasc. Interv.* 3,193-196(2010).
5. J. A. Goldstein, C. Grines, T. Fischell, R. Virmani, D. Rizik, J. Muller, and S. R. Dixon, "Coronary Embolization Following Balloon Dilation of Lipid-Core Plaques," *JACC Cardiovasc Imaging* 2,1420-1424(2009).
6. A. Tanaka, T. Imanishi, H. Kitabata, T. Kubo, S. Takarada, T. Tanimoto, A. Kuroi, H. Tsujioka, H. Ikejima, K. Komukai, H. Kataiwa, K. Okouchi, M. Kashiwaghi, K. Ishibashi, H. Matsumoto, K. Takemoto, N. Nakamura, K. Hirata, M. Mizukoshi, and T. Akasaka, "Lipid-rich plaque and myocardial perfusion after successful stenting in patients with non-ST-segment elevation acute coronary syndrome: an optical coherence tomography study," *Eur Heart J* (2009).
7. E. Regar, J. Ligthart, N. Bruining, and G. van Soest, "The diagnostic value of intracoronary optical coherence tomography," *Herz* 36,417-429(2011).
8. G. J. Tearney, E. Regar, T. Akasaka, T. Adriaenssens, P. Barlis, H. G. Bezerra, B. Bouma, N. Bruining, J.-m. Cho, S. Chowdhary, M. A. Costa, R. de Silva, J. Dijkstra, C. Di Mario, D. Dudeck, E. Falk, M. D. Feldman, P. Fitzgerald, H. Garcia, N. Gonzalo, J. F. Granada, G. Guagliumi, N. R. Holm, Y. Honda, F. Ikeno, M. Kawasaki, J. Kochman, L. Koltowski, T. Kubo, T. Kume, H. Kyono, C. C. S. Lam, G. Lamouche, D. P. Lee, M. B. Leon, A. Maehara, O. Manfrini, G. S. Mintz, K. Mizuno, M.-a. Morel, S. Nadkarni, H. Okura, H. Otake, A. Pietrasik, F. Prati, L. Räber, M. D. Radu, J. Rieber, M. Riga, A. Rollins, M. Rosenberg, V. Sirbu, P. W. J. C. Serruys, K. Shimada, T. Shinke, J. Shite, E. Siegel, S. Sonada, M. Suter, S. Takarada, A. Tanaka, M. Terashima, T. Troels, S. Uemura, G. J. Ughi, H. M. M. van Beusekom, A. F. W. van der Steen, G.-a. van Es, G. van Soest, R. Virmani, S. Waxman, N. J. Weissman, and G. Weisz, "Consensus Standards for Acquisition, Measurement, and Reporting of Intravascular Optical Coherence Tomography Studies: A Report From the International Working Group for Intravascular Optical Coherence Tomography Standardization and Validation," *J Am Coll Cardiol* 59,1058-1072(2012).
9. G. Guagliumi, M. A. Costa, V. Sirbu, G. Musumeci, H. G. Bezerra, N. Suzuki, A. Matiashvili, N. Lortkipanidze, L. Mihalcsik, A. Trivisonno, O. Valsecchi, G. S. Mintz, O. Dressler, H. Parise, A. Maehara, E. Cristea, A. J. Lansky, R. Mehran, and G. W. Stone, "Strut Coverage and Late Malapposition With Paclitaxel-Eluting Stents Compared With Bare Metal Stents in Acute Myocardial Infarction: Optical Coherence Tomography Substudy of the Harmonizing Outcomes With Revascularization and Stents in Acute Myocardial Infarction (HORIZONS-AMI) Trial," *Circulation* 123,274-281(2011).
10. G. Guagliumi, G. Musumeci, V. Sirbu, H. G. Bezerra, N. Suzuki, L. Fiocca, A. Matiashvili, N. Lortkipanidze, A. Trivisonno, O. Valsecchi, G. Biondi-Zoccai, and M. A. Costa, "Optical Coherence Tomography Assessment of In Vivo Vascular Response After Implantation of Overlapping Bare-Metal and Drug-Eluting Stents," *JACC Cardiovasc Interv* 3,531-539(2010).
11. H. Yabushita, B. E. Bourn, S. L. Houser, T. Aretz, I. K. Jang, K. H. Schlendorf, C. R. Kauffman, M. Shishkov, D. H. Kang, E. F. Halpern, and G. J. Tearney, "Characterization of human atherosclerosis by optical coherence tomography," *Circulation* 106,1640-1645(2002).
12. T. Kume, T. Akasaka, T. Kawamoto, N. Watanabe, E. Toyota, Y. Neishi, R. Sukmawan, Y. Sadahira, and K. Yoshida, "Assessment of coronary arterial plaque by optical coherence tomography," *Am J Cardiol* 97,1172-1175(2006).
13. D. Levitz, L. Thrane, M. H. Frosz, P. E. Andersen, C. B. Andersen, J. Valanciunaite, J. Swartling, S. Andersson-Engels, and P. R. Hansen, "Determination of optical scattering properties of highly-scattering media in optical coherence tomography images," *Opt Express* 12,249-259(2004).

14. F. J. van der Meer, D. J. Faber, D. M. Baraznji Sassoon, M. C. Aalders, G. Pasterkamp, and T. G. van Leeuwen, "Localized measurement of optical attenuation coefficients of atherosclerotic plaque constituents by quantitative optical coherence tomography," *IEEE Trans on Med Imaging* 24,1369-1376(2005).
15. G. van Soest, T. Goderie, E. Regar, S. Koljenovic, G. L. van Leenders, N. Gonzalo, S. van Noorden, T. Okamura, B. E. Bouma, G. J. Tearney, J. W. Oosterhuis, P. W. Serruys, and A. F. van der Steen, "Atherosclerotic tissue characterization in vivo by optical coherence tomography attenuation imaging," *J Biomed Opt* 15,011105(2010).
16. E. Regar, M. Gnanadesigan, A. F. W. Van der Steen, and G. van Soest, "Quantitative Optical Coherence Tomography Tissue-Type Imaging for Lipid-Core Plaque Detection," *JACC Cardiovasc Interv* 6,891-892(2013).
17. G. J. Ughi, T. Adriaenssens, P. Sinnaeve, W. Desmet, and J. D'hooge, "Automated tissue characterization of in vivo atherosclerotic plaques by intravascular optical coherence tomography images," *Biomed. Opt. Express* 4, 1014-1030(2013).
18. Bamber, J. C., M. J. Fry, C. R. Hill and F. Dunn (1977). Ultrasonic attenuation and backscattering by mammalian organs as a function of time after excision. *Ultrasound Med Biol* 3:15-20.
19. Bamber, J. C. and C. R. Hill (1979). "Ultrasonic attenuation and propagation speed in mammalian tissues as a function of temperature." *Ultrasound Med Biol* 5(2):149-157.
20. Bamber, J. C., C. R. Hill, J. A. King and F. Dunn (1979). "Ultrasonic propagation through fixed and unfixed tissues." *Ultrasound Med Biol* 5(2):159-165.
21. Schaar, J. A., C. L. de Korte, F. Mastik and A. F. van der Steen (2002). "Effect of temperature increase and freezing on intravascular elastography." *Ultrasonics* 40(1-8):879-881.
22. van der Steen, A. F., M. H. Cuypers, J. M. Thijssen and P. C. de Wilde (1991). "Influence of histochemical preparation on acoustic parameters of liver tissue: a 5-MHz study." *Ultrasound Med Biol* 17(9):879-891.
23. van der Steen, A. F., J. M. Thijssen, G. P. Ebben and P. C. de Wilde (1992). "Effects of tissue processing techniques in acoustical (1.2 GHz) and light microscopy." *Histochemistry* 97(2):195-199.
24. M. Nakano, M. Vorpahl, F. Otsuka, M. Taniwaki, S. K. Yazdani, A. V. Finn, E. R. Ladich, F. D. Kolodgie, and R. Virmani, "Ex vivo assessment of vascular response to coronary stents by optical frequency domain imaging," *JACC Cardiovasc Imaging* 5,71-82(2012) - Online Appendix.
25. Wang, T., W. Wieser, G. Springeling, R. Beurskens, C. T. Lancee, T. Pfeiffer, A. F. van der Steen, R. Huber and G. van Soest (2013). "Intravascular optical coherence tomography imaging at 3200 frames per second." *Opt Lett* 38(10):1715-1717.
26. T. W. Johnson, S. White, M. Gnanadesigan, H. Bourenane, J. W. Strange, A. C. Newby, G. van Soest, and A. Baumbach, "An ex-vivo "whole human heart model" for the development of intravascular imaging," *Heart* 98, 15-A16(2012).
27. T. G. van Leeuwen, D. J. Faber, and M. C. Aalders, "Measurement of the axial point spread function in scattering media using single-mode fiber-based optical coherence tomography," *Ieee J Sel Top Quant* 9,227-233(2003).
28. G. J. Ughi, T. Adriaenssens, K. Onsea, P. Kayaert, C. Dubois, P. Sinnaeve, M. Coosemans, W. Desmet, and J. D'hooge, "Automatic segmentation of in-vivo intra-coronary optical coherence tomography images to assess stent strut apposition and coverage," *Int J Cardiovasc Imaging* 28,229-241(2012).
29. O. A. Meissner, J. Rieber, G. Babaryka, M. Oswald, S. Reim, U. Siebert, T. Redel, M. Reiser, and U. Mueller-Lisse, "Intravascular optical coherence tomography: comparison with histopathology in atherosclerotic peripheral artery specimens," *J Vasc Interv Radiol* 17,343-349(2006).

Chapter 3

Optical coherence tomography attenuation imaging for lipid core detection: an ex-vivo validation study

Muthukaruppan Gnanadesigan, Ali S Hussain, Stephen White,
Simon Scoltock, Andreas Baumbach, Antonius FW van der Steen,
Evelyn Regar, Thomas W Johnson and Gijs van Soest

The International journal of Cardiovascular Imaging 2016
Accepted

Abstract

Objective: Lipid-core atherosclerotic plaques are associated with disease progression, procedural complications, and cardiac events. Coronary plaque lipid can be quantified in optical coherence tomography (OCT) pullbacks by measurement of lipid arcs and lipid lengths; parameters frequently used in clinical research, but labor intensive and subjective to analyze.

Methods: In this study, we investigated the ability of quantitative attenuation, derived from intravascular OCT, to detect plaque lipid. Lipid cores are associated with a high attenuation coefficient. We compared the index of plaque attenuation (IPA), a local quantitative measure of attenuation, to the manually measured lipid score (arc and length) on OCT images, and to the plaque characterization ex-vivo.

Results: We confirmed a correlation between the IPA and lipid scores ($R^2 > 0.7$). Comparison to histology shows that high attenuation is associated with fibroatheroma, but also with macrophage presence.

Conclusions: IPA is a robust, reproducible, and user-independent measure that facilitates quantification of coronary lipid, a potential tool in clinical research and in guiding percutaneous coronary intervention.

Keywords: Optical coherence tomography, attenuation, lipid core plaque

3.1 | Introduction

Sudden rupture of a lipid-rich atherosclerotic plaque, causing acute myocardial infarction is one of the major causes of death worldwide. Early detection of such coronary plaques may influence treatment strategies and facilitate a reduction in clinical events secondary to ischemic heart disease [1]. The lipid core plaque (LCP) or fibroatheroma is a type of atherosclerotic lesion prone to develop unstable features under the influence of inflammatory processes and mechanical forces. Hence, imaging of tissue composition, especially in LCP, plays an important role in recognizing plaque instability [2]. LCP detection also has implications in the guidance of coronary interventions, as these plaques have been implicated in peri-procedural and follow-up events [3-8]. Intravascular optical coherence tomography (OCT) is now widely used as a clinical tool, imaging vessel lumen and wall morphology for guidance of stent placement and optimization [9-12]. OCT is a catheter-based imaging technique that provides high-resolution images of the arterial wall. Interpretation of the images allows for a qualitative assessment of the tissue composition [7,11,12].

Measurement of lipid length and lipid arc in OCT for calculation of a lipid score is a common method to quantify lipid in cardiovascular research [13,14]. This score is an indicator of the extent and severity of atherosclerotic disease in the coronary arteries. It provides patient and lesion-specific diagnostic information, and may serve as a metric of plaque progression in temporal studies. Currently a skilled OCT reader is required to score lipid accumulations, and it is a time-consuming manual procedure with considerable inter-observer variability [13]. An automated tissue score that can provide the same information can be a very useful tool in research with potential for clinical utility.

Various tissue components have different optical parameters and this contrast can be exploited to devise a tissue characterization method based on IV-OCT data [15]. Quantification of tissue optical parameters may assist image interpretation by OCT users. The attenuation coefficient is a robust tissue optical parameter [16] that has been proposed for tissue characterization [17-19]. Lipid-rich necrotic core and macrophage infiltration have high attenuation compared to fibrous tissue and other plaque components. Such methods have recently been augmented with statistical image metrics to achieve tissue detection [20].

In this study, we validate optical attenuation imaging of coronary plaque tissue type in an ex-vivo setting, using whole heart specimens harvested from cadavers and imaged in a purpose-built setup. We focus on the ability of attenuation imaging to identify coronary plaque lipid. The objective of the study was to compare the quantitative attenuation scores with the manually measured lipid scores of plaque segments, which were characterized based on the histology.

3.2 | Materials and methods

3.2.1 | Specimens

Whole cadaveric hearts used were obtained from the Bristol Heart Valve Bank and excised within 48 hours post-mortem and stored at 4°C [21]. A short guide catheter was introduced into the right coronary artery to facilitate intravascular imaging and fixed in position with sutures. All tissues were handled in accordance with the local ethics regulations. The heart specimen was held within a custom-built Perspex container, with adapters on both sides of the lid allowing connection of the guide internally, and a Y-connector and pressure/injector manifold externally [21]. For the study a total of 6 heart specimens were imaged.

3.2.2 | IV-OCT imaging

For intravascular OCT imaging, the imaged artery was perfused with phosphate buffered saline (PBS) and the intracoronary pressure was maintained at 100 mmHg. The OCT image pullbacks of the coronary arteries were performed at 20 mm/s. The OCT system used for imaging was a C7-XR with Dragonfly catheter (St. Jude Medical Inc. St. Paul, MN, U.S.A). The end of the guide catheter served as a reference point.

3.2.3 | Histology and plaque characterization

The imaged vessels were pressure-fixed while still on the heart with buffered formalin at 100 mmHg for 15 minutes, excised from the heart, and fixed with buffered formalin for 24 hours. Then the vessels were embedded in paraffin and cut into 4-mm blocks with the end of the guide catheter serving as a reference. The proximal face of each block was cut at 3 µm thickness for histological analysis and serial sections stained with Haematoxylin and Eosin (H&E), Elastic Van Gieson (EVG), Cluster of Differentiation 68 (CD68) and smooth muscle cell α-Actin stains. CD68 and α-Actin were visualized using mouse anti-CD68 (DAKO M0814 and M0876 mixed 1/200 of each), and mouse anti-α actin (DAKO, M0851 1/200), or matched mouse IgG control, followed by biotinylated goat anti-mouse and extravidin-HRP conjugate with DAB staining.

Twenty-three atherosclerotic plaques were identified from the six cadaveric heart specimens. A skilled pathologist analyzed the plaque characteristics by the histological staining and classified the plaque type. The lesions were classified into pathological intimal thickening, pathological intimal thickening with macrophage infiltration and fibroatheroma using standard criteria [2,22]. Fibroatheroma with less than 65 µm cap thickness was classified as thin-cap fibroatheroma.

3.2.4 | Parametric imaging

The acquired OCT images were analyzed to quantify the attenuation coefficient of the tissues by fitting the OCT signal to a single scattering model [18,19].

$$\langle I_d \rangle = T(r)S(r)I_0 e^{-\mu_r r}, \quad (1)$$

where $S(r)$ is the OCT signal roll off and $T(r)$ is the point spread function (PSF) of the catheter [23]. The attenuation coefficient μ_a is the parameter of interest. The attenuation calculation and the model implementation were done in Matlab release 2012b (The Mathworks, Inc., Natick, MA, USA). The model is fitted in the polar image, in every A-line starting from the edge of the lumen [18,20], in small windows of varying length [24] to extract the attenuation coefficients. The accuracy of the extracted attenuation coefficient is approximately 1 mm^{-1} [18]. The data analysis results in an attenuation image per frame of the pullback. Figure 3.1 depicts a frame of OCT, its corresponding attenuation image and histology.

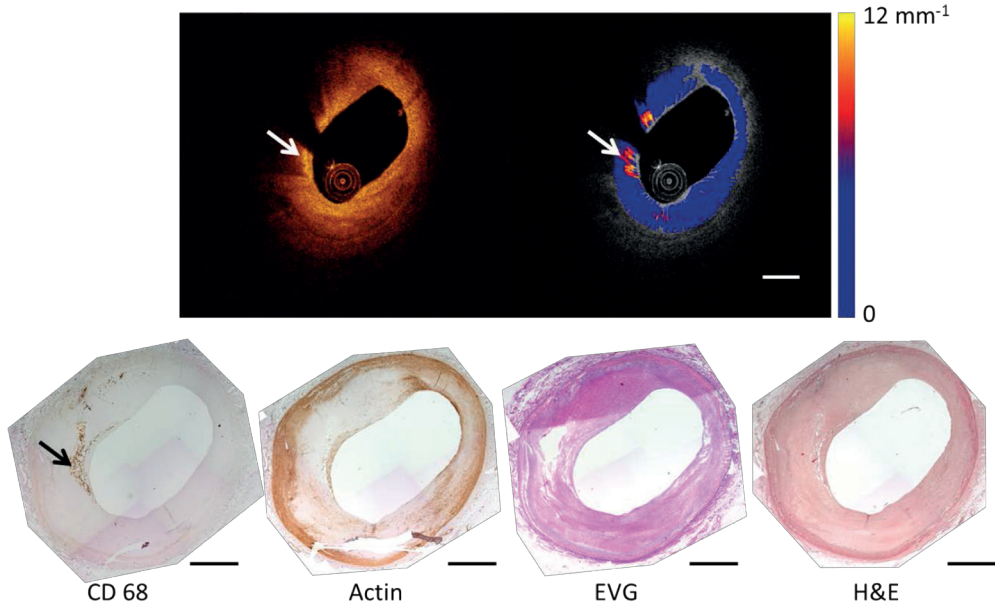


Figure 3.1 | A representative OCT frame and the corresponding attenuation image depicting high attenuation features and the corresponding Histology stains. The arrow heads point to a streak of macrophages that shows high attenuation and are clearly stained in CD68. The dashed scale bar equals 1 mm.

We made longitudinal attenuation maps of the vessel depicting the tissue properties of the intima along the entire pullback. The map was constructed by sampling the maximum value of attenuation between the lumen border and the internal elastic lamina (IEL) as shown in Figure 3.2. The en-face map display has dimensions of frame number (horizontal-axis), rotational angle (vertical-axis) and color-codes the maximum attenuation coefficient per A-line in the range $0-12 \text{ mm}^{-1}$. Such a map highlights strongly attenuating features like the lipid plaques in the entire pullback [16] and corresponds well with a visual assessment of LCP in the OCT data by an expert reader [25].

We also defined an Index of Plaque Attenuation (IPA) to quantify the parametric image. IPA is the ratio of the number of pixels in the attenuation map or a segment of it with an attenuation coefficient greater than a certain threshold x to the total number of pixels, multiplied by a factor of 1000. Mathematically it is represented as

$$IPA_x = \frac{N(\mu \geq x)}{N_{\text{total}}} \times 1000 \quad (2)$$

where N is the number of pixels. x is the threshold in attenuation coefficient, with a maximum value of 12 mm^{-1} , that enables IPA to represent a particular tissue type.

The IPA was calculated in 4mm windows, covering a plaque segment. For the frame pitch of $200 \mu\text{m}$ that we used in our study, a window for IPA computation comprises 20 OCT frames. The OCT data were matched to the histology cross-sections based on longitudinal position and general anatomy (side branches and presence of plaque).

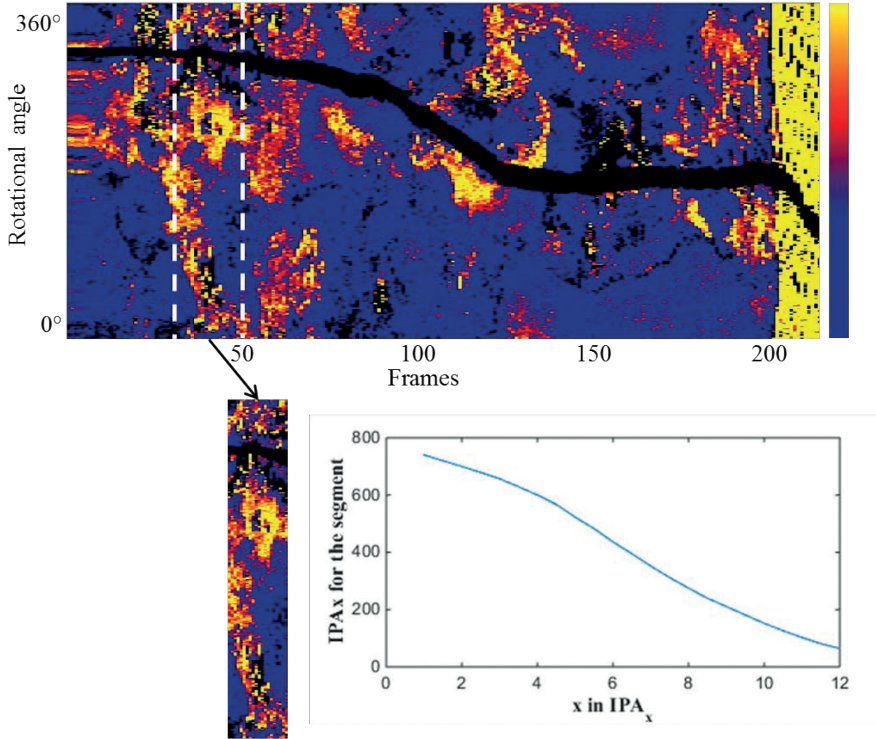


Figure 3.2 | A representative image of the en-face map depicting the attenuation features across the vessel and the 4 mm segment of a plaque that would be used to calculate the IPA. The inset plot shows the IPA for the segment for different thresholds ' x ' in IPA_x . Color scale runs from 0-12 mm^{-1} .

3.2.5 | Lipid measurements

Lipid measurements were made on the OCT frames, using the Ilumien offline OCT review workstation by St. Jude Medical (St. Paul, MN, USA). The lipid length was measured by detection of sequential OCT frames within a plaque segment containing lipid, defined as a diffusely bordered signal-poor region with high attenuation by the signal rich region covering them [7,26]. The pitch of the OCT enabled calculation of the lipid length in mm. The lipid arc measurements were made by defining the circumferential extent of the lipid core from the vessel centre and a mean for the plaque segment was calculated. Combining both measurements a lipid score was calculated, which is the product of the average lipid arc of the segment and the lipid length of the segment. To establish the relation between OCT lipid score and optical attenuation coefficient, we computed the correlation (Pearson's r) between lipid score and IPA_x for different values of x (1,1.5,...12) in all segments.

3.2.6 | Statistical analysis

Continuous variables are expressed as mean (standard deviation), or median (interquartile range; IQR) and categorical variables are expressed as percentages. The regression analysis was performed on the lipid measurements and IPA , with linear least squares fit and the coefficient of determination r^2 (square of the correlation coefficient r) was used.

3.3 | Results

According to the analysis of the histological sections, there were 16 fibroatheromas, 3 fibrous plaques, 2 pathological intimal thickenings and 2 pathological intimal thickenings with macrophage infiltration. One fibroatheroma with less than 65 microns cap thickness was classified as thin cap fibroatheroma.

We measured the lipid scores in the OCT recordings of the segments of interest. The median of the mean lipid arc of the plaques was 81.98 ± 45 degrees and the median of the lipid length was 3.9 ± 2.1 mm. The scores ranged from 0 to 638.4 mm° . There were eight plaques that did not have the characteristics of LCP according to the consensus OCT criteria [7].

The maximum correlation coefficient between the lipid score and IPA_x was found for a threshold of $x=8.5 \text{ mm}^{-1}$ ($IPA_{8.5}$), and equaled $r=0.85$ ($p<0.0001$). The relationship between IPA and the lipid scores for all the 23 plaques are given in Figure 3.3. The data points in the graph are color-coded based on the plaque type classification as shown in the legend.

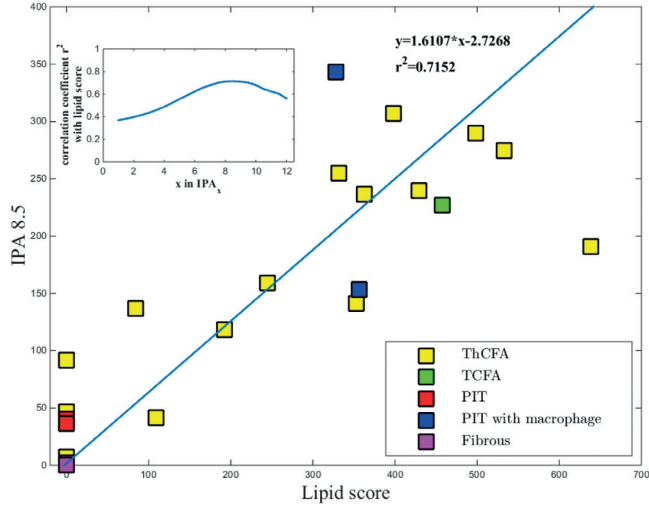


Figure 3.3 | Correlation between IPA8.5 and Lipid score by OCT (mean lipid arc*lipid length). The inset plot shows the correlation coefficient with the lipid score for different thresholds 'x' in IPA_x . The legend shows the color code for plaque types.

3.4 | Discussion

This study investigated the ability of the index of plaque attenuation (IPA), a bias free and reproducible summary measurement of attenuating tissue types, to detect lipids. The study aimed to validate OCT attenuation coefficient as a lipid-core detection tool. The main finding of the study was that the OCT-derived index, the $IPA_{8.5}$, have a significant correlation ($R^2 > 0.7$) with the manual lipid score in OCT images, which enables automation of the coronary plaque lipid assessment by OCT. Lipid scoring is a time consuming process, where frame-by-frame analysis and measurement is required. Previous studies which compared the lipid score by OCT to automated indices like the near-infrared spectroscopy (NIRS)-based Lipid Core Burden Index (LCBI) found a lesser correlation ($R^2 = 0.436$) [27]. This weaker association between OCT measurements and LCBI may be explained by registration errors in measurements made by different catheters, but also by the physically different detection mechanisms (scattering-dominated attenuation for OCT, vs. optical absorption in NIRS). The IPA, which is the result of automatic computation of plaque attenuation, has the potential as a clinical tool as it can indicate the presence and location of lipid rich plaques in an entire pullback, and provides an alternative to manual scoring in cardiovascular research. IPA could be displayed as a color-coded block along the vessel indicating probable lipid core plaques as shown in Figure 3.4. IPA, being an index calculated from a physical parameter, is robust and reproducible.

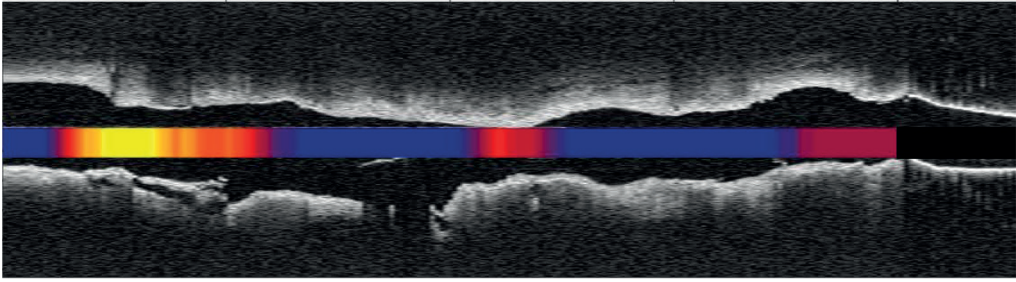


Figure 3.4 | Color coded $IPA_{8.5}$ as bar embedded in a OCT L-mode image of an artery.

The Figure 3.3 demonstrated that thick cap fibroatheroma exhibited a range of low to high IPA values, showing that lipid content is just one tissue component contributing to optical attenuation. We only found one thin cap fibroatheroma in our data, which had large OCT-lipid burden as expected [28]. It had a high IPA value, illustrating the relation between manual OCT measurements and automatic IPA analysis. Its typical dense macrophage infiltration by histology contributed to the observed attenuation. Among the four plaques classified as pathological intimal thickening (PIT), two had macrophage infiltration. The two PITs with macrophage exhibited high IPA values even though pathological evidence of lipid was not available. The gap between the PITs with and without macrophages was very significant, as expected. The three fibrotic plaques had near zero IPA values, as expected. The three fibrous plaques and the four PITs were among the eight plaques scored as having no lipid on OCT, along with one fibroatheroma with deep extra-cellular cholesterol.

3.4.1 | Limitations

Our data set is targeted towards validation of lipid measurements, and so does not reflect the heterogeneity of atherosclerosis in a clinical setting, with few plaques other than FA, and only one TCFA. The two included macrophage-infiltrated PIT plaques exhibit high attenuation even in the absence of histological evidence for lipids, a known mechanism resulting in false positives for lipid detection by OCT [7,29,30]. It was not possible to compare IPA with the lipid scores from histology as it is not practical to measure lipid length and the mean lipid arc in the whole segment. The attenuation calculation itself is automated and fast but in calculation of IPA, manual media segmentation is currently necessary to avoid artifacts due to the intima-media border. To be able to automate the whole process and for application to large datasets, automated media segmentation is required. This software is currently under development in our institute [31].

3.5 | Conclusion

We validated the optical attenuation as a tissue classification tool. We investigated a quantitative measure of the attenuating tissue types, the IPA. Our results show that the OCT-derived index of plaque attenuation has a correlation ($R^2 > 0.7$) with the conventional lipid score on OCT images. The results highlight the potential of a robust and fast identification tool of lipids in OCT pullbacks.

3.6 | Acknowledgements

The authors acknowledge the contribution of Dr. Giovanni Ughi for providing the algorithm for Lumen detection.

3.7 | Compliance with Ethical Standards

Funding: This work was funded by the Netherlands Heart Foundation grant (2010B064) and Heart Research UK (RG2608/12/14) and supported by researchers at the National Institute for Health Research Bristol Cardiovascular Biomedical Research Unit.

Conflict of Interest: Erasmus MC has patent licensing agreements with Terumo Corporation and Boston Scientific. Dr. Van Soest (Terumo) and Dr. Van der Steen (Terumo, Boston Scientific) have the right to receive royalties as part of these licensing agreements.

Ethical approval: This article does not contain any studies with human participants or animals performed by any of the authors.

References

1. E. Falk, P. K. Shah, and V. Fuster, "Coronary plaque disruption," *Circulation* 92,657-671(1995).
2. R. Virmani, F. D. Kolodgie, A. P. Burke, A. Farb, and S. M. Schwartz, "Lessons from sudden coronary death: a comprehensive morphological classification scheme for atherosclerotic lesions," *Arterioscler Thromb Vasc Biol* 20,1262-1275(2000).
3. S. Waxman, M. I. Freilich, M. J. Suter, M. Shishkov, S. Bilazarian, R. Virmani, B. E. Bouma, and G. J. Tearney, "A case of lipid core plaque progression and rupture at the edge of a coronary stent: elucidating the mechanisms of drug-eluting stent failure," *Circ Cardiovasc Interv* 3,193-196(2010).
4. J. A. Goldstein, C. Grines, T. Fischell, R. Virmani, D. Rizik, J. Muller, and S. R. Dixon, "Coronary embolization following balloon dilation of lipid-core plaques," *JACC Cardiovasc Imaging* 2,1420-1424(2009).
5. A. Tanaka, T. Imanishi, H. Kitabata, T. Kubo, S. Takarada, T. Tanimoto, A. Kuroi, H. Tsuchioka, H. Ikejima, K. Komukai, H. Kataiwa, K. Okouchi, M. Kashiwaghi, K. Ishibashi, H. Matsumoto, K. Takemoto, N. Nakamura, K. Hirata, M. Mizukoshi, and T. Akasaka, "Lipid-rich plaque and myocardial perfusion after successful stenting in patients with non-ST-segment elevation acute coronary syndrome: an optical coherence tomography study," *Eur Heart J* 30,1348-1355(2009).
6. E. Regar, J. Ligthart, N. Bruining, and G. van Soest, "The diagnostic value of intracoronary optical coherence tomography," *Herz* 36,417-428(2011).
7. G. J. Tearney, E. Regar, T. Akasaka, T. Adriaenssens, P. Barlis, H. G. Bezerra, B. Bouma, N. Bruining, J. M. Cho, S. Chowdhary, M. A. Costa, R. de Silva, J. Dijkstra, C. Di Mario, D. Dudek, E. Falk, M. D. Feldman, P. Fitzgerald, H. M. Garcia-Garcia, N. Gonzalo, J. F. Granada, G. Guagliumi, N. R. Holm, Y. Honda, F. Ikeno, M. Kawasaki, J. Kochman, L. Koltowski, T. Kubo, T. Kume, H. Kyono, C. C. Lam, G. Lamouche, D. P. Lee, M. B. Leon, A. Maehara, O. Manfrini, G. S. Mintz, K. Mizuno, M. A. Morel, S. Nadkarni, H. Okura, H. Otake, A. Pietrasik, F. Prati, L. Raber, M. D. Radu, J. Rieber, M. Riga, A. Rollins, M. Rosenberg, V. Sirbu, P. W. Serruys, K. Shimada, T. Shinke, J. Shite, E. Siegel, S. Sonoda, M. Suter, S. Takarada, A. Tanaka, M. Terashima, T. Thim, S. Uemura, G. J. Ughi, H. M. van Beusekom, A. F. van der Steen, G. A. van Es, G. van Soest, R. Virmani, S. Waxman, N. J. Weissman, and G. Weisz, "Consensus standards for acquisition, measurement, and reporting of intravascular optical coherence tomography studies: a report from the International Working Group for Intravascular Optical Coherence Tomography Standardization and Validation," *J Am Coll Cardiol* 59,1058-1072(2012).
8. F. Prati, L. Di Vito, G. Biondi-Zoccai, M. Occhipinti, A. La Manna, C. Tamburino, F. Burzotta, C. Trani, I. Porto, V. Ramazzotti, F. Imola, A. Manzoli, L. Matera, A. Cremonesi, and M. Albertucci, "Angiography alone versus angiography plus optical coherence tomography to guide decision-making during percutaneous coronary intervention: the Centro per la Lotta contro l'Infarto-Optimisation of Percutaneous Coronary Intervention (CLI-OPCI) study," *EuroIntervention* 8,823-829(2012).
9. G. Guagliumi, G. Musumeci, V. Sirbu, H. G. Bezerra, N. Suzuki, L. Fiocca, A. Matiashevili, N. Lortkipanidze, A. Trivisonno, O. Valsecchi, G. Biondi-Zoccai, and M. A. Costa, "Optical coherence tomography assessment of in vivo vascular response after implantation of overlapping bare-metal and drug-eluting stents," *JACC Cardiovasc Interv* 3,531-539(2010).
10. G. Guagliumi, M. A. Costa, V. Sirbu, G. Musumeci, H. G. Bezerra, N. Suzuki, A. Matiashevili, N. Lortkipanidze, L. Mihalcsik, A. Trivisonno, O. Valsecchi, G. S. Mintz, O. Dressler, H. Parise, A. Maehara, E. Cristea, A. J. Lansky, R. Mehran, and G. W. Stone, "Strut coverage and late malapposition with paclitaxel-eluting stents compared with bare metal stents in acute myocardial infarction: optical coherence tomography substudy of the Harmonizing Outcomes with Revascularization and Stents in Acute Myocardial Infarction (HORIZONS-AMI) Trial," *Circulation* 123,274-281(2011).
11. H. Yabushita, B. E. Bouma, S. L. Houser, H. T. Aretz, I. K. Jang, K. H. Schlendorf, C. R. Kauffman, M. Shishkov, D. H. Kang, E. F. Halpern, and G. J. Tearney, "Characterization of human atherosclerosis by optical coherence tomography," *Circulation* 106,1640-1645(2002).
12. T. Kume, T. Akasaka, T. Kawamoto, N. Watanabe, E. Toyota, Y. Neishi, R. Sukmawan, Y. Sadahira, and K. Yoshida, "Assessment of coronary arterial plaque by optical coherence tomography," *Am J Cardiol* 97,1172-1175(2006).
13. S. J. Kim, H. Lee, K. Kato, T. Yonetsu, L. Xing, S. Zhang, and I. K. Jang, "Reproducibility of in vivo measurements for fibrous cap thickness and lipid arc by OCT," *JACC Cardiovasc Imaging* 5,1072-1074(2012).

14. A. J. Brown, D. R. Obaid, C. Costopoulos, R. A. Parker, P. A. Calvert, Z. Teng, S. P. Hoole, N. E. West, M. Goddard, and M. R. Bennett, "Direct Comparison of Virtual-Histology Intravascular Ultrasound and Optical Coherence Tomography Imaging for Identification of Thin-Cap Fibroatheroma," *Circ Cardiovasc Imaging* 8,e003487(2015).
15. C. Xu, J. M. Schmitt, S. G. Carlier, and R. Virmani, "Characterization of atherosclerosis plaques by measuring both backscattering and attenuation coefficients in optical coherence tomography," *J Biomed Opt* 13,034003(2008).
16. M. Gnanadesigan, G. van Soest, S. White, S. Scoltock, G. J. Ughi, A. Baumbach, A. F. van der Steen, E. Regar, and T. W. Johnson, "Effect of temperature and fixation on the optical properties of atherosclerotic tissue: a validation study of an ex-vivo whole heart cadaveric model," *Biomed Opt Express* 5,1038-1049(2014).
17. E. Regar, M. Gnanadesigan, A. F. Van der Steen, and G. van Soest, "Quantitative optical coherence tomography tissue-type imaging for lipid-core plaque detection," *JACC Cardiovasc Interv* 6,891-892(2013).
18. G. van Soest, T. Goderie, E. Regar, S. Koljenovic, G. L. van Leenders, N. Gonzalo, S. van Noorden, T. Okamura, B. E. Bouma, G. J. Tearney, J. W. Oosterhuis, P. W. Serruys, and A. F. van der Steen, "Atherosclerotic tissue characterization in vivo by optical coherence tomography attenuation imaging," *J Biomed Opt* 15,011105(2010).
19. F. J. van der Meer, D. J. Faber, D. M. Baraznji Sassoon, M. C. Aalders, G. Pasterkamp, and T. G. van Leeuwen, "Localized measurement of optical attenuation coefficients of atherosclerotic plaque constituents by quantitative optical coherence tomography," *IEEE Trans Med Imaging* 24,1369-1376(2005).
20. G. J. Ughi, T. Adriaenssens, P. Sinnavee, W. Desmet, and J. D'Hooge, "Automated tissue characterization of in vivo atherosclerotic plaques by intravascular optical coherence tomography images," *Biomed Opt Express* 4,1014-1030(2013).
21. T. W. Johnson, S. White, M. Gnanadesigan, H. Bourenane, J. W. Strange, A. C. Newby, G. van Soest, and A. Baumbach, "An Ex-Vivo "Whole Human Heart Model" for the Development of Intravascular Imaging," *Heart* 98,15-A16(2012).
22. J. A. Schaar, J. E. Muller, E. Falk, R. Virmani, V. Fuster, P. W. Serruys, A. Colombo, C. Stefanadis, S. Ward Casscells, P. R. Moreno, A. Maseri, and A. F. van der Steen, "Terminology for high-risk and vulnerable coronary artery plaques. Report of a meeting on the vulnerable plaque, June 17 and 18, 2003, Santorini, Greece," *Eur Heart J* 25, 1077-1082(2004).
23. T. G. van Leeuwen, D. J. Faber, and M. C. Aalders, "Measurement of the axial point spread function in scattering media using single-mode fiber-based optical coherence tomography," *Ieee J Sel Top Quant* 9,227-233(2003).
24. G. van Soest, T. P. M. Goderie, S. van Noorden, and A. F. W. van der Steen, "Algorithm Optimization for Quantitative Analysis of Intravascular Optical Coherence Tomography Data," *P Soc Photo-Opt Ins* 7161(2009).
25. A. Karanasos, C. Simsek, M. Gnanadesigan, N. S. van Ditzhuijzen, R. Freire, J. Dijkstra, S. Tu, N. Van Mieghem, G. van Soest, P. de Jaegere, P. W. Serruys, F. Zijlstra, R. J. van Geuns, and E. Regar, "OCT assessment of the long-term vascular healing response 5 years after everolimus-eluting bioresorbable vascular scaffold," *J Am Coll Cardiol* 64, 2343-2356(2014).
26. F. Prati, E. Regar, G. S. Mintz, E. Arbustini, C. Di Mario, I. K. Jang, T. Akasaka, M. Costa, G. Guagliumi, E. Grube, Y. Ozaki, F. Pinto, and P. W. Serruys, "Expert review document on methodology, terminology, and clinical applications of optical coherence tomography: physical principles, methodology of image acquisition, and clinical application for assessment of coronary arteries and atherosclerosis," *Eur Heart J* 31,401-415(2010).
27. T. Yonetsu, W. Suh, F. Abtahian, K. Kato, R. Vergallo, S. J. Kim, H. Jia, I. McNulty, H. Lee, and I. K. Jang, "Comparison of near-infrared spectroscopy and optical coherence tomography for detection of lipid," *Catheter Cardiovasc Interv* 84,710-717(2014).
28. A. J. Brown, D. R. Obaid, C. Costopoulos, R. A. Parker, P. A. Calvert, Z. Teng, S. P. Hoole, N. E. J. West, M. Goddard, and M. R. Bennett, "Direct Comparison of Virtual-Histology Intravascular Ultrasound and Optical Coherence Tomography Imaging for Identification of Thin-Cap Fibroatheroma," *Circulation: Cardiovascular Imaging* 8,e003487(2015).
29. M. Kashiwagi, H. Kitabata, Y. Ozaki, T. Imanishi, and T. Akasaka, "Fatty streak assessed by optical coherence tomography: early atherosclerosis detection," *Eur Heart J Cardiovasc Imaging* 14,109(2013).
30. G. van Soest, E. Regar, T. P. Goderie, N. Gonzalo, S. Koljenovic, G. J. van Leenders, P. W. Serruys, and A. F. van der Steen, "Pitfalls in plaque characterization by OCT: image artifacts in native coronary arteries," *JACC Cardiovasc Imaging* 4,810-813(2011).
31. G. Zahnd, A. Karanasos, G. van Soest, E. Regar, W. Niessen, F. Gijzen, and T. van Walsum, "Quantification of fibrous cap thickness in intracoronary optical coherence tomography with a contour segmentation method based on dynamic programming," *Int J Comput Assist Radiol Surg* 10,1383-1394(2015).

Chapter 4

Automated characterization of lipid-core plaques in vivo by quantitative optical coherence tomography tissue type imaging

Muthukaruppan Gnanadesigan, T. Kameyama, Antonios Karanasos,
Nienke S van Ditzhuijzen, Johannes N van der Sijde, Robert-Jan van Geuns,
Jurgen Ligthart, Karen Witberg, Giovanni J. Ughi, Antonius FW van der Steen,
Evelyn Regar and Gijs van Soest

EuroIntervention 2016, accepted

Abstract

To investigate the ability of atherosclerotic tissue characterization in vivo, we are conducting the OC3T study: a prospective single-center validation study of 61 patients, comparing OCT-derived optical attenuation to NIRS/IVUS. We compare the chemogram and the en-face OCT attenuation map. The plaque area with the highest 4mm Lipid Core Burden Index (LCBI) was compared with the OCT Index of Plaque Attenuation (IPA) for the same. Unlike LCBI, IPA is significantly larger in thin-cap than in thick-cap plaques.

Keywords: Optical coherence tomography, attenuation, lipid core plaque

4.1 | Introduction

Diagnosis and effective intervention on ischemic heart disease benefits from early detection of coronary plaques that are likely to precipitate clinical events [1]. Plaque morphological features that have been associated with instability include a lipid-rich necrotic core, contained by a fragile layer of fibrous tissue that can be compromised by inflammation and mechanical forces [2]. Forces exerted by the variable blood pressure, or by intravascular devices used in percutaneous coronary interventions (PCI) may cause rupture of the fibrous cap, releasing the thrombogenic material, and leading to acute coronary syndrome or periprocedural myocardial infarction (MI). Hence tissue composition is important in recognizing plaque instability [3]. Detection of lipid-core plaques (LCP) has important implications for guidance of coronary interventions, as LCP has been recognized as a potential factor in periprocedural and future adverse events [4-9]. Intravascular optical coherence tomography (OCT) is gaining popularity as a clinical tool for assessment of stent placement and optimization [10-14]. OCT provides high resolution arterial images, from which vessel wall composition can be assessed by qualitative interpretation [11,15,16]. The quantification of tissue optical properties derived from the OCT images has been proposed as method to automate tissue characterization, or at least support image interpretation. The attenuation coefficient is a robust tissue optical parameter that can be used in tissue characterization [17,18]. Both necrotic core and macrophage infiltration, plaque features that have been associated with impaired stability, have high attenuation compared to fibrous and calcified tissues [19]. Such analyses have recently been augmented with statistical image metrics to achieve tissue identification [20].

A catheter based intracoronary near-infrared reflection spectroscopy (NIRS) and intravascular ultrasound (IVUS) system (InfraRedx, Burlington, MA, USA) has been used for lipid detection in vivo [21,22], operating by spectrally analysing the reflected light by the tissue. Spectral features are translated into a probability for the presence of LCP in the wall of the artery under investigation. The system does not, however, provide information on the depth of the lipid core relative to the lumen. This is effectively a measurement of cap thickness, which is one of the important factors for determining plaque stability. Casuistry suggests [23] that overall features (lipid by NIRS, high attenuation by OCT) coincide in images of diseased coronary arteries in patients. We have previously demonstrated the potential of optical attenuation coefficient by OCT as a tissue characterization method in ex vivo studies [19]. To investigate the ability of atherosclerotic tissue characterization in vivo, we conducted the Optical Coherence Tomography Tissue Type (OC3T) study. In this study, we performed a thorough clinical validation by quantitative evaluation of the attenuation characteristics of LCP as identified by NIRS-IVUS. Specifically, we aimed to investigate the potential of OCT attenuation imaging for differentiation of the superficial and deep lipids, distinguishing thin and thick cap fibroatheromas.

4.2 | Methods

4.2.1 | OC3T study

The Optical Coherence Tomography Tissue Type (OC3T) study was a prospective single-centre study, performed in Thoraxcenter, ErasmusMC, Rotterdam, the Netherlands, enrolling 85 patients undergoing PCI for stable/unstable angina pectoris or acute MI. The study was carried out in accordance with the declarations of Helsinki and was approved by the local ethical review committee. Patients with at least one coronary lesion requiring PCI were included in the study after having provided written informed consent. At least 20 mm of native artery wall accessible to OCT and NIRS-IVUS imaging was required. Patients unable to provide informed written consent, under 18 years of age, with haemodynamic instability, cardiogenic shock and TIMI 0 flow at target lesion were excluded.

OCT and Lipiscan/IVUS pullbacks were performed in a non-culprit native vessel segment.. The imaging region was defined based on angiographic landmarks, such as side-branch take-offs, with a recommended length of >2 cm. Both OCT and NIRS-IVUS were performed in the vessel.

The primary endpoint of the study was a quantification of the relation between OCT attenuation and plaque type, by OCT analysis and by correlation with NIRS.

4.2.2 | NIRS-IVUS

The NIRS-IVUS images were acquired using a hybrid optical/ultrasound catheter (TVC, InfraRedx) [24,25], in compliance with its instructions for use. An automated pullback (0.5 mm/sec and 16 frames per second (fps)) acquired co-registered images of measured probability of LCP presence (P_{LCP}) by NIRS, displayed as a color-coded ring (yellow is high probability, red is low), and gray-scale IVUS (Figure 4.1A). A so-called “chemogram” displays the lipid probability as a fold-out map of the artery with coordinates of longitudinal and circumferential position (Figure 4.1D). This chemogram is co-registered online with IVUS data providing structural information and geographic orientation inside the coronary artery Lipid Core Burden Index (LCBI) is a quantitative measure calculated from the chemogram that represents the fraction of pixels with $P_{LCP} > 0.6$, coloured orange to yellow, in the chemogram, multiplied by a factor of 1000 [7]. The LCBI is a summary measure of the amount of lipid core plaque along the entire length on a 0-1000 scale [26]. In addition to the overall LCBI, the $LCBI_{4mm}$ has been introduced [7,8,27], which provides a metric to quantify LCP in 4 mm segments.

4.2.3 | OCT imaging and image analysis

The OCT images were obtained with C7-XR/Illumien and Dragonfly catheter (St. Jude Medical Inc., St. Paul, MN, USA). Automated OCT pullback (pullback speed 20 mm/s) was performed during simultaneous iso-osmolar X-ray contrast medium (Visipaque 320, GE Healthcare, Buckinghamshire, U.K) delivery through the guide catheter, using a power injector (Medrad ProVis, Bayer HealthCare LLC, NJ, U.S.A; typical flush rate 3.0 ml/s).

The resulting OCT images were then analyzed, to quantify the attenuation coefficient of the tissues, derived from the OCT signal by fitting a single scattering model [19]:

$$\langle I_d \rangle = T(r)S(r)I_0 e^{-\mu_t r} \quad (1)$$

where $T(r)$ and $S(r)$ quantify catheter optics [28] and OCT system dependent changes in the signal with depth in the image, and the parameter of interest is μ_t , the attenuation coefficient. The attenuation calculation and the image analysis were done in Matlab R2012b (The Mathworks, Inc., Natick, MA, USA). The model is fitted in the polar image, in every A-line starting from the edge of the lumen [19,20]. The accuracy of the extracted μ_t is approximately 1 mm^{-1} [19]. The data analysis results in an attenuation image per cross-section of the pullback (Figure 4.1B).

To facilitate the comparison with NIRS-IVUS, we made a longitudinal map of the attenuation data similar to the chemogram. This display depicts tissue optical properties in the entire pullback, sampling a user specified depth window for the maximum value of attenuation from the lumen border to the media as shown in Figure 4.1D. Such a map highlights lipid plaques and other strongly attenuating features in the entire pullback [29] and corresponds well with a visual assessment of LCP in the OCT data by an expert reader [30].

Analogous to the LCBI, we defined the Index of Plaque Attenuation (IPA). IPA is the fraction of pixels in the attenuation map with an attenuation coefficient greater than a certain threshold x , multiplied by a factor of 1000. The calculation of IPA can be represented as a mathematical formula as follows,

$$IPA_x = \frac{N(\mu_t \geq x)}{N_{\text{total}}} \times 1000 \quad (2)$$

where the numerator includes pixels with attenuation greater than certain threshold x .

4.2.4 | Image registration and selection of region of interest

Co-registration of the OCT- and NIRS-IVUS-derived data was achieved by ‘folding out’ the OCT and IVUS pullbacks, as depicted in Figure 4.1C. The largest side-branch within the imaged vessel segment was used as a landmark for longitudinal and angular registration. Subsequently, the maps were cropped to represent the same physical length (Figure 4.1C).

The regions of interest (ROIs) were selected from pullbacks with presence of lipid i.e. $LCBI > 0$. The ROIs for analysis were selected as 4-mm sections with $LCBI_{4\text{mm}} > 150$ in all data sets, computed with a sliding window in the chemogram. The threshold ensures presence of lipid in the majority of segments, but does allow small plaques to be analysed. If all $LCBI_{4\text{mm}} < 150$ in a pullback, the section with the highest $LCBI_{4\text{mm}}$ was selected. In all OCT pullbacks, we selected the 4-mm (20 frames) sections corresponding to the ROIs defined in the NIRS-IVUS data for analysis of the attenuation coefficient. In these OCT ROIs, we manually traced the contour separating the bright intima and dark media to minimize attenuation artefacts associated with the intima-media border, using the proprietary St. Jude Medical analysis

software. The media contour was used as the end of the sampling window per A-line for analysis of the maximum attenuation coefficient. If the media was not visible in a region of an image, the contour in that sector was interpolated [31]. The matched data sets in the chemogram and attenuation images are depicted in Figure 4.1D.

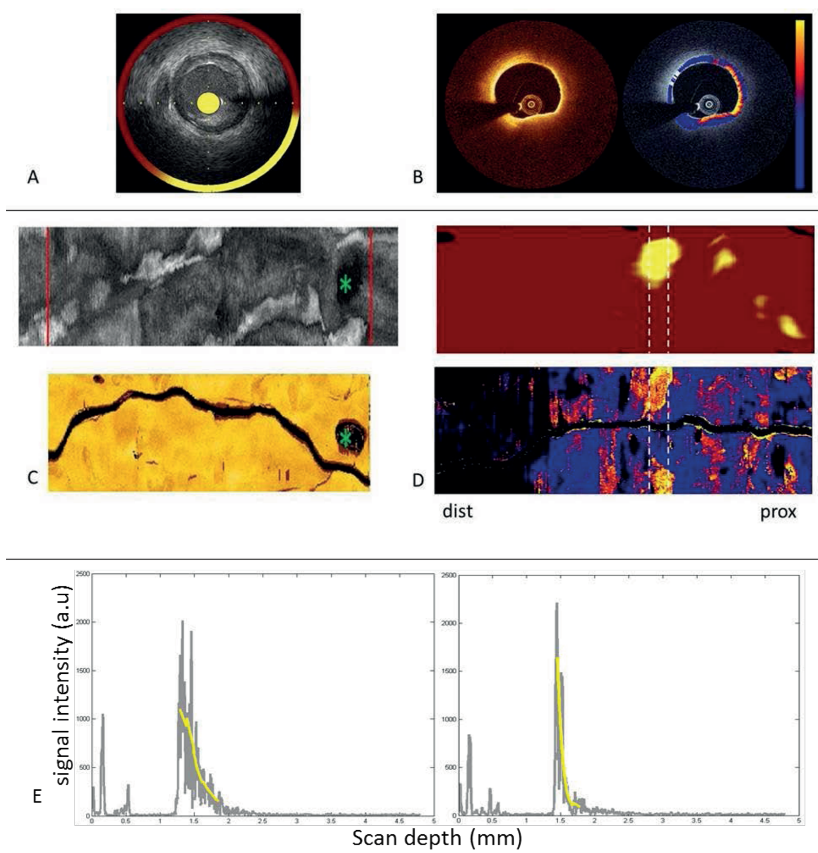


Figure 4.1 | Image acquisition, registration, and display A) Cross-sectional NIRS-IVUS image B) Cross-sectional image of OCT and the corresponding attenuation image (color; blue-red-yellow representing $0\text{--}12\text{ mm}^{-1}$) overlaid on the OCT image (grayscale) C) IVUS and OCT fold out map of a vessel with the largest side branch marked in green asterisk and the cropped region of same physical length represented by red lines D) Chemogram representing the probability of lipid in a coronary artery segment; white dotted lines indicate high LCBI 4-mm block in this pullback; Attenuation map of the same segment depicting the maximum attenuation coefficients in the entire vessel; white dotted lines indicate corresponding selected section. dist- distal, prox-proximal E) Typical A-line of a fibrotic (left) and lipid plaque (right) and the fit from the signal model (yellow line).

4.2.5 | Plaque characterization and cap measurement

Two independent skilled readers (AK and NSvD) analyzed the plaque characteristics by OCT in all ROIs, after reviewing all 20 frames of the selected region. They classified plaque type and, if appropriate, performed a cap thickness measurement. The lesions were classified into fibrous, fibrocalcific (FC) and fibroatheroma (FA) using standard criteria [11]. Mixed plaques were classified as fibroatheromas. In fibroatheromas the thinnest point of the cap in the plaque was selected in the set of 20 frames and measured. Differences in cap thickness and plaque type characterization, resulting from the freedom to choose the frame containing the thinnest cap [32], were resolved by consensus between the two observers. Aided by the cap thickness measurements, fibroatheroma was classified into thin-cap and thick-cap fibroatheromas. Fibroatheroma with less than 65 μm cap thickness was classified as thin-cap fibroatheroma (TCFA) [3].

4.2.6 | Statistical analysis

Continuous variables are presented as mean \pm SD, or median (interquartile range; IQR), and nominal variables as n, (%). Two-sided significance level of p-value was used. We investigated the ability of LCBI and IPA_x to distinguish between TCFA and FA by receiver-operator curve (ROC) analysis, using the experts' classification as the gold standard. LCBI has not been validated for cap thickness evaluation; however, it is the only measurement available to the NIRS user and hence it is interesting to know if a high LCBI is associated with high-risk plaque characteristics such as cap thickness. To establish the relation between lipid detected by NIRS and optical attenuation coefficient, we computed the correlation (Pearson's r) between LCBI and IPA_x for different values of x in all ROIs.

4.3 | Results

4.3.1 | Study population and plaque characterization

A total of 85 patients who underwent both OCT and NIRS-IVUS imaging were included in the study between July 2012 and July 2013. The automated image analysis stringently requires all images in the segment of interest to be free of common image artefacts (e.g. blood in the OCT images), and demands a high accuracy in co-registration of OCT and NIRS-IVUS pullbacks. After the application of these criteria, 61 pullback data sets remained suitable available for analysis. From the 61 patients' data, the selection criteria resulted in 98 regions of 4 mm that forms the dataset for analysis. The baseline characteristics of the analyzed patients are as shown in Table 4.1.

Table 4.1 | Baseline Characteristics

N	61
Age, years	61.9±10
Male	48 (79)
Target vessel	
Left anterior descending artery	24 (40)
Left circumflex artery	13 (20)
Right coronary artery	24 (40)
Medical history	
Hypertension	33 (54)
Dyslipidemia	29 (48)
Diabetes	11 (18)
Smoking	27 (44)
Cardiac family history	30 (49)
Previous MI	18 (30)
Previous PCI	22 (36)
Previous CABG	1 (1)

Patient characteristics of analyzable data. Values are mean±SD or n (%). *Abbreviations:* CABG, coronary artery bypass graft; MI, myocardial infarction; PCI, percutaneous coronary intervention.

The two OCT experts reached a consensus classification for all 98 segments of interest, presented in Table 4.2. The cap thickness measurements in the FA and TCFA categories and the LCBI and IPA values for all the categories are also listed.

Table 4.2 | Consensus Plaque type classification

	Fibrocalcific	Fibrous	Fibroatheroma	TCFA
No.	5	8	70	15
Cap thickness (microns)	NA	NA	150±62	54±8
LCBI	285±93	151±106	260±145	330±153
IPA	115±54	22±28	70±45	140±68

Plaque characterization. Cap thickness, LCBI and IPA values are mean±SD.

4.3.2 | Detection of lipid-core plaque and thin cap fibroatheroma

The maximum correlation coefficient between LCBI_{4mm} and IPA was found for a threshold of $x=6\text{ mm}^{-1}$, and equaled $r=0.4$, (see Supplementary Figure 4.1).

Using the readers' characterization as classifier, ROC curves were made for IPA values with different attenuation thresholds x as well as for LCBI. IPA with threshold 11 mm^{-1} (denoted IPA₁₁) has the greatest area under the curve (AUC), making it the strongest differentiator between FA and TCFA. Figure 4.2

shows the ROC curves for LCBI and IPA_{11} . The best cut-off value of IPA_{11} is 110, which minimize the distance between the curve and the upper corner of the ROC curve [33], for the differentiation.

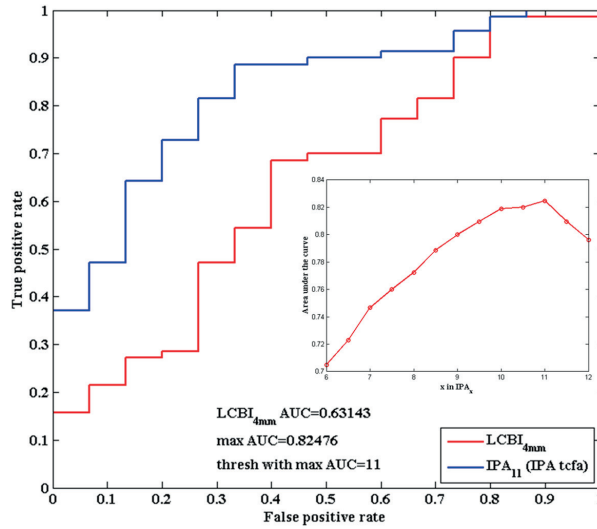


Figure 4.2 | ROC curves for FA and TCFA differentiation. OC curves of $LCBI_{4mm}$ and IPA_{11} for the ability to differentiate FA and TCFA with the OCT readers classification as ground truth. The AUC values indicate that IPA_{11} has the maximum ability to differentiate FA and TCFA. The inset plot shows the area under the curves for different thresholds 'x' in IPA_x . Abbreviations: FA, Fibroatheroma; TCFA, Thin cap fibroatheroma; LCBI, Lipid core burden index; IPA, Index of Plaque attenuation; AUC, Area under the curve.

IPA_{11} was significantly higher in TCFA compared to FA ($p < 0.0001$; Figure 4.3). Although the LCBI was also higher in TCFA compared to FA, this difference did not reach significance ($p = 0.097$) for discrimination between thick and thin cap LCP. Table 4.2 shows the mean values with standard deviation for these variables.

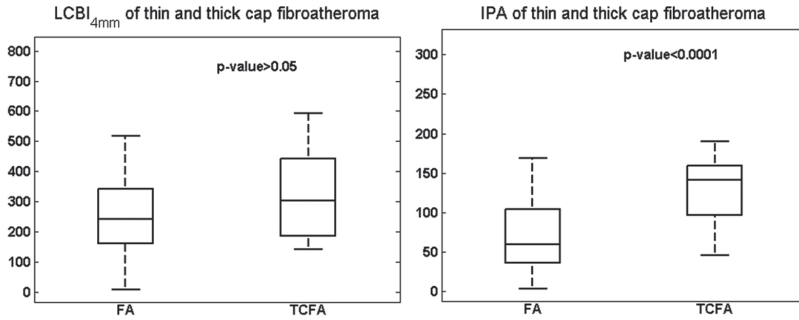


Figure 4.3 | Boxplot of LCBI and IPA values in thin cap and thick cap fibroatheromas. Median LCBI_{4mm} was 242 (interquartile range: 161-342) for FA, for TCFA 302 (IQR187-442) ($p=0.10$). Median IPA₁₁ for FA was 60 (37-103) which was significantly lower than in TCFA (median 141 (98-159); $p<0.0001$). IPA₁₁ can significantly differentiate ($p<0.0001$) whereas the differentiation based on LCBI_{4mm} is not significant ($p>0.05$). *Abbreviations:* FA, Fibroatheroma; TCFA, Thin cap fibroatheroma; LCBI, Lipid core burden index; IPA, Index of Plaque attenuation.

4.4 | Discussion

This study introduces the index of plaque attenuation (IPA), a bias-free and reproducible summary measurement of attenuating structures in the coronary vessels. Highly attenuating features have been linked to histopathological markers of plaque vulnerability. This study aimed to validate optical attenuation as a plaque characterization tool *in vivo*. The main finding of our study was that an OCT-derived marker of plaque attenuation, the fraction of image pixels with optical attenuation greater than 11 mm⁻¹ (IPA₁₁), can reliably differentiate between thin and thick cap fibroatheroma. It is superior compared to LCBI for making this distinction. Deeper lipids exhibit reduced attenuation in OCT images, which enables the discrimination of TCFA and FA by IPA₁₁. The correlation between IPA and LCBI is modest, a finding that indicates a limited specificity of optical attenuation to detect lipid overall (see supplementary discussion). Fibrocalcific plaques in the data set also exhibit elevated IPA₁₁, albeit significantly ($p=0.02$) lower than TCFA. The contrast between FC and TCFA is similar for LCBI and IPA₁₁, so the FC plaques apparently also contain lipid. Previously published data on attenuation of purely (non-lipidic) calcified plaques shows these have low attenuation [20,23].

The ability of NIRS-IVUS to detect the lipid core plaques that may cause peri-procedural MI [7] and STEMI [34] has been shown before with the use of the maximum 4-mm LCBI to detect lipid core plaques, demonstrating how intravascular imaging can be a powerful tool to identify the lipid core plaques that may be unstable [35]. Similarly, qualitative OCT assessment of plaque morphology offers potential to influence clinical decision making during PCI and risk assessment [36,37], as observed with NIRS [7]. Automatic computation of OCT plaque attenuation could potentially be integrated in future clinical practice because it can highlight the presence of TCFA in a complete pullback, without the need for a time-consuming frame-by-frame inspection and manual measurements in the pullback

data. OCT-derived IPA_{11} may be a feasible method to detect LCP with a thin cap, an important indicator for plaque instability [3]. In a clinical application, realistic implementation would include automatic media segmentation as discussed above, after which the attenuation analysis can be overlaid on the OCT images. The carpet display (see Figure 4.1B) and colour coded IPA_{11} displayed on the longitudinal section (similar to the block chemogram used in NIRS), would enable direct overall assessment of plaque in the artery to guide revascularization procedures. The utility of such a tool would need to be evaluated in a dedicated study enrolling a larger group of patients. Application to large data sets will be facilitated by automated media segmentation, a tool that is currently being developed in our institute [38]. Our study results reiterate that 4-mm LCBI was not designed to quantify cap thickness, and indeed cannot reliably differentiate the thin and thick cap fibroatheroma.

4.4.1 | Limitations

This study has several limitations. The selection of plaques was based on the lipid positive regions identified with LCBI calculated from NIRS data. This means that the optical attenuation of non-lipid plaque was not included. Highly attenuating features that are not associated with LCP, such as superficial macrophage foam cells [39], would reduce the specificity of OCT-based plaque detection. This is true also for qualitative OCT plaque characterization, and is recognized as one of the major pitfalls in OCT image interpretation [11,40]. Such attenuating features that are not associated with LCP also lead to the modest correlation between LCBI and IPA overall (see Supplementary Discussion).

The spatial resolution and data complexity is quite different for NIRS and OCT. While by a strict definition NIRS is not an imaging technology with a well-defined resolution, it is clear that the averaging kernel with which the data is being acquired is much larger for NIRS than for OCT. Also, NIRS provides a single spectroscopic measurement per A-line. We reduced the information content of the OCT data to accommodate the validation of OCT attenuation by NIRS data. This simplification consisted of the reduction of the OCT measurements to a single value per A-line, and an area measurement of high attenuation per 4 mm segment. This procedure undoubtedly loses image features that could be helpful in tissue characterization. Further exploratory studies on clinical data [38] and more extensive comparisons of OCT signal analysis with histology are ongoing to address these limitations.

The pullback images, especially IVUS, suffer from longitudinal motion artefacts that result in imperfect co-registration [41]. Inclusion of multiple fiducial points may remedy this problem, but as landmarks are often visible multiple times in an IVUS pullback, this is a delicate procedure. Since we process the data in 4-mm blocks (larger than the anticipated mismatch), and do not require accurate circumferential image matching, the final effect on our quantitative data is limited.

4.5 | Conclusion

We validated OCT-derived optical attenuation as a tissue characterization tool. We expressed plaque attenuation in a local measure of highly attenuating tissue, the index of plaque attenuation (IPA_x), where x is the threshold for high attenuation in mm^{-1} . IPA_{11} can differentiate TCFA and FA with high sensitivity and specificity. This analysis might allow a fast and accurate TCFA detection in pullback data sets without requiring inspection of every individual frame.

4.6 | Perspectives

Competency in Patient Care and Procedural Skills: This newly introduced index of tissue optical attenuation enables a fast and reproducible interpretation of plaque morphology in everyday clinical application of OCT.

Translational Outlook: Automated analysis of complete OCT pullbacks, which can indicate thin cap lipid core plaques, can provide guidance in PCI.

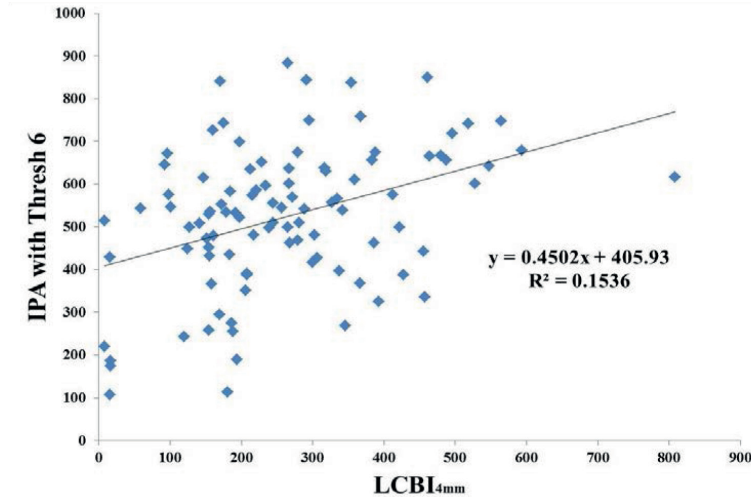
4.7 | Acknowledgements

The authors acknowledge the funding from the Dutch Heart Foundation (2010B064). The authors also would like to acknowledge Prof. Dr. Yoshifumi Saijo, Dr. Frank Gijzen, Dr. Jolanda Wentzel and Dr. Pieter Kruizinga for their contributions in the discussions. We thank Dr. Thomas Johnson for critical commenting on the manuscript.

4S.1 | Supplementary discussion

4S.1.1 | Relation between NIRS lipid and optical attenuation

Upon computation of the correlation between IPA and LCBI, we found the maximum r for $x = 6 \text{ mm}^{-1}$ in IPA calculation. The correlation between the IPA_6 and LCBI was modest ($r=0.4$) as shown in Figure 4S.1. Of the 98 plaques, 15 plaques had also calcification by OCT which could be one of the influencing factors.



Supplementary Figure 4S.1 | Correlation of $\text{LCBI}_{4\text{mm}}$ with IPA_6 . Correlation between the $\text{LCBI}_{4\text{mm}}$ and IPA with threshold 6 mm^{-1} . *Abbreviations:* LCBI, Lipid core burden index; IPA, Index of plaque attenuation.

A straightforward explanation for the modest correlation of OCT-derived optical attenuation coefficient with probability of LCP by NIRS may be the fact that there are more attenuating tissues than lipid-rich necrotic core alone, macrophages chiefly among them. We also observed that a thick layer of overlaying tissue tends to reduce the attenuation coefficient, likely as a result of multiple scattering processes [42]. The LCBI is by nature less prone to this effect of overlaying tissue layers. The reduced attenuation of deeper lipid supports the second finding of this study: a significant difference between thin and thick cap fibroatheroma by OCT-based IPA_{11} . This moderate overall agreement in detection of lipids between OCT and NIRS has also been demonstrated by a previous study, performed with non-automated analysis of plaque morphology by OCT [43]. In our study, we utilised the OCT attenuation coefficient, an optical parameter which can be automatically computed from the data, and as such does not suffer from user variability. The comparison between LCBI and IPA is further facilitated by the fact that both are relative area measurements, which the OCT-based product of lipid arc and lipid length is not. LCBI and IPA do not necessarily measure the same tissue property, as is evident from the correlation coefficient.

Discrepancies in the correlation of IPA with LCBI were found both for plaques with low, as well as with high IPA. High IPA (large area with attenuation above the threshold value) with low LCBI may be attributed to attenuation by the foam cells or macrophages which may cover a larger area than the LCP itself, thus giving a false positive diagnosis of lipid presence by OCT. The prominence of macrophage attenuation is related to their often superficial occurrence, even in early lesions. Macrophages are a common confounder in OCT image interpretation [44] and the main source of false positives in LCP detection by attenuation imaging. Similarly, fibroatheromas with a calcified core might be misidentified by NIRS, giving a false negative diagnosis for LCP [45], while appearing as highly attenuating structures on OCT. Conversely, deep or small lipid pools are a leading cause of false-positive LCP by NIRS [45] but may still have low OCT attenuation. Likewise, mixed plaques with calcification may have less signal attenuation than the non-calcified necrotic cores, resulting in lower IPA, which could be a source of false-negatives, reducing the area under the curve in the ROC analysis. NIRS suffers from the same limitation but not necessarily equally strongly (Table 4S.1).

Supplementary Table 4S.1 | Thin cap fibroatheroma detection.

	NIRS	OCT
False Positive	Deep lipid pools	Superficial Macrophages
False Negative	Fibroatheromas with calcification	Fibroatheromas with calcification

References

1. Falk E, Shah PK, Fuster V. Coronary plaque disruption. *Circulation* 1995;92:657-671.
2. Schaar JA, Muller JE, Falk E, Virmani R, Fuster V, Serruys PW, Colombo A, Stefanadis C, Ward Casscells S, Moreno PR, Maseri A, van der Steen AF. Terminology for high-risk and vulnerable coronary artery plaques. Report of a meeting on the vulnerable plaque, June 17 and 18, 2003, Santorini, Greece. *European heart journal* 2004;25:1077-1082.
3. Virmani R, Kolodgie FD, Burke AP, Farb A, Schwartz SM. Lessons From Sudden Coronary Death: A Comprehensive Morphological Classification Scheme for Atherosclerotic Lesions. *Arteriosclerosis, thrombosis, and vascular biology* 2000;20:1262-1275.
4. Waxman S, Freilich MI, Suter MJ, Shishkov M, Bilazarian S, Virmani R, Bouma BE, Tearney GJ. A case of lipid core plaque progression and rupture at the edge of a coronary stent: elucidating the mechanisms of drug-eluting stent failure. *Circ Cardiovasc Interv* 2010;3:193-196.
5. Goldstein JA, Grines C, Fischell T, Virmani R, Rizik D, Muller J, Dixon SR. Coronary embolization following balloon dilation of lipid-core plaques. *JACC Cardiovasc Imaging* 2009;2:1420-1424.
6. Tanaka A, Imanishi T, Kitabata H, Kubo T, Takarada S, Tanimoto T, Kuroi A, Tsujioka H, Ikejima H, Komukai K, Kataiwa H, Okouchi K, Kashiwaghi M, Ishibashi K, Matsumoto H, Takemoto K, Nakamura N, Hirata K, Mizukoshi M, Akasaka T. Lipid-rich plaque and myocardial perfusion after successful stenting in patients with non-ST-segment elevation acute coronary syndrome: an optical coherence tomography study. *European heart journal* 2009;30:1348-1355.
7. Goldstein JA, Maini B, Dixon SR, Brilakis ES, Grines CL, Rizik DG, Powers ER, Steinberg DH, Shunk KA, Weisz G, Moreno PR, Kini A, Sharma SK, Hendricks MJ, Sum ST, Madden SP, Muller JE, Stone GW, Kern MJ. Detection of Lipid-Core Plaques by Intracoronary Near-Infrared Spectroscopy Identifies High Risk of Periprocedural Myocardial Infarction. *Circulation: Cardiovascular Interventions* 2011;4:429-437.
8. Madder RD, Smith JL, Dixon SR, Goldstein JA. Composition of Target Lesions by Near-Infrared Spectroscopy in Patients With Acute Coronary Syndrome Versus Stable Angina. *Circ-Cardiovasc Interv* 2012;5:55-61.
9. Kini AS, Motoyama S, Vengrenyuk Y, Feig JE, Pena J, Baber U, Bhat AM, Moreno P, Kovacic JC, Narula J, Sharma SK. Multimodality Intravascular Imaging to Predict Periprocedural Myocardial Infarction During Percutaneous Coronary Intervention. *JACC Cardiovasc Interv* 2015;8:937-945.
10. Regar E, Ligthart J, Bruining N, van Soest G. The diagnostic value of intracoronary optical coherence tomography. *Herz* 2011;36:417-428.
11. Tearney GJ, Regar E, Akasaka T, Adriaenssens T, Barlis P, Bezerra HG, Bouma B, Bruining N, Cho JM, Chowdhary S, Costa MA, de Silva R, Dijkstra J, Di Mario C, Dudek D, Falk E, Feldman MD, Fitzgerald P, Garcia-Garcia HM, Gonzalo N, Granada JF, Guagliumi G, Holm NR, Honda Y, Ikeno F, Kawasaki M, Kochman J, Koltowski L, Kubo T, Kume T, Kyono H, Lam CC, Lamouche G, Lee DP, Leon MB, Maehara A, Manfrini O, Mintz GS, Mizuno K, Morel MA, Nadkarni S, Okura H, Otake H, Pietrasik A, Prati F, Raber L, Radu MD, Rieber J, Riga M, Rollins A, Rosenberg M, Sirbu V, Serruys PW, Shimada K, Shinke T, Shite J, Siegel E, Sonoda S, Suter M, Takarada S, Tanaka A, Terashima M, Thim T, Uemura S, Ughi GJ, van Beusekom HM, van der Steen AF, van Es GA, van Soest G, Virmani R, Waxman S, Weissman NJ, Weisz G, International Working Group for Intravascular Optical Coherence Tomography. Consensus standards for acquisition, measurement, and reporting of intravascular optical coherence tomography studies: a report from the International Working Group for Intravascular Optical Coherence Tomography Standardization and Validation. *J Am Coll Cardiol* 2012;59:1058-1072.
12. Guagliumi G, Musumeci G, Sirbu V, Bezerra HG, Suzuki N, Fiocca L, Matiashvili A, Lortkipanidze N, Trivisonno A, Valsecchi O, Biondi-Zoccai G, Costa MA, Investigators OT. Optical coherence tomography assessment of in vivo vascular response after implantation of overlapping bare-metal and drug-eluting stents. *JACC Cardiovascular interventions* 2010;3:531-539.
13. Guagliumi G, Costa MA, Sirbu V, Musumeci G, Bezerra HG, Suzuki N, Matiashvili A, Lortkipanidze N, Mihalcsik L, Trivisonno A, Valsecchi O, Mintz GS, Dressler O, Parise H, Maehara A, Cristea E, Lansky AJ, Mehran R, Stone GW. Strut coverage and late malapposition with paclitaxel-eluting stents compared with bare metal stents in acute myocardial infarction: optical coherence tomography substudy of the Harmonizing Outcomes with Revascularization and Stents in Acute Myocardial Infarction (HORIZONS-AMI) Trial. *Circulation* 2011; 123:274-281.

14. Prati F, Romagnoli E, Burzotta F, Limbruno U, Gatto L, La Manna A, Versaci F, Marco V, Di Vito L, Imola F, Paoletti G, Trani C, Tamburino C, Tavazzi L, Mintz GS. Clinical Impact of OCT Findings During PCI: The CLI-OPCI II Study. *JACC Cardiovasc Imaging* 2015;8:1297-1305.
15. Yabushita H, Bouma BE, Houser SL, Aretz T, Jang IK, Schlendorf KH, Kauffman CR, Shishkov M, Kang DH, Halpern EF, Tearney GJ. Characterization of human atherosclerosis by optical coherence tomography. *Circulation* 2002;106:1640-1645.
16. Kume T, Akasaka T, Kawamoto T, Watanabe N, Toyota E, Neishi Y, Sukmawan R, Sadahira Y, Yoshida K. Assessment of coronary arterial plaque by optical coherence tomography. *The American journal of cardiology* 2006;97:1172-1175.
17. Levitz D, Thrane L, Frosz M, Andersen P, Andersen C, Andersson-Engels S, Valanciunaite J, Swartling J, Hansen P. Determination of optical scattering properties of highly-scattering media in optical coherence tomography images. *Opt Express* 2004;12:249-259.
18. van der Meer FJ, Faber DJ, Baraznji Sassoon DM, Aalders MC, Pasterkamp G, van Leeuwen TG. Localized measurement of optical attenuation coefficients of atherosclerotic plaque constituents by quantitative optical coherence tomography. *IEEE Trans Med Imaging* 2005;24:1369-1376.
19. van Soest G, Goderie T, Regar E, Koljenovic S, van Leenders GL, Gonzalo N, van Noorden S, Okamura T, Bouma BE, Tearney GJ, Oosterhuis JW, Serruys PW, van der Steen AF. Atherosclerotic tissue characterization in vivo by optical coherence tomography attenuation imaging. *J Biomed Opt* 2010;15:011105.
20. Ughi GJ, Adriaenssens T, Sinnaeve P, Desmet W, D'Hooge J. Automated tissue characterization of in vivo atherosclerotic plaques by intravascular optical coherence tomography images. *Biomed Opt Express* 2013;4:1014-1030.
21. Moreno PR. Detection of Lipid Pool, Thin Fibrous Cap, and Inflammatory Cells in Human Aortic Atherosclerotic Plaques by Near-Infrared Spectroscopy. *Circulation* 2002;105:923-927.
22. Gardner CM, Tan H, Hull EL, Lisauskas JB, Sum ST, Meese TM, Jiang C, Madden SP, Caplan JD, Burke AP, Virmani R, Goldstein J, Muller JE. Detection of lipid core coronary plaques in autopsy specimens with a novel catheter-based near-infrared spectroscopy system. *JACC Cardiovasc Imaging* 2008;1:638-648.
23. Regar E, Gnanadesigan M, Van der Steen AF, van Soest G. Quantitative optical coherence tomography tissue-type imaging for lipid-core plaque detection. *JACC Cardiovasc Interv* 2013;6:891-892.
24. Garg S, Serruys PW, van der Ent M, Schultz C, Mastik F, van Soest G, van der Steen AF, Wilder MA, Muller JE, Regar E. First use in patients of a combined near infra-red spectroscopy and intra-vascular ultrasound catheter to identify composition and structure of coronary plaque. *EuroIntervention* 2010;5:755-756.
25. Schultz CJ, Serruys PW, van der Ent M, Ligthart J, Mastik F, Garg S, Muller JE, Wilder MA, van de Steen AF, Regar E. First-in-man clinical use of combined near-infrared spectroscopy and intravascular ultrasound: a potential key to predict distal embolization and no-reflow? *J Am Coll Cardiol* 2010;56:314.
26. de Boer SP, Brugaletta S, Garcia-Garcia HM, Simsek C, Heo JH, Lenzen MJ, Schultz C, Regar E, Zijlstra F, Boersma E, Serruys PW. Determinants of high cardiovascular risk in relation to plaque-composition of a non-culprit coronary segment visualized by near-infrared spectroscopy in patients undergoing percutaneous coronary intervention. *European heart journal* 2014; 35:282-289.
27. Maddar RD, Goldstein JA, Madden SP, Puri R, Wolski K, Hendricks M, Sum ST, Kini A, Sharma S, Rizik D, Brilakis ES, Shunk KA, Petersen J, Weisz G, Virmani R, Nicholls SJ, Maehara A, Mintz GS, Stone GW, Muller JE. Detection by Near-Infrared Spectroscopy of Large Lipid Core Plaques at Culprit Sites in Patients With Acute ST-Segment Elevation Myocardial Infarction. *JACC: Cardiovascular Interventions* 2013;6:838-846.
28. van Leeuwen TG, Faber DJ, Aalders MC. Measurement of the axial point spread function in scattering media using single-mode fiber-based optical coherence tomography. *Ieee J Sel Top Quant* 2003;9:227-233.
29. Gnanadesigan M, van Soest G, White S, Scoltock S, Ughi GJ, Baumbach A, van der Steen AFW, Regar E, Johnson TW. Effect of temperature and fixation on the optical properties of atherosclerotic tissue: a validation study of an ex-vivo whole heart cadaveric model. *Biomedical optics express* 2014;5:1038-1049.
30. Karanasos A, Simsek C, Gnanadesigan M, van Ditzhuijzen NS, Freire R, Dijkstra J, Tu S, Van Mieghem N, van Soest G, de Jaegere P, Serruys PW, Zijlstra F, van Geuns RJ, Regar E. OCT assessment of the long-term vascular healing response 5 years after everolimus-eluting bioresorbable vascular scaffold. *J Am Coll Cardiol* 2014;64:2343-2356.

31. Kubo T, Yamano T, Liu Y, Ino Y, Shiono Y, Orii M, Taruya A, Nishiguchi T, Shimokado A, Teraguchi I, Tanimoto T, Kitabata H, Yamaguchi T, Hirata K, Tanaka A, Akasaka T. Feasibility of Optical Coronary Tomography in Quantitative Measurement of Coronary Arteries With Lipid-Rich Plaque. *Circ J* 2015;79:600-606.
32. Kim SJ, Lee H, Kato K, Yonetsu T, Xing L, Zhang S, Jang IK. Reproducibility of in vivo measurements for fibrous cap thickness and lipid arc by OCT. *JACC Cardiovasc Imaging* 2012;5:1072-1074.
33. Kang SJ, Lee JY, Ahn JM, Song HG, Kim WJ, Park DW, Yun SC, Lee SW, Kim YH, Mintz GS, Lee CW, Park SW, Park SJ. Intravascular ultrasound-derived predictors for fractional flow reserve in intermediate left main disease. *JACC Cardiovasc Interv* 2011;4:1168-1174.
34. Madder RD, Goldstein JA, Madden SP, Puri R, Wolski K, Hendricks M, Sum ST, Kini A, Sharma S, Rizik D, Brilakis ES, Shunk KA, Petersen J, Weisz G, Virmani R, Nicholls SJ, Maehara A, Mintz GS, Stone GW, Muller JE. Detection by near-infrared spectroscopy of large lipid core plaques at culprit sites in patients with acute ST-segment elevation myocardial infarction. *JACC Cardiovascular interventions* 2013;6:838-846.
35. Uemura S. Invasive imaging of vulnerable atherosclerotic plaques in coronary artery disease. *Circulation journal: official journal of the Japanese Circulation Society* 2013;77:869-875.
36. Lee T, Yonetsu T, Koura K, Hishikari K, Murai T, Iwai T, Takagi T, Iesaka Y, Fujiwara H, Isobe M, Kakuta T. Impact of Coronary Plaque Morphology Assessed by Optical Coherence Tomography on Cardiac Troponin Elevation in Patients With Elective Stent Implantation. *Circ-Cardiovasc Inte* 2011;4:378-386.
37. Imola F, Mallus MT, Ramazzotti V, Manzoli A, Pappalardo A, Di Giorgio A, Albertucci M, Prati F. Safety and feasibility of frequency domain optical coherence tomography to guide decision making in percutaneous coronary intervention. *EuroIntervention* 2010;6:575-581.
38. Zahnd G, Karanasos A, van Soest G, Regar E, Niessen W, Gijzen F, van Walsum T. Quantification of fibrous cap thickness in intracoronary optical coherence tomography with a contour segmentation method based on dynamic programming. *Int J Comput Assist Radiol Surg* 2015.
39. Kashiwagi M, Kitabata H, Ozaki Y, Imanishi T, Akasaka T. Fatty streak assessed by optical coherence tomography: early atherosclerosis detection. *Eur Heart J Cardiovasc Imaging* 2013;14:109.
40. van Soest G, Regar E, Goderie TP, Gonzalo N, Koljenovic S, van Leenders GJ, Serruys PW, van der Steen AF. Pitfalls in plaque characterization by OCT: image artifacts in native coronary arteries. *JACC Cardiovasc Imaging* 2011;4:810-813.
41. van Ditzhuijzen NS, Karanasos A, Bruining N, van den Heuvel M, Sorop O, Ligthart J, Witberg K, Garcia-Garcia HM, Zijlstra F, Duncker DJ, van Beusekom HM, Regar E. The impact of Fourier-Domain optical coherence tomography catheter induced motion artefacts on quantitative measurements of a PLLA-based bioresorbable scaffold. *Int J Cardiovasc Imaging* 2014;30:1013-1026.
42. Thrane L, Yura HT, Andersen PE. Analysis of optical coherence tomography systems based on the extended Huygens-Fresnel principle. *Journal Of The Optical Society Of America A-Optics Image Science And Vision* 2000; 17:484-490.
43. Yonetsu T, Suh W, Abtahian F, Kato K, Vergallo R, Kim SJ, Jia H, McNulty I, Lee H, Jang IK. Comparison of near-infrared spectroscopy and optical coherence tomography for detection of lipid. *Catheterization and cardiovascular interventions : official journal of the Society for Cardiac Angiography & Interventions* 2013.
44. van Soest G, Regar E, Goderie TP, Gonzalo N, Koljenovic S, van Leenders GJ, Serruys PW, van der Steen AF. Pitfalls in plaque characterization by OCT: image artifacts in native coronary arteries. *JACC Cardiovasc Imaging* 2011;4:810-813.
45. Gardner CM, Tan H, Hull EL, Lissauskas JB, Sum ST, Meese TM, Jiang C, Madden SP, Caplan JD, Burke AP, Virmani R, Goldstein J, Muller JE. Detection of lipid core coronary plaques in autopsy specimens with a novel catheter-based near-infrared spectroscopy system. *JACC Cardiovasc Imaging* 2008;1:638-648.

Chapter 5

Qualitative comparison of automated tissue characterization methods in intravascular optical coherence tomography ex-vivo

Muthukaruppan Gnanadesigan, Steve White, Giovanni Ughi,
Lambros Athanasiou, Taylor Hoyt, Jan van der Thüsen,
Heleen van Beusekom, Thomas W Johnson, Dimitrios Fotiadis,
Jeniffer Phipps, Marc Feldman, Gary Tearney,
Antonius FW van der Steen and Gijs van Soest

Manuscript in preparation

Abstract

Optical coherence tomography is a widely used morphological tool that provides high-resolution images of the arterial wall. The OCT images allow tissue characterization of the atherosclerotic plaques by the various analysis methods. Several methods have recently been developed to provide fast and robust tissue characterization of OCT. In this study, we qualitatively compare some of these methods by analyzing a set of ex-vivo data. The presented methods are valuable in understanding of the atherosclerosis process.

5.1 | Introduction

Coronary artery disease (CAD) is the major clinical manifestation of atherosclerosis, a focal thickening of intima that leads to formation of asymmetric complex lesions as the disease progresses. CAD is one of the major causes of death worldwide [1]. The tissue composition of the atherosclerotic plaque can play an important role in the prediction of its instability [2]. The detection of tissue types like a lipid core has implications in coronary intervention. Lipid core plaques have been implicated in peri-procedural and follow-up events [3-7]. Coronary angiography only provides visualization of the arterial lumen, but not of the vessel wall, needed to assess atherosclerotic plaque progression [8,9]. Intravascular imaging techniques overcome the inherent limitations, like the resolution and the arterial view, of x-ray angiographic imaging.

Intravascular optical coherence tomography is a popular clinical tool for stent placement and optimization by imaging the lumen and wall morphology [10-13]. OCT is a high resolution catheter based imaging modality that not only provides assessment of luminal measurements and morphology but also allows qualitative assessment of tissue composition of the plaque [6,12,13]. The tissue components of atherosclerotic plaque have different morphology, appearance and optical parameters, and this allows for the development of tissue characterization methods based on IV-OCT images. Automated plaque characterization methods may assist image interpretation by OCT users. Since the introduction of IV-OCT to clinical imaging in interventional cardiology, several methodologies have been developed to perform robust and automated analysis for tissue characterization.

The different atherosclerotic tissue types that are of interest and can be potentially be discriminated by OCT are: lipid core present in fibroatheroma and mixed plaque; calcified tissue; fibrotic tissue; and regions of inflammation appearing superficially or inside lipid core plaque. Inflamed tissue is characterized by dense infiltration with macrophages.

Tearney et al. [14] proposed a quantification of macrophage content by calculating the standard deviation of the OCT intensity, a measure of the variability of the OCT signal in a sample area of the image. The method quantifies macrophage proliferation in fibrous cap within a selected region of interest (ROI). The authors calculated normalized standard deviation (NSD) for 26 lipid rich plaques, and compared it to measurements of macrophage positive area in an appropriate histology staining. There was a high degree of correlation between OCT and histological measurements of fibrous cap macrophage density. The authors proposed that the high NSD is due to the difference in refractive index of the macrophages and their surrounding fibrous tissue.

The presence of cells with strong optical scattering generates the variability measured by NSD, which can also be automatically quantified as “bright spots”. Phipps et al. [15] used this hypothesis and proposed that the bright spots can also occur in the interfaces between plaque components where there are sharp differences in refractive indices. Their algorithm detects bright spots in the entire depth of the artery based on distance from catheter, SNR of the OCT and tissue depth. They analyzed 1599 OCT images

from 14 vessels and compared with histology. Their results suggest that macrophages alone were responsible only for 23% of the bright spot regions, while the other etiologies for the bright spots were cellular fibrous tissue, interfaces between calcium and fibrous tissue, calcium and lipids, and fibrous cap and lipid pool.

The attenuation coefficient is a robust tissue optical parameter [16] that has been proposed for tissue characterization [17-19]. The plaque characterization by Van Soest et al. uses the attenuation coefficient calculated by fitting the OCT data to a signal model. The results show lipid-rich necrotic core and macrophage infiltration have high attenuation compared to fibrous tissue and other plaque components. The method is a fully automated analysis on a speckle reduced A-line of OCT from lumen border resulting in an attenuation image, which is color-coded for guidance.

Image texture can also be related to tissue composition, by extracting statistical metrics from local regions in the image and creating classifiers by matching with histological interpretation. Athanasiou et al. [20] proposed a fully automated method that relies on the processing of the OCT images from lumen border to 1.5 mm. They use a K-means algorithm to segment atherosclerotic tissue and calcium, supplemented with a classification algorithm to categorize the atherosclerotic tissue into lipid, fibrous, and mixed tissue.

The aim of this study is to present the different methods for tissue characterization in IV-OCT and perform a qualitative comparison of their ability to identify the different plaque tissues by running the respective analyses on a common data set of ex-vivo images. We then classified the plaque type and the various tissue components therein by interpretation of the histology, using series of histochemical and immunohistochemical stains.

5.2 | Materials and methods

5.2.1 | Specimens

A total of 23 vessels were obtained at two centers, ErasmusMC and Bristol Heart institute. We obtained 17 coronary arteries from the Department of Pathology of the Erasmus MC at autopsy. Consent was obtained from the relatives and the protocol was sanctioned by the Medical Ethics Committee of the Erasmus MC. The coronary arteries were frozen within 2h at -80° , then thawed and measured within 2 months. In the measurement, we fixed the specimen on top of a custom built plastic tissue holder with an array of 200 μm thick metal wires glued to the bottom at 1.5 mm intervals [21]. Whole cadaveric hearts used were obtained from the Bristol Heart Valve Bank and excised within 48 hours post-mortem and stored at 4°C [22]. A short guide catheter was introduced into the right coronary artery to facilitate intravascular imaging and fixed in position with sutures. All tissues were handled in accordance with the local ethics regulations. The heart specimen was held within a custom-built Perspex container, with adapters on both sides of the lid allowing connection of the guide internally, and a Y-connector and pressure/injector manifold externally [22]. For the study a total of 6 heart specimens were imaged.

5.2.2 | IV-OCT imaging

The OCT system used for imaging at both the Bristol Heart Institute and the Erasmus MC institutes was a C7-XR with Dragonfly catheter (St. Jude Medical Inc. St. Paul, MN, U.S.A), performing pullback acquisitions at a rate of 100 frames per second and a pullback speed of 20 mm/s. For experiments at Erasmus MC, the tissue holder was placed inside a water tank filled with saline solution at room temperature and pullback data was obtained. At the Bristol Heart Institute, the imaged artery was perfused with phosphate buffered saline (PBS) and the intracoronary pressure was maintained at 100 mmHg. The end of the guide catheter served as a reference point.

5.2.3 | Histology and plaque characterization

The histologic processing at Erasmus MC used the following protocol: After imaging, the arteries were cut at the two wires adjacent to the imaging plane, embedded in optimal cutting temperature compound (Tissue-Tek®, Sakura Finetek Europe B.V.), and then were frozen on dry ice, and stored at -80°C until further processing. For histopathology, a series of 10 µm thick sections were thaw mounted on slides and stained with Oil Red O (ORO) to identify lipids in the artery (lipids are stained red in ORO staining), Haematoxylin and Eosin (H&E), Cluster of Differentiation 68 (CD68) and Resorcin-Fuchsin (RF).

At the Bristol Heart institute, the imaged vessels were pressure-fixed while still on the heart with buffered formalin at 100 mmHg for 15 minutes, excised from the heart, and fixed with buffered formalin for 24 hours. Then the vessels were embedded in paraffin and cut into 4-mm blocks with the end of the guide catheter serving as a reference. The proximal face of each block was cut at 3 µm thickness for histological analysis and serial sections stained with Haematoxylin and Eosin (H&E), Elastic Van Gieson (EVG), Cluster of Differentiation 68 (CD68) and smooth muscle cell α -Actin stains. CD68 and α -Actin were visualized using mouse anti-CD68 (DAKO M0814 and M0876 mixed 1/200 of each), and mouse anti- α actin (DAKO, M0851 1/200), or matched mouse IgG control, followed by biotinylated goat anti-mouse and extravidin-HRP conjugate with DAB staining.

Forty atherosclerotic plaques were identified from the ex-vivo specimens. Two skilled pathologists analyzed the plaque characteristics by the histological staining and classified the plaque type. The lesions were classified according to standard criteria (AHA). Differences in tissue type identification and plaque type characterization, if any, were resolved by consensus between the two observers.

5.2.4 | Image analysis

A 1 mm segment of OCT pullback (5 frames) corresponding to each plaque location was selected. The OCT frames were then analyzed with the different methodologies for tissue characterization. The overview of the methods and the tissue types detected are depicted in Table 5.1.

Table 5.1 |

Study	Method	Tissue types detected
Tearney et al. (2003)	Normalized standard deviation in ROI	– Macrophage infiltration in fibrous cap (14)
van Soest et al. (2010)	Optical attenuation	– Macrophage infiltration – Lipid pool – Fibrotic/calcium (18)
Phipps et al. (2015)	Bright spot detection based on depth, catheter position and SNR	– Macrophage – Interfaces between calcium and fibrous, calcium and lipids, and lipid pool and fibrous cap – Cellular fibrous tissue (15)
Athanasίου et al. (2014)	Texture analysis, K-means, automatic thresholding and classification algorithm	– Calcium – Lipid tissue – Fibrous tissue – Mixed tissue (20)

5.3 | Results and discussion

5.3.1 | Lipid tissue

A total of 23 plaques were characterized as having lipid histologically. Image texture and attenuation imaging methods can detect lipid tissue or lipid pool and bright spots algorithm detects the interface of lipid with other tissue components. Both Image texture and attenuation imaging methods had good sensitivity and specificity for lipid tissue. The attenuation imaging method performs well in segments with relatively thin fibrous cap over the lipid. The deeper lipids result in a false negative prediction. Also in segments with large amount of macrophage presence, the high attenuation was mostly due to the macrophages. In these segments Image texture tends to overestimate the lipid content and shows false positives for the internal elastic media layer (IEM) of the vessels. Bright spots method resulted in bright spots at the interface between lipid and fibrous tissue but with a significant underestimation in terms of both the presence and the extent of lipid in the segments. NSD analysis is not aimed at lipid detection but some elevated NSD areas were found in plaque segments that had highly attenuating lipid with no histological presence of macrophages.

5.3.2 | Macrophages

Macrophages were present in 30 segments overall and two of the four compared methods, NSD analysis and bright spots, have macrophages as their major target tissue. The NSD analysis method detected all of the macrophage tissue present superficially and not the deep infiltrated macrophages, as the method requires selecting a ROI in the fibrous cap of the plaque. The method of Bright spots resulted in bright spots in the most of the region of macrophages but significantly less or no spots when the density of infiltration is less. Image texture do not have a classification for macrophages. The superficial macrophage

infiltrations are classified as mixed tissue and the deeper infiltrations as lipid tissue. Macrophages are the most attenuating tissue type and hence attenuation imaging's attenuation coefficient method performs very well in macrophage detection. Only a couple of segments with deeper infiltrations resulted in false negatives.

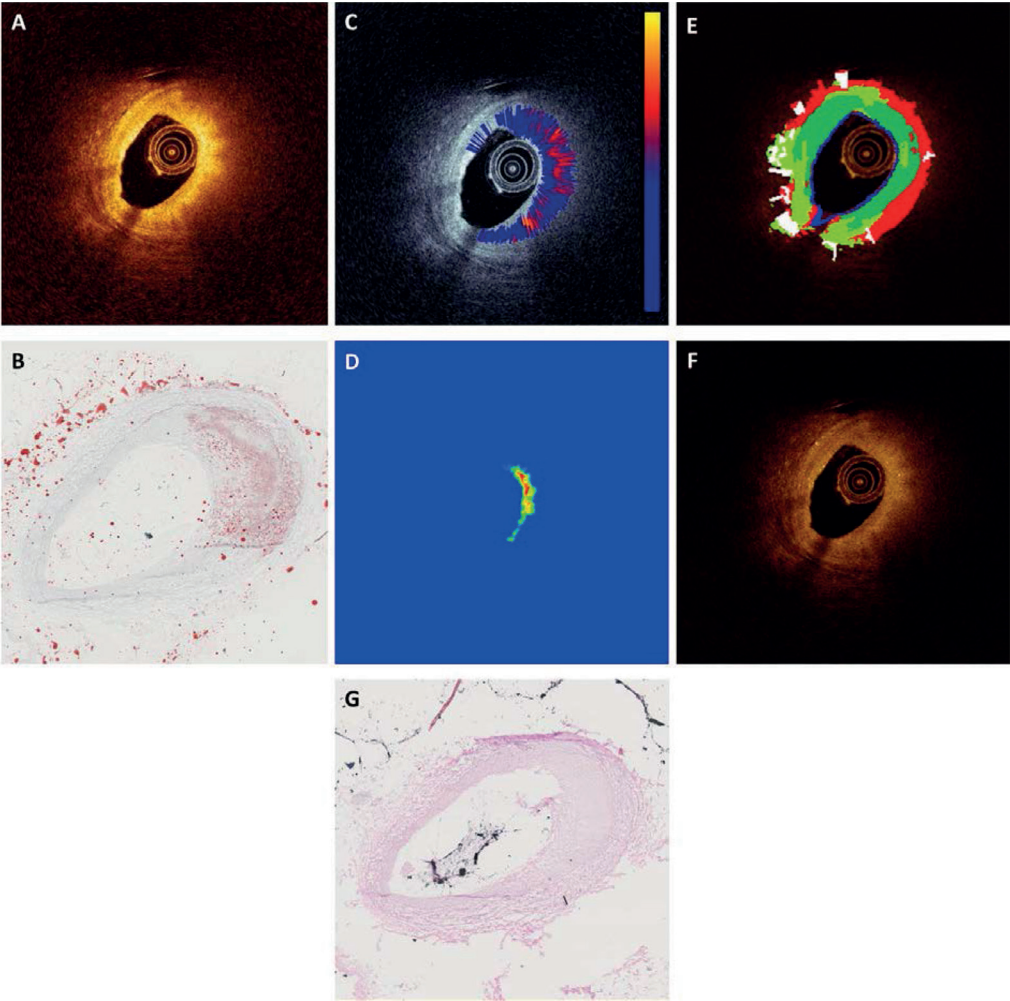


Figure 5.1 | A) Optical coherence tomography image showing a lipid rich plaque B) ORO stain showing the presence of lipid C) Attenuation image of the cross section using the method of attenuation imaging showing high attenuation in the lipid rich region. D) NSD image using the analysis of NSD analysis E) color-coded image produced using Image texture (Red: lipid, White: calcium, green: fibrous tissue and light green: mixed tissue). F) Bright spot algorithm of Bright spots depicting few bright spots at the interface of fibrous and lipid tissue. G) H&E stain of the corresponding cross section.

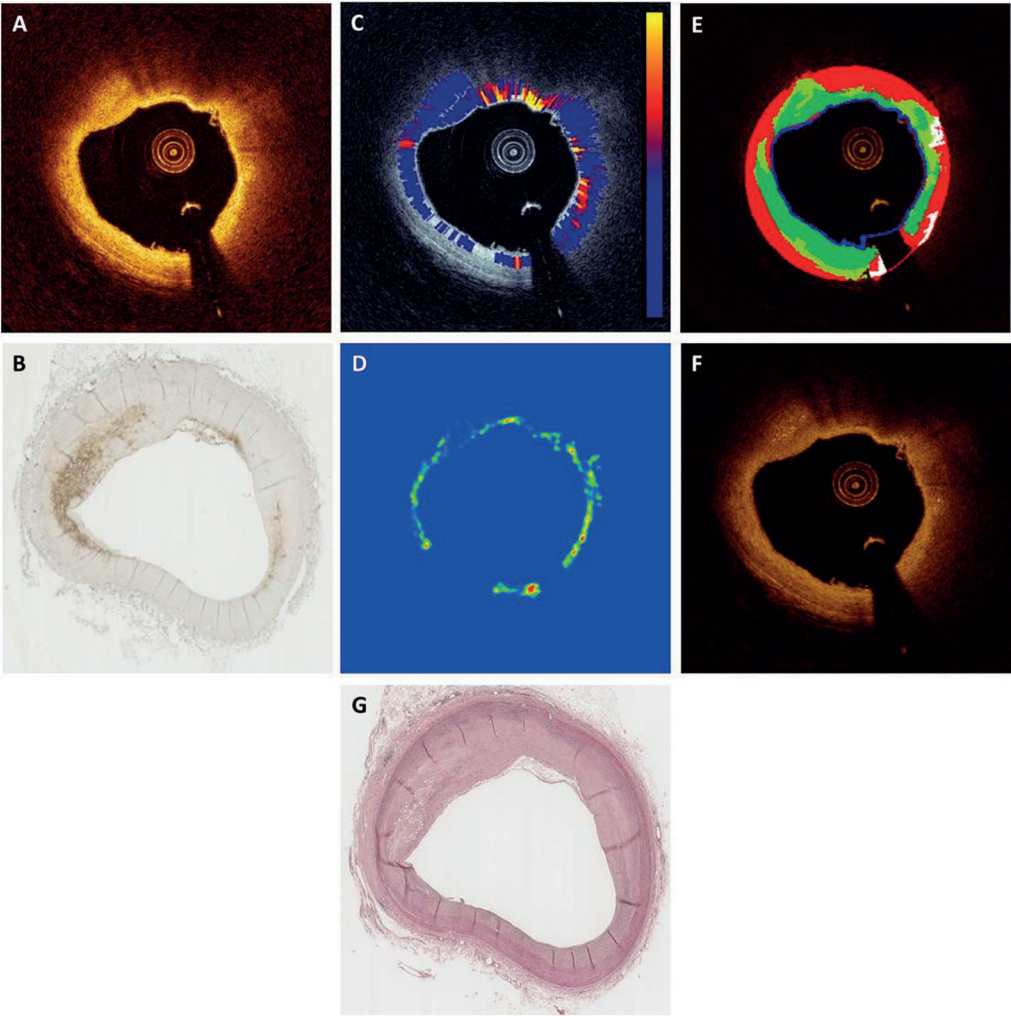


Figure 5.2 | A) Optical coherence tomography image showing a plaque with macrophage infiltration B) CD68 stain showing the presence of macrophages C) Macrophages exhibiting high attenuation in the attenuation image of the cross section using the method of attenuation imaging D) Quantitative macrophage content from the NSD analysis of NSD analysis E) color-coded image produced using Image texture (Red: lipid, White: calcium, green: fibrous tissue and light green: mixed tissue). Macrophages are shown as mixed tissue F) Bright spot algorithm of Bright spots depicting few bright spots corresponding to the macrophage infiltration. G) H&E stain of the corresponding cross section.

5.3.3 | Calcium

Among the methods compared, Image texture’s algorithm is the only method that has classification for calcium. The bright spot method from Bright spots can also detect the presence of calcium indirectly

at the interface with fibrous or lipid tissue. Mixed plaque with regions of calcium and lipid resulted in bright spots but the calcium-fibrous interface almost resulted in no bright spots. Image texture algorithm detected calcium not mixed with lipid better than the calcium in mixed plaque. Only 8 segments in total had calcium.

5.3.4 | Fibrous

Fibrous tissue is relatively homogenous, high backscattering and the least attenuating plaque component. Low attenuation coefficients were depicted by attenuation imaging algorithm for all the segments but for two segments exhibiting high attenuation. In image texture method fibrous tissue is found often present along with mixed tissue even in cases with no histology evidence of mixed plaque. The NSD analysis also showed up some false positives in region with only fibrous tissue.

5.3.5 | Overview

Algorithmic OCT tissue type characterization can provide a valuable metric for automated assessment of the extent and severity of atherosclerotic coronary artery disease. The methods included in this study all have assets that make them valuable contributions to the image analysis toolbox in clinical OCT imaging. With the exception of the image texture classification, all of these algorithms have been developed and tested on histological data sets. This comparative study shows that the NSD, bright spot and attenuation analyses all detect the tissues that they aim to identify, but also have limited specificity, as is evident from the false positives arising for macrophages in NSD and lipid tissue in the attenuation method. The bright spots algorithm does not aim to identify the nature of the detected bright spots but only to investigate the utility of this image feature as a measure for plaque heterogeneity and inflammation. This study is the first to compare texture-based tissue characterization with histology, and it demonstrates a reasonable correspondence, with the caveat that the classification tends to indicate lipid in all areas of signal loss, which leads to an overestimation.

It is interesting to evaluate a hybrid approach, such as the one pioneered by the Leuven group [23], which combines attenuation analysis with classification based on local image statistics. Like the image texture analysis, it has not been evaluated on ex vivo data before. We aim to include this analysis in the near future.

The methods have a few limitations. The methods are either image based or optical parameter retrieval by analyzing the OCT data and hence they also inherit the intrinsic limitations of OCT. OCT has limited tissue-penetration which makes the analyses made on the OCT image beyond certain depth as unreliable. OCT also suffers from artifacts that can resemble the morphology or texture of a plaque tissue type, such as tangential signal drop or catheter proximity. Moreover atherosclerosis is a complex progressive disease and classification of tissues, both on histology and images is necessarily a simplification. Future research should provide more insight into which image features have prognostic value or may be used for intervention guidance.

Some methods require manual selection of ROIs (NSD works on fibrous caps only, attenuation requires the media contour), which can be time consuming and limits automation. This may be addressed by automatic segmentation algorithms [24,25] that are continuously being refined.

5.4 | Conclusions

Each of the methods of OCT tissue characterization compared, has value as an atherosclerotic tissue component detection tool and could play a significant role in the assessment of the stability of the plaque.

References

1. Falk E, Shah PK, Fuster V. Coronary plaque disruption. *Circulation* 1995;92:657-71.
2. Virmani R, Kolodgie FD, Burke AP, Farb A, Schwartz SM. Lessons from sudden coronary death: a comprehensive morphological classification scheme for atherosclerotic lesions. *Arterioscler Thromb Vasc Biol* 2000;20:1262-75.
3. Waxman S, Freilich MI, Suter MJ et al. A case of lipid core plaque progression and rupture at the edge of a coronary stent: elucidating the mechanisms of drug-eluting stent failure. *Circ Cardiovasc Interv* 2010;3:193-6.
4. Goldstein JA, Grines C, Fischell T et al. Coronary embolization following balloon dilation of lipid-core plaques. *JACC Cardiovasc Imaging* 2009;2:1420-4.
5. Regar E, Ligthart J, Bruining N, van Soest G. The diagnostic value of intracoronary optical coherence tomography. *Herz* 2011;36:417-428.
6. Tearney GJ, Regar E, Akasaka T et al. Consensus standards for acquisition, measurement, and reporting of intravascular optical coherence tomography studies: a report from the International Working Group for Intravascular Optical Coherence Tomography Standardization and Validation. *J Am Coll Cardiol* 2012;59:1058-72.
7. Prati F, Di Vito L, Biondi-Zoccai G et al. Angiography alone versus angiography plus optical coherence tomography to guide decision-making during percutaneous coronary intervention: the Centro per la Lotta contro l'Infarto-Optimisation of Percutaneous Coronary Intervention (CLI-OPCI) study. *EuroIntervention* 2012;8:823-9.
8. Garcia-Garcia HM, Costa MA, Serruys PW. Imaging of coronary atherosclerosis: intravascular ultrasound. *Eur Heart J* 2010;31:2456-69.
9. Prati F, Guagliumi G, Mintz GS et al. Expert review document part 2: methodology, terminology and clinical applications of optical coherence tomography for the assessment of interventional procedures. *Eur Heart J* 2012;33:2513-20.
10. Guagliumi G, Musumeci G, Sirbu V et al. Optical coherence tomography assessment of in vivo vascular response after implantation of overlapping bare-metal and drug-eluting stents. *JACC Cardiovasc Interv* 2010;3:531-9.
11. Guagliumi G, Costa MA, Sirbu V et al. Strut coverage and late malapposition with paclitaxel-eluting stents compared with bare metal stents in acute myocardial infarction: optical coherence tomography substudy of the Harmonizing Outcomes with Revascularization and Stents in Acute Myocardial Infarction (HORIZONS-AMI) Trial. *Circulation* 2011;123:274-81.
12. Yabushita H, Bouma BE, Houser SL et al. Characterization of human atherosclerosis by optical coherence tomography. *Circulation* 2002;106:1640-5.
13. Kume T, Akasaka T, Kawamoto T et al. Assessment of coronary arterial plaque by optical coherence tomography. *Am J Cardiol* 2006;97:1172-5.
14. Tearney GJ, Yabushita H, Houser SL et al. Quantification of macrophage content in atherosclerotic plaques by optical coherence tomography. *Circulation* 2003;107:113-9.
15. Phipps JE, Vela D, Hoyt T et al. Macrophages and intravascular OCT bright spots: a quantitative study. *JACC Cardiovasc Imaging* 2015;8:63-72.
16. Gnanadesigan M, van Soest G, White S et al. Effect of temperature and fixation on the optical properties of atherosclerotic tissue: a validation study of an ex-vivo whole heart cadaveric model. *Biomed Opt Express* 2014;5:1038-49.
17. Regar E, Gnanadesigan M, Van der Steen AF, van Soest G. Quantitative optical coherence tomography tissue-type imaging for lipid-core plaque detection. *JACC Cardiovasc Interv* 2013;6:891-2.
18. van Soest G, Goderie T, Regar E et al. Atherosclerotic tissue characterization in vivo by optical coherence tomography attenuation imaging. *J Biomed Opt* 2010;15:011105.
19. van der Meer FJ, Faber DJ, Baraznji Sassoon DM, Aalders MC, Pasterkamp G, van Leeuwen TG. Localized measurement of optical attenuation coefficients of atherosclerotic plaque constituents by quantitative optical coherence tomography. *IEEE Trans Med Imaging* 2005;24:1369-76.
20. Athanasiou LS, Bourantas CV, Rigas G et al. Methodology for fully automated segmentation and plaque characterization in intracoronary optical coherence tomography images. *J Biomed Opt* 2014;19:026009.

21. Wu M, Jansen K, van der Steen AF, van Soest G. Specific imaging of atherosclerotic plaque lipids with two-wavelength intravascular photoacoustics. *Biomed Opt Express* 2015;6:3276-86.
22. Johnson TW, White S, Gnanadesigan M et al. An Ex-Vivo "Whole Human Heart Model" for the Development of Intravascular Imaging. *Heart* 2012;98:15-A16.
23. Ughi GJ, Adriaenssens T, Sinnaeve P, Desmet W, D'hooge J. Automated tissue characterization of in vivo atherosclerotic plaques by intravascular optical coherence tomography images. *Biomed Opt Express* 2013;4:1014-1030.
24. Wang Z, Chamie D, Bezerra HG et al. Volumetric quantification of fibrous caps using intravascular optical coherence tomography. *Biomed Opt Express* 2012;3:1413-1426.
25. Zahnd G, Karanasos A, van Soest G et al. Quantification of fibrous cap thickness in intracoronary optical coherence tomography with a contour segmentation method based on dynamic programming. *Int J Comput Assist Radiol Surg* 2015.

Chapter 6

OCT Assessment of the Long-Term Vascular Healing Response 5 Years After Everolimus-Eluting Bioresorbable Vascular Scaffold

Antonios Karanasos, Cihan Simsek, Muthukaruppan Gnanadesigan, Nienke S van Ditzhuijzen, Raphael Freire, Jouke Dijkstra, Shengxian Tu, Nicolas Van Mieghem, Gijs van Soest, Peter de Jaegere, Patrick W Serruys, Felix Zijlstra, Robert-Jan van Geuns, Evelyn Regar

J Am Coll Cardiol 64, 2343-2356 (2014)

Abstract

Background: Although recent observations suggest a favorable healing process of the everolimus-eluting bioresorbable vascular scaffold (BVS), little is known regarding the long-term healing response.

Objective: We assessed the in vivo vascular healing response 5 years following elective first-in-man BVS implantation by optical coherence tomography (OCT).

Methods: Out of 14 living patients enrolled in the Thoraxcenter Rotterdam cohort of ABSORB A study, eight patients underwent invasive follow-up including OCT, 5 years post implantation. Advanced OCT image analysis included luminal morphometry, assessment of the adluminal signal-rich layer separating the lumen from other plaque components, visual and quantitative tissue characterization, and assessment of side-branch ostia jailed at baseline.

Results: In all patients, BVS struts were integrated in the vessel and not discernible. Both, minimum and mean luminal area increased from 2 to 5 years, while lumen eccentricity decreased over time. In most patients plaques were covered by a signal-rich, low-attenuating layer. The minimum cap thickness over necrotic core was $155 \pm 90 \mu\text{m}$. One patient showed different tissue response with plaque progression and discontinuity of this layer. Side-branch ostia were preserved with thinning of tissue bridges that had developed in the place of side-branch struts creating a ‘neo-carina’.

Conclusions: At long-term BVS follow-up, a favorable tissue response is observed, with late luminal enlargement, side-branch patency, and development of a signal-rich, low-attenuating tissue layer covering thrombogenic plaque components. The small scale of our study and the observation of a different tissue response in one patient warrant the judicious interpretation of our results and further confirmation in larger studies.

Abbreviations

BVS: bioresorbable vascular scaffold

ICC: intraclass correlation coefficient

IEL: internal elastic lamina

IQR: interquartile range

IVUS: intravascular ultrasound

LAD: left anterior descending artery

LCx: left circumflex artery

OCT: optical coherence tomography

OM: obtuse marginal branch

SB: side-branch

6.1 | Introduction

Metallic stents for percutaneous revascularization have been associated with late complications, such as neoatherosclerosis, late restenosis and thrombosis [1]. Bioresorbable vascular scaffolds (BVS) could help overcome such pitfalls. In the ABSORB A study, the first-generation everolimus-eluting bioresorbable vascular scaffold (Absorb BVS 1.0; Abbott Vascular, Santa Clara, CA, USA) was associated with a good long-term clinical outcome after 2 and 5 years [2,3]. Plaque regression from 2 to 5 years and recovery of vasomotion in the scaffolded segment were documented in a patient subset [4]. Moreover, recent clinical observations of a signal-rich layer separating potentially thrombogenic plaque components from the lumen [5,6], suggest a favorable long-term healing response with potential plaque sealing.

We aimed to provide a comprehensive optical coherence tomography (OCT) analysis of the vascular healing response in the longest follow-up available to date, namely after 5 years, in the first series of patients who received everolimus-eluting BVS.

6.2 | Methods

6.2.1 | Patient population

The study population [4] and index procedure [2] have been described (see supplementary material). Briefly, all living patients of the Thoraxcenter Rotterdam cohort of ABSORB A study (n=14) were asked to participate. Eight of them consented and were included. The protocol was approved by the institutional ethics committee and conforms to the declaration of Helsinki.

6.2.2 | OCT image acquisition

All 8 subjects underwent frequency-domain OCT at the 5-year invasive follow-up [7]. Six patients at baseline, 7 patients at 6-month follow-up, and 7 patients at 2-year follow-up had undergone occlusive time domain OCT as per ABSORB A study protocol, with serial OCT imaging at all intervals available for 5 patients. For details see supplementary material.

6.2.3 | Definitions

OCT analysis of bioresorbable scaffolds has essential differences from metal stents (Figure 6.1). In metal stents, struts are preserved and neointimal area is clearly defined as the area between stent and lumen contour. In BVS, when scaffold struts are still discernible, the neointimal area can be assessed similarly to metal stents. However, at long-term follow-up, scaffold struts are no longer visible and the area corresponding to struts and neointima has similar optical properties as the underlying fibrous layer [5,8]. Consequently, it is impossible to distinguish between strut area, neointimal area and underlying plaque.

Therefore, the vascular structure observed at the scaffolded segment as a product of the consolidation of underlying plaque, biodegraded struts and neointima resembles a native atherosclerotic plaque and was defined as **neo-plaque** (Figure 6.1).

Since the scaffold area, and thus neointimal area cannot be distinguished from the underlying plaque by OCT, neointimal thickness cannot be directly assessed. Hence, we aimed to provide an indirect assessment focusing on the signal-rich layer observed, consisting of the neointimal layer, resorbed struts and pre-existing fibrous tissue. Therefore, we analyzed this signal-rich layer for providing a measure of the separation of the lumen from underlying plaque components [5,6]. The signal-rich layer encompassed the area between lumen border and internal elastic lamina (IEL). In situations where signal-poor regions (calcifications, necrotic core, deeply located fibrous plaque) obscured IEL delineation, the signal-rich layer was delineated between lumen border and the boundary of signal-rich and signal-poor regions (Figures 6.1-6.2).

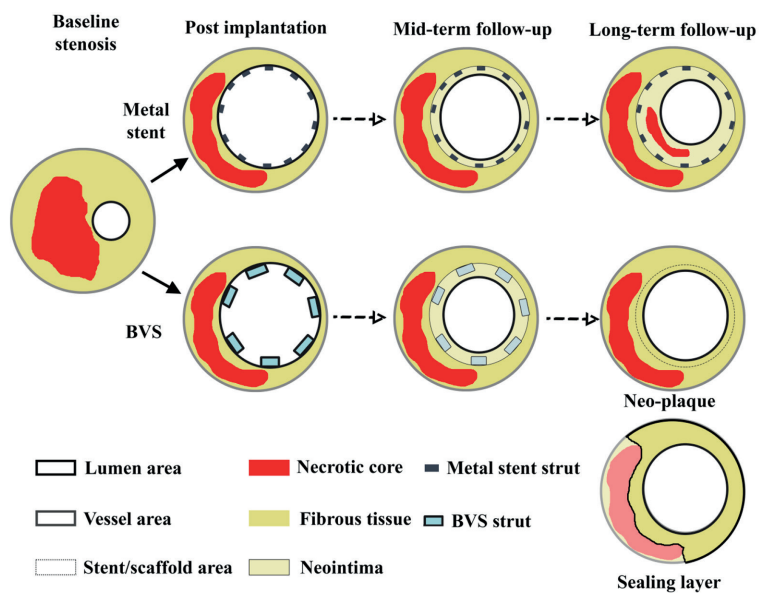


Figure 6.1 | Long-term vascular healing response in metal stents and bioresorbable scaffolds. After metal stent implantation, struts are preserved and the neointimal area is clearly delineated between stent and lumen contour even at long-term, with possible development of neoatherosclerosis within the neointima. Conversely, in long-term follow-up of bioresorbable scaffolds, after bioresorption neointimal boundaries are unclear (dotted line), and the intima resembles a native plaque, defined as ‘neo-plaque’. The ‘sealing layer’ is defined as the layer separating the underlying plaque components from the lumen.

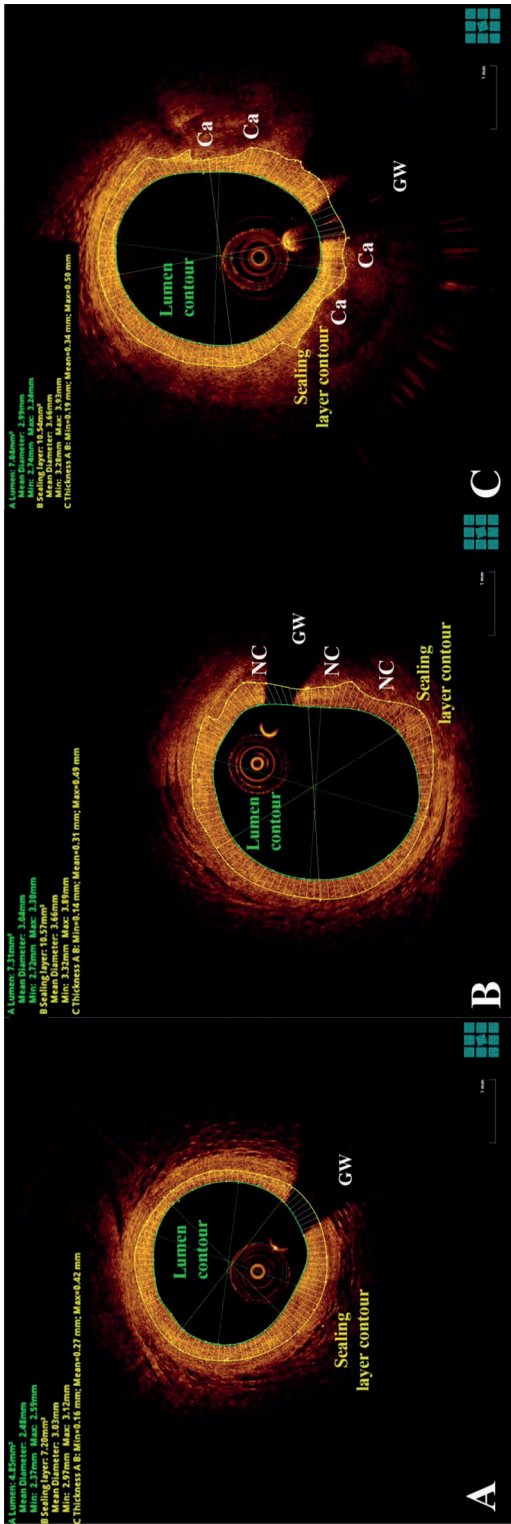


Figure 6.2 | Quantification of ‘sealing layer’ thickness in different plaque types. A) In the absence of attenuating intimal regions, the contour is traced at the IEL. B) In plaques with necrotic core, the abluminal contour is traced at the attenuating region boundary. C) In plaques with calcifications, the ‘sealing layer’ is segmented at the calcification edge. *Abbreviations:* GW, guidewire; NC, necrotic core; Ca, calcium.

6.2.4 | OCT image analysis

The region of interest was defined by the platinum scaffold markers. Quantitative and qualitative 5-year OCT image analysis was performed per frame. Analysis included the assessment of discernible struts, lumen morphometry, signal-rich layer thickness measurement, neo-plaque characterization, attenuation analysis, and ostial side-branch assessment. Metal stents implanted in the same vessels were also analyzed [1].

6.2.5 | Luminal measurements and variability analysis

For details see supplementary material. Measurements included mean and minimum lumen area and eccentricity, calculated as the ratio [(maximum lumen diameter – minimum lumen diameter)/maximum lumen diameter] [7]. Lumen measurements were assessed for intra-observer, inter-observer and intra-study variability.

6.2.6 | Quantification of signal-rich layer thickness

The signal-rich layer was quantified following segmentation of its luminal and abluminal contour, by measurement of minimum, mean and maximum thickness and symmetry (ratio of minimal-to-maximal thickness; Figure 6.2). Signal-rich layer measurements were assessed for variability.

6.2.7 | ‘Neo-plaque’ characterization

‘Neo-plaque’ morphology was assessed per frame at five years, according to native atherosclerosis definitions [7], and the arc of calcifications, necrotic core and mixed plaque was measured using QCU-CMS (LKEB, Leiden University, Netherlands; research version of QIvus, Medis medical imaging systems bv, Leiden, Netherlands). Fibrous cap contours were traced over necrotic core and minimum cap thickness was measured. Mean and minimum cap thickness was calculated per patient. Spread-out maps representing ‘neo-plaque’ morphology and cap thickness throughout the scaffolded segment were generated (Figure 6.3), and color-coded according to plaque type. The presence of sharply-delineated signal-poor voids, corresponding to intimal microchannels [7], was recorded.

In ‘neo-plaques’ with necrotic core, OCT images were compared with previous follow-ups, in order to investigate for any evidence of de novo accumulation of necrotic core of adluminal origin, possibly corresponding to neoatherosclerosis.

6.2.8 | Attenuation analysis

We used attenuation analysis for quantitative tissue characterization of the signal-rich layer and the ‘neo-plaque’ (Figure 6.4). In ex-vivo validation experiments, highly-attenuating regions (attenuation coefficient $\mu_t \geq 8 \text{ mm}^{-1}$) have been associated with necrotic core or macrophages. On the contrary, $\mu_t < 6 \text{ mm}^{-1}$ were associated with healthy vessel components, intimal thickening or calcified plaque [9,10]. Attenuation was quantified circumferentially at different depths from the lumen surface by custom-made software [11]. Results were plotted in spread-out maps demonstrating 1) maximum attenuation coefficient per A-line throughout the pullback, and 2) attenuation coefficient values in different depths from the vessel surface.

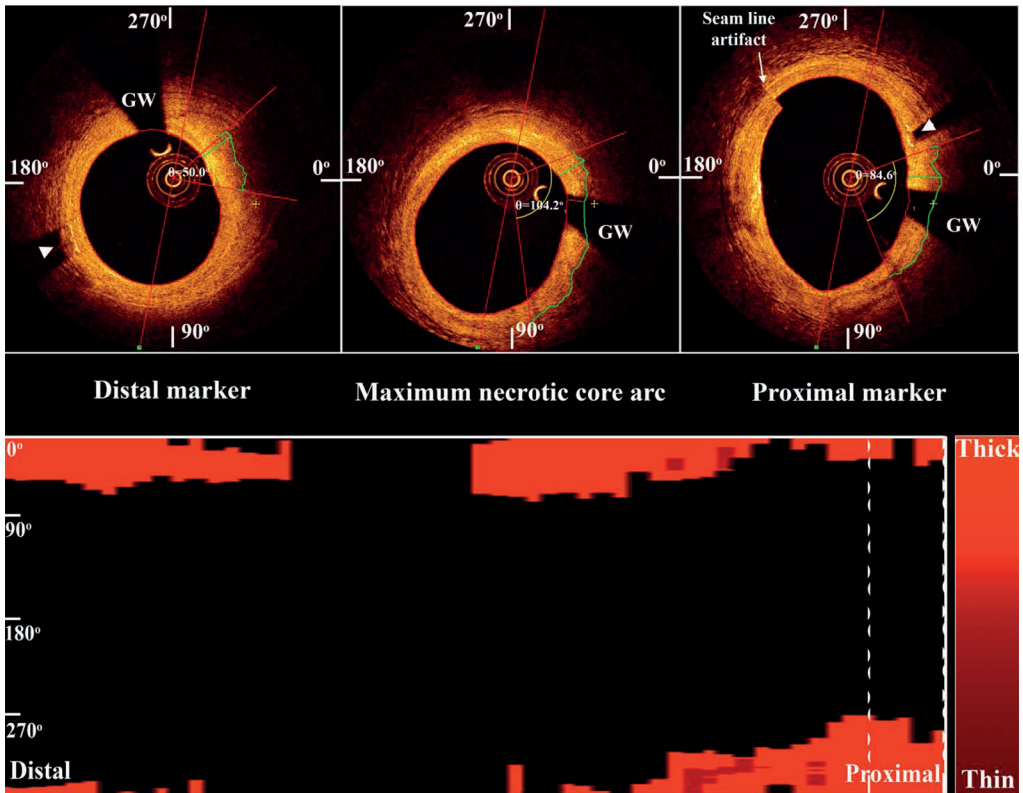
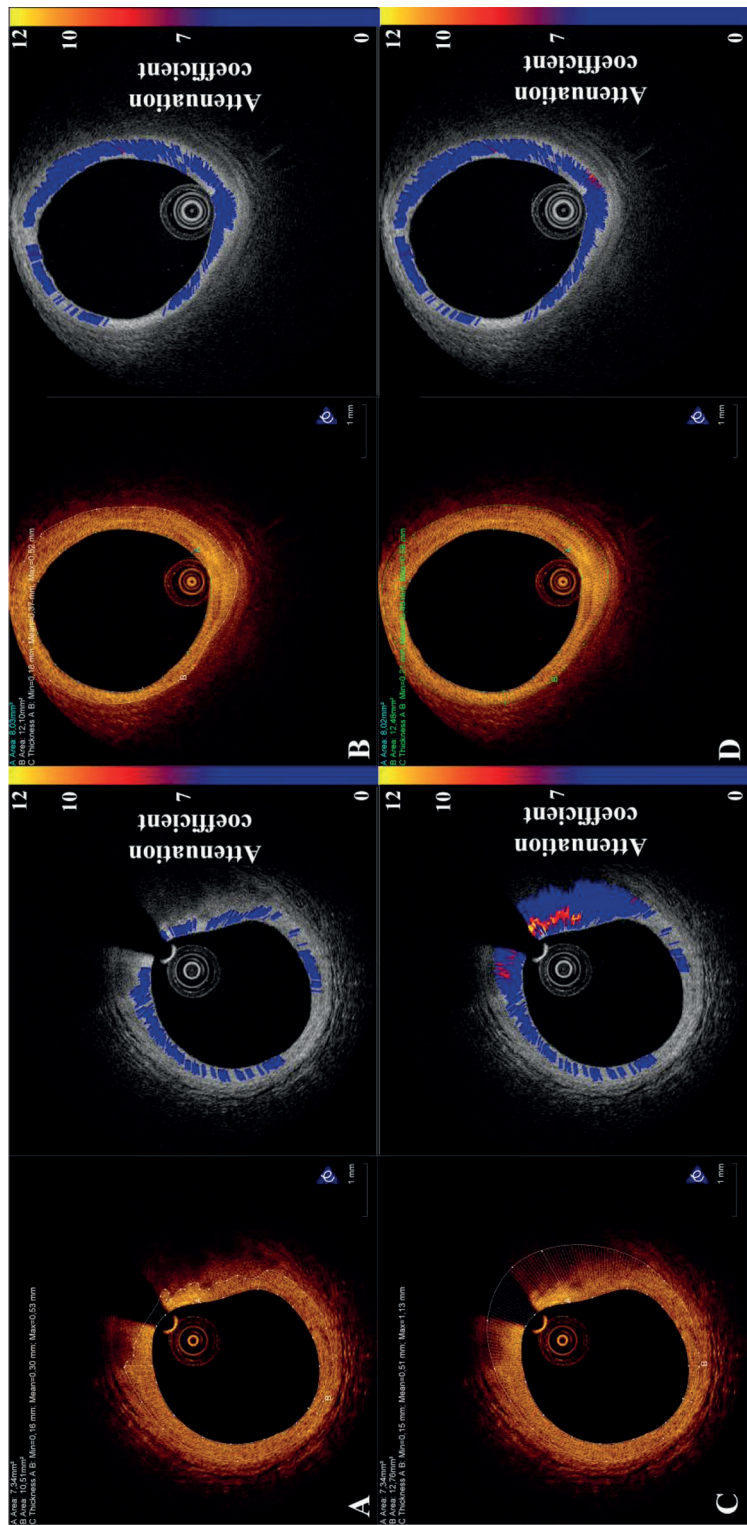


Figure 6.3 | Plaque characterization and cap tracing. In frames with necrotic core, calcifications, or mixed plaque within the scaffolded segment, the overlying fibrous cap is segmented and minimum thicknesses are recorded. A spread-out map is generated, showing the component distribution within the ‘neo-plaque’, with lighter colours corresponding to thicker caps. GW, guidewire; arrowhead, scaffold marker

6.2.9 | Side-branch assessment

In order to assess anatomical side-branch jailing over time, three-dimensional images of side-branch ostia were obtained by volume-rendering software (Intage Realia, KGT, Japan) [1]. No struts were identifiable in OCT, but neointimal bridges had developed in their place. Neointimal bridges were classified based on their relative location to the ostium as proximal, distal, proximal and distal, or crossing (Figure 6.5). Mean and minimal thickness was measured in matched frames at 2-year and 5-year follow-up using QCU-CMS (Supplementary Figure 6.1).

Side-branch ostium area was assessed using dedicated software (QAngioOCT 1.0, Medis Specials by, Leiden, Netherlands). Following three-dimensional reconstruction, a cut-plane perpendicular to the side-branch centerline was selected and side-branch ostium planimetry was performed (Figure 6.6) [13].



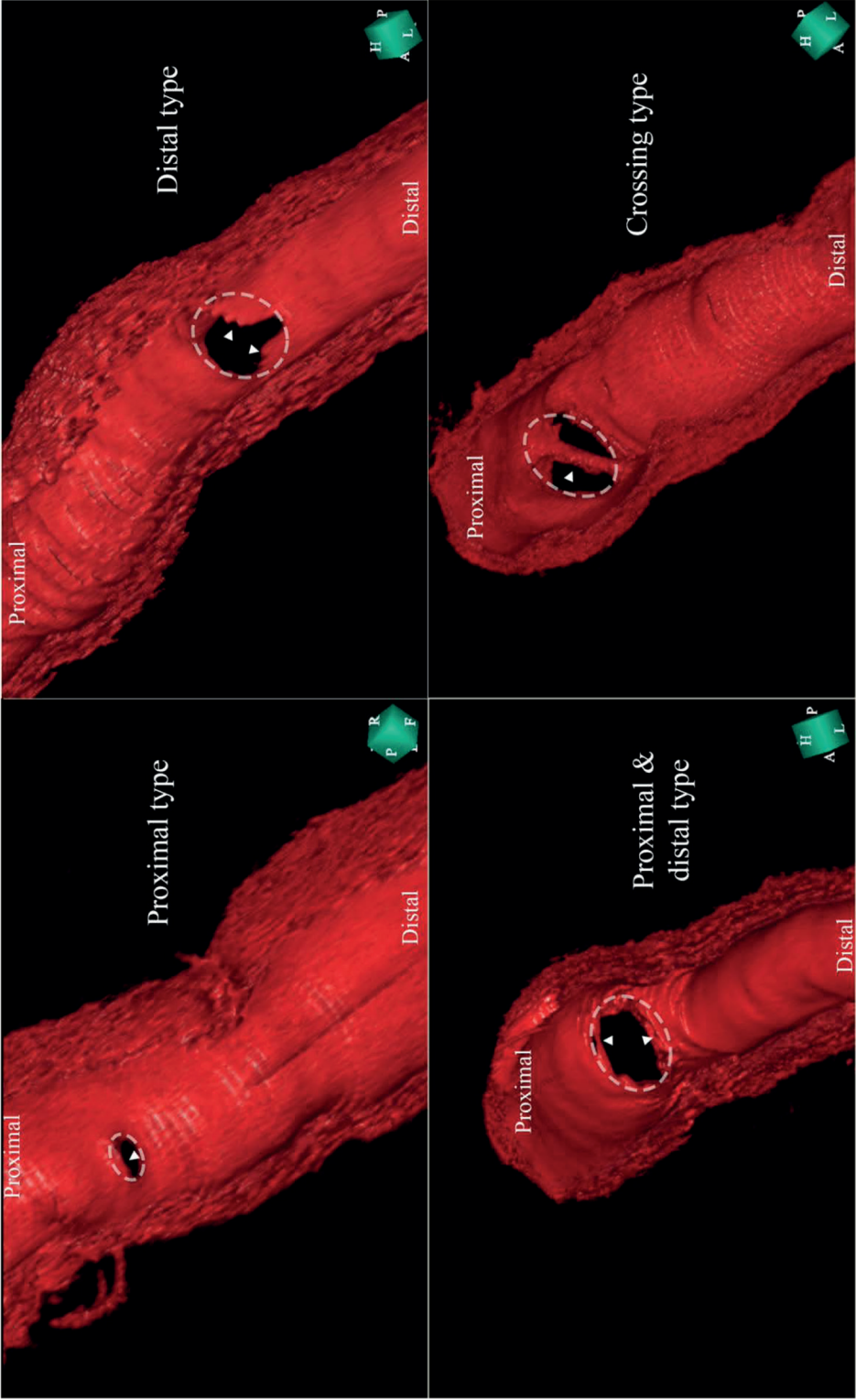


Figure 6.5 | Different types of tissue bridges overlying side-branches. The classification is based on the relative location of the tissue bridge with the side-branch ostium. Four different types can be identified: proximal, distal, proximal and distal, or crossing. Dotted lines indicate side-branch ostia and arrowheads tissue bridges.

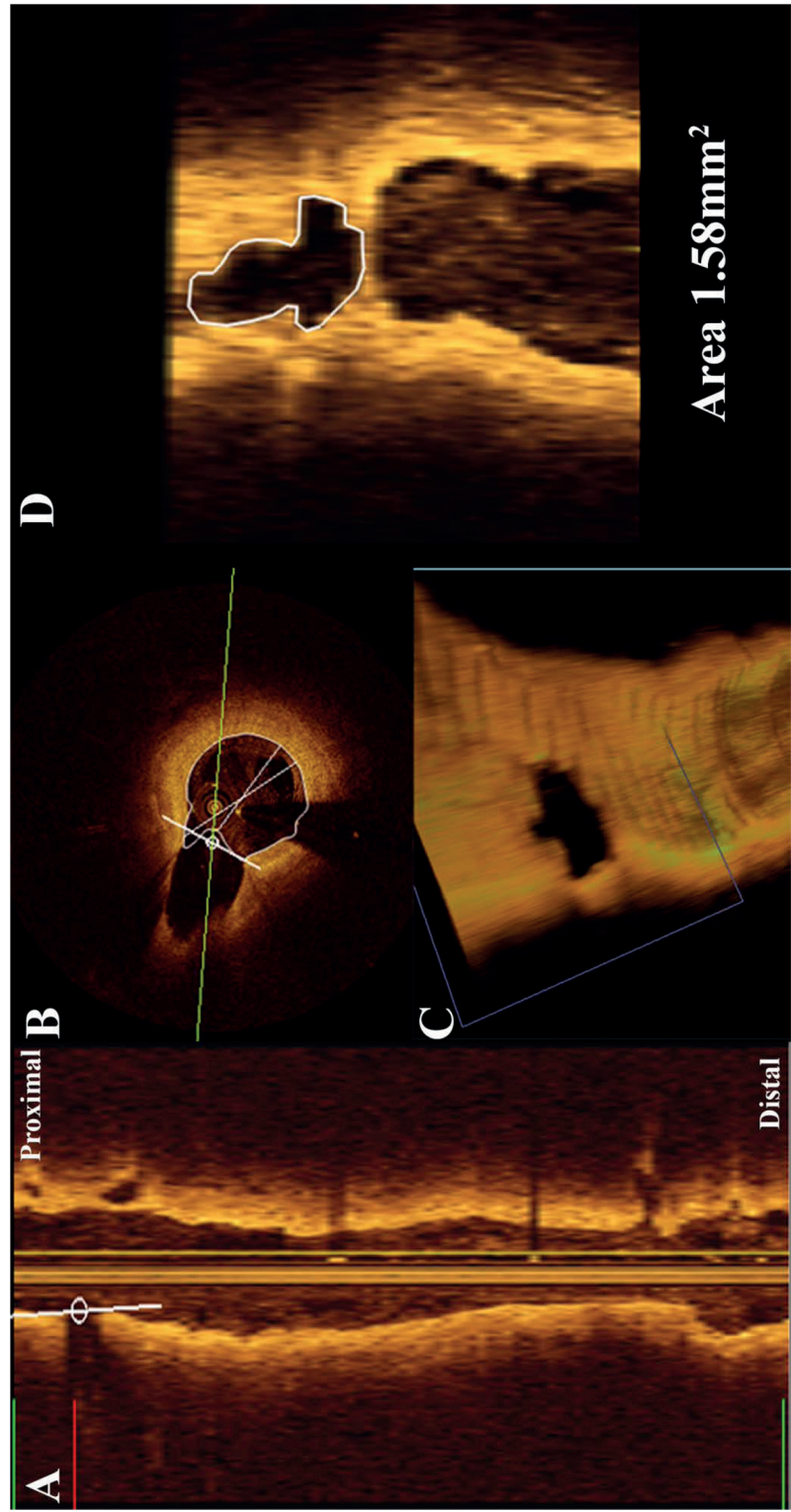


Figure 6.6 | Side-branch ostium area measurement by cut-plane analysis. Following three-dimensional rendering, side-branch ostium area can be measured in a cut-plane perpendicular to the side-branch ostium using QAngioOCT. A) L-mode display. B) Cross-sectional image. C) Three-dimensional rendering. D) Derived cut-plane.

6.2.10 | Statistical analysis

Continuous variables are presented as mean \pm SD, or median (interquartile range; IQR), and nominal variables as n, (%). Significance level was set at $p < 0.05$. Luminal measurements were compared by Wilcoxon's signed rank test. All other paired comparisons were performed by paired t-test. No corrections were made for multiple comparisons. Variability was assessed using intraclass correlation coefficients (ICCs) for absolute agreement and Bland-Altman statistics. Statistical analysis was performed with SPSS 20.0 (IBM, Armonk, NY, USA).

6.3 | Results

6.3.1 | Lumen and strut measurements

No binary restenosis was witnessed in the 5-year angiograms. In all patients, scaffold struts were no longer discernible as a result of complete bioresorption, and lumen area increased significantly from 2 to 5 years (Figure 6.7). Lumen eccentricity declined over time (baseline: 0.24 ± 0.13 ; 6-month: 0.29 ± 0.12 ; 2-year: 0.21 ± 0.08 ; 5-year: 0.15 ± 0.02 ; $p < 0.05$ for all comparisons versus previous studies).

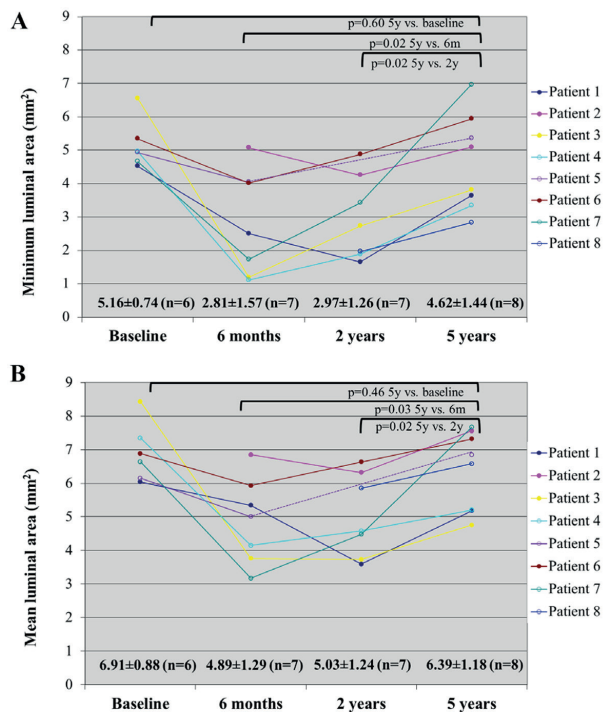


Figure 6.7 | Serial luminal measurements.

Despite an initial decrease in lumen dimensions from baseline to 6 months, (A) minimal and (B) mean lumen area are increased at 5 years compared to previous follow-ups and not significantly different than baseline.

The total strut count in five patients with serial observations was reduced from 278 at baseline, to 248 at 6 months, to 174 at 2 years, and no visible struts at 5 years. Two cases with incomplete scaffold apposition at baseline or 6 months demonstrated complete resolution of incomplete scaffold apposition at 2 years, with complete strut bioresorption at 5 years.

6.3.2 | Quantification of signal-rich layer.

Median values [IQR] for mean, minimum, and maximum signal-rich layer thickness, and symmetry were 330 μm [290 μm –378 μm], 150 μm [120 μm –190 μm], 570 μm [500 μm –640 μm], and 0.26 [0.20–0.33], correspondingly. Supplementary Figure 6.2 demonstrates frequency distributions of these thickness measurements.

6.3.3 | ‘Neo-plaque’ characterization

Spread-out ‘neo-plaque’ maps are presented in Figure 6.8. The mean value of minimum cap thickness was $310 \pm 113 \mu\text{m}$, while the minimum value was $155 \pm 90 \mu\text{m}$. Mean and maximum values were $92 \pm 49^\circ$ and $156 \pm 72^\circ$ for necrotic core arc, 80° and 104° for calcification arc, $104 \pm 145^\circ$ and $146 \pm 80^\circ$ for mixed plaque arc.

Microchannels were identified in 7/8 patients and in 66/468 frames (14.1%). As seen in the ‘neo-plaque’ maps, necrotic core or mixed plaque >1 quadrant was observed in 7 patients. Comparison with previous follow-ups did not reveal evidence of de novo necrotic core accumulation of adluminal origin.

Two patients had a focally irregular lumen contour: Patient 8 had a short intimal dissection, not present at earlier investigations, at the overlap between BVS and a metallic stent implanted at baseline. We assume that this minor, angiographically not visible dissection is most likely iatrogenic, induced by the guidewire. In Patient 4, a thin cap fibroatheroma was observed at the distal scaffold segment with cap disruption and small thrombus (Figure 6.9). This patient had undergone implantation of a 3.0x12 mm BVS, after 2.5x8 mm balloon predilation, further post-dilated with a 3.0x8 mm balloon. Post-hoc revision of previous OCT examinations revealed possible scaffold discontinuity near the distal edge at 4 months, with the scaffold being dislocated opposite to the rupture site. During 2218-day follow-up, the patient underwent uneventful revascularization of a flow-limiting lesion (fractional flow reserve: 0.79) 5mm distal of the BVS with a 3.0x2.5x19 mm Tryton bifurcation stent (Tryton Medical, Newton, MA) also covering the scaffolded segment.

6.3.4. | Attenuation analysis

Mean attenuation per patient within the signal-rich layer was $1.77 \pm 0.32 \text{ mm}^{-1}$ and the median was $1.28 \pm 0.25 \text{ mm}^{-1}$ (Supplementary Figure 6.3). This value was higher within the entire ‘neo-plaque’ (mean per patient: $2.87 \pm 0.54 \text{ mm}^{-1}$, median per patient: $2.33 \pm 0.49 \text{ mm}^{-1}$, $p < 0.001$; Supplementary Figure 6.4). Spread-out attenuation maps at different depths from the luminal surface (100 μm , 200 μm , and

400 μm) are displayed in Figure 6.10. The surface layers (first 200 μm) had low attenuation, overlying high-attenuation areas located deeper in the plaque.

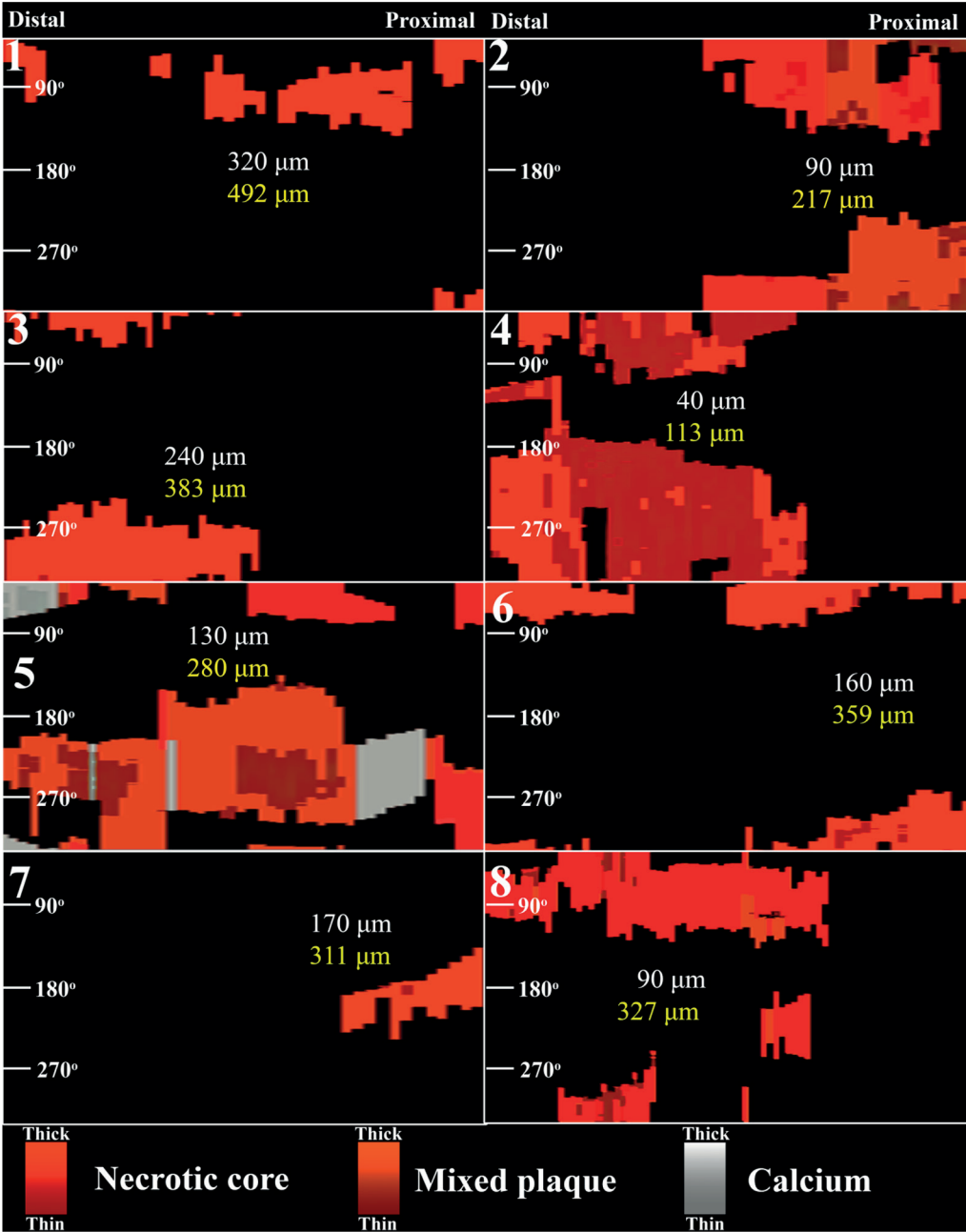


Figure 6.8 | Neo-plaque morphology. Spread-out maps from all patients demonstrating ‘neo-plaque’ composition. Red represents necrotic core, orange mixed plaque, and white calcification. Lighter colours indicate a thicker fibrous cap (>250 μm). The minimum and mean values of minimum cap thickness per patient are presented in white and yellow, respectively.

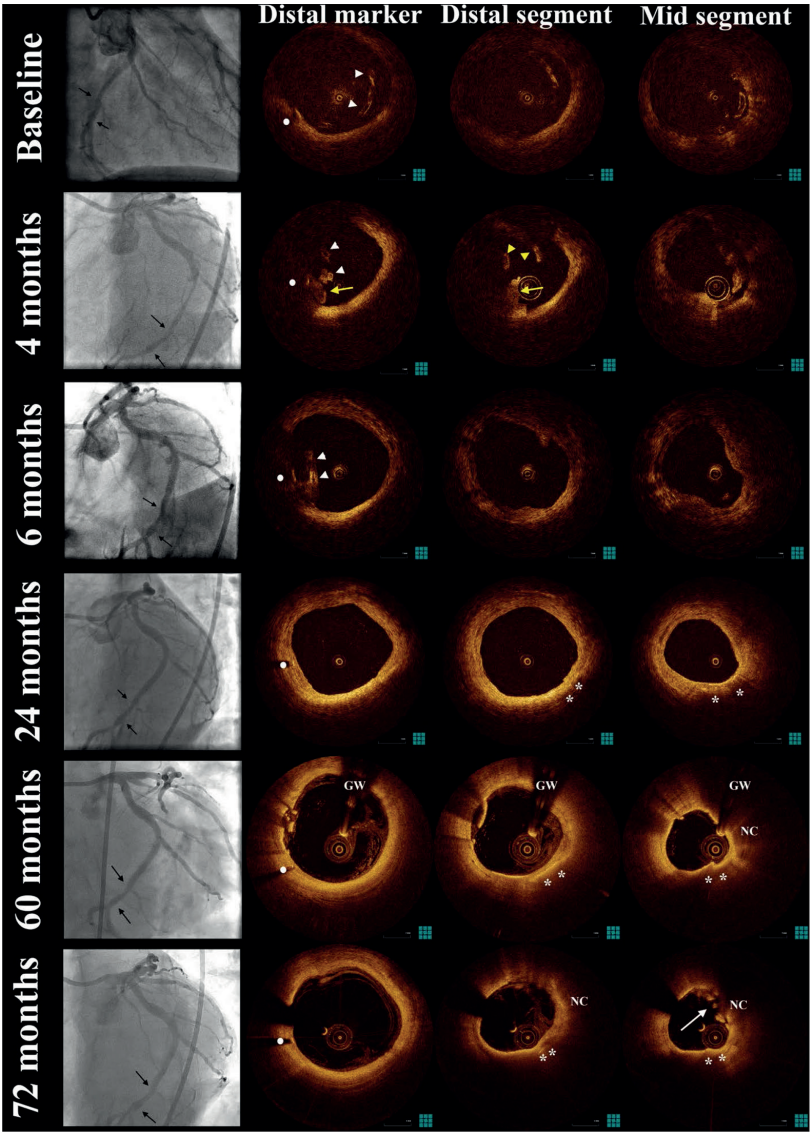


Figure 6.9 | Vascular response in Patient 4. At baseline, there is malapposition (white arrowheads) at the distal scaffold segment. At a follow-up examination at 106 days performed during non-target lesion revascularization, scaffold collapse (white arrowheads) at the site of the distal marker (white bullet), overhanging struts (yellow arrowheads), and thrombus (yellow arrow) were observed suggestive of late scaffold discontinuity. At 6 months, a tissue bridge was formed (white arrowheads) at the site of the collapsed scaffold, and integrated into the vascular wall by 24 months. There is also macrophage accumulation (white asterisks) at the opposite side at 24 months. At a subsequent 60-month follow-up, lesion progression with macrophages and necrotic core was evident, as well as intimal disruption. At the 72-month study follow-up, there is further luminal narrowing and plaque rupture with thrombus (white arrow). *Abbreviations:* GW, guidewire; NC, necrotic core.

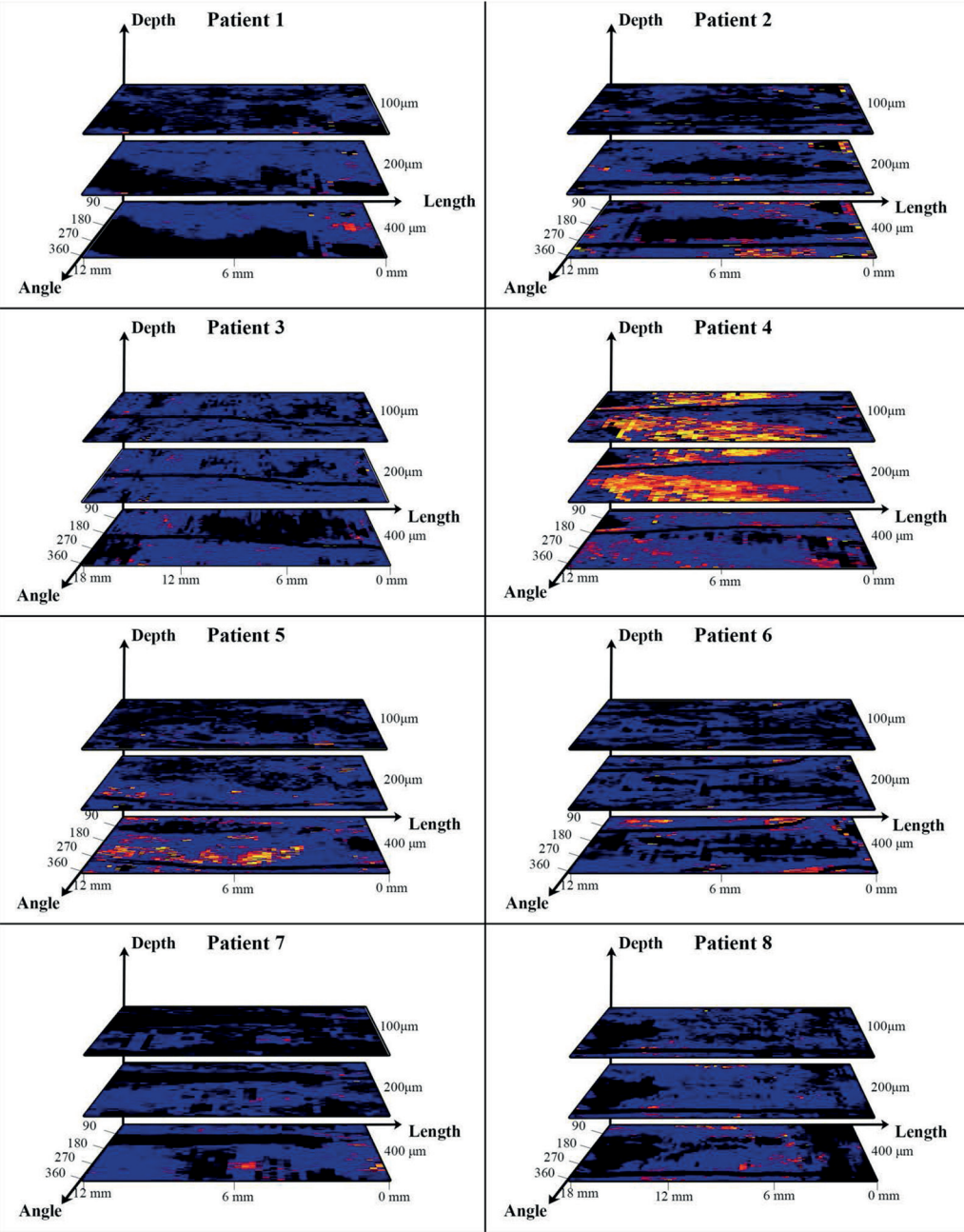


Figure 6.10 | Attenuation spread-out maps in different depths from the vessel surface. Spread-out maps demonstrating the attenuation coefficient, in certain depths from the vessel surface (100 μm , 200 μm , and 400 μm) per patient. In the majority of patients, there is a low-attenuating layer of 200 μm , separating the underlying plaque (starting at $\sim 400 \mu\text{m}$) from the lumen. In Patient 4, this layer is absent and the plaque is close to the lumen.

6.3.5 | Side-branch assessment

All side-branches were patent with TIMI III flow. Overall, 14 side-branches were associated with incompletely apposed struts at previous examinations. Neointimal bridges at 5 years were identified in 13 side-branches, whereas in one no bridge was visible (Table 6.1).

Minimal and mean thickness of neointimal bridges overlying side-branches were respectively reduced from 241±92 µm and 341±106µm at 2 years to 161±107 µm and 227±119 at 5 years (p<0.001; Supplementary Figure 6.5).

Table 6.1 | Side-branch analysis.

	Bifurcation type	SB ostium area(mm ²)	Jailing pattern
Patient 1-SB 1	OM-LCx	4.81	Proximal and distal
Patient 2-SB 1	LAD-septal	6.22	Crossing
Patient 2-SB 2	LAD-diagonal	1.14	Distal
Patient 2-SB 3	LAD-septal	1.89	Proximal
Patient 3-SB 1	LAD-diagonal	1.58	Distal
Patient 3-SB 2	LAD-septal	1.42	N/A*
Patient 4-SB 1	LCx-OM	1.11	Proximal and distal
Patient 5-SB 1	LAD-septal	1.93	Crossing
Patient 5-SB 2	LAD-diagonal	0.46	Distal
Patient 6-SB 1	LCx-OM	1.37	Crossing
Patient 6-SB 2	OM-LCx	2.23	Distal
Patient 8-SB 1	LCx-OM	N/A†	Proximal
Patient 8-SB 2	LCx-posterolateral	0.3	Proximal
Patient 8-SB 3	LCx-OM	0.78	Proximal

*The bridge was not present at 5 years - distal location at previous studies. †Exact area not measurable. *Abbreviations:* SB, side-branch; OM, obtuse marginal branch; LCx, left circumflex artery; LAD, left anterior descending artery.

6.3.6 | Metal DES analysis

Metal DES analysis is presented in Supplementary Table 6.1 and Figure 6.11. In Patient 1, there was a focal distal edge stenosis of a distally overlapping 3.0x13 mm SES (luminal area:1.74 mm²) left untreated. In all metal stents, coverage was >95%, without malapposed struts, while neoatherosclerosis was identified in all.

6.3.7 | Variability analysis

Inter- and intra-observer variability for both frame- and patient-level analysis was low (inter-observer: difference 0.23 ± 0.29 mm, ICC 0.98; inter-observer [core-lab]: difference 0.13 ± 0.32 mm, ICC 0.98; intra-observer: difference 0.17 ± 0.19 mm, ICC 0.99) (Supplementary Table 6.1; Supplementary Figure 6.6). As seen in the Bland-Altman plots, there were few measurements with significant differences, all of which in the polygon of confluence of larger side-branches with complex geometry lacking a priori definitions for contour tracing. ICCs for mean and minimal signal-rich layer thickness were respectively 0.95 and 0.86 for intra-observer, and 0.80 and 0.80 for inter-observer variability.

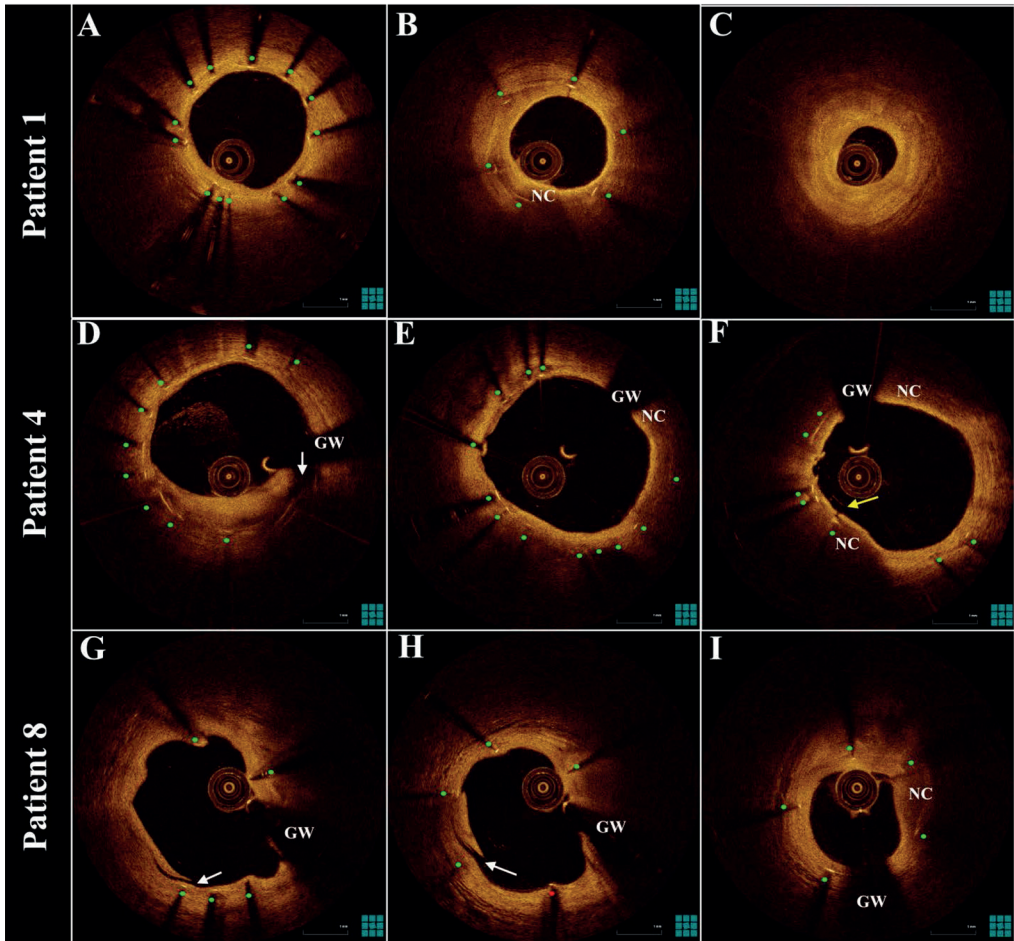


Figure 6.11 | Representative OCT images of metal drug-eluting stents. A) Covered struts (green bullet), B) Neoatherosclerosis, C) Distal edge stenosis (area=1.74 mm²). D) Heterogeneous neointima with discontinuity (white arrow), E) Neoatherosclerosis, F) Neointimal disruption (yellow arrow) over necrotic core with mural thrombus. G) Evaginations - neointimal discontinuity (white arrow) possibly iatrogenic, H) Uncovered strut (red bullet), I) Neoatherosclerosis. *Abbreviations:* GW, guidewire; NC, necrotic core.

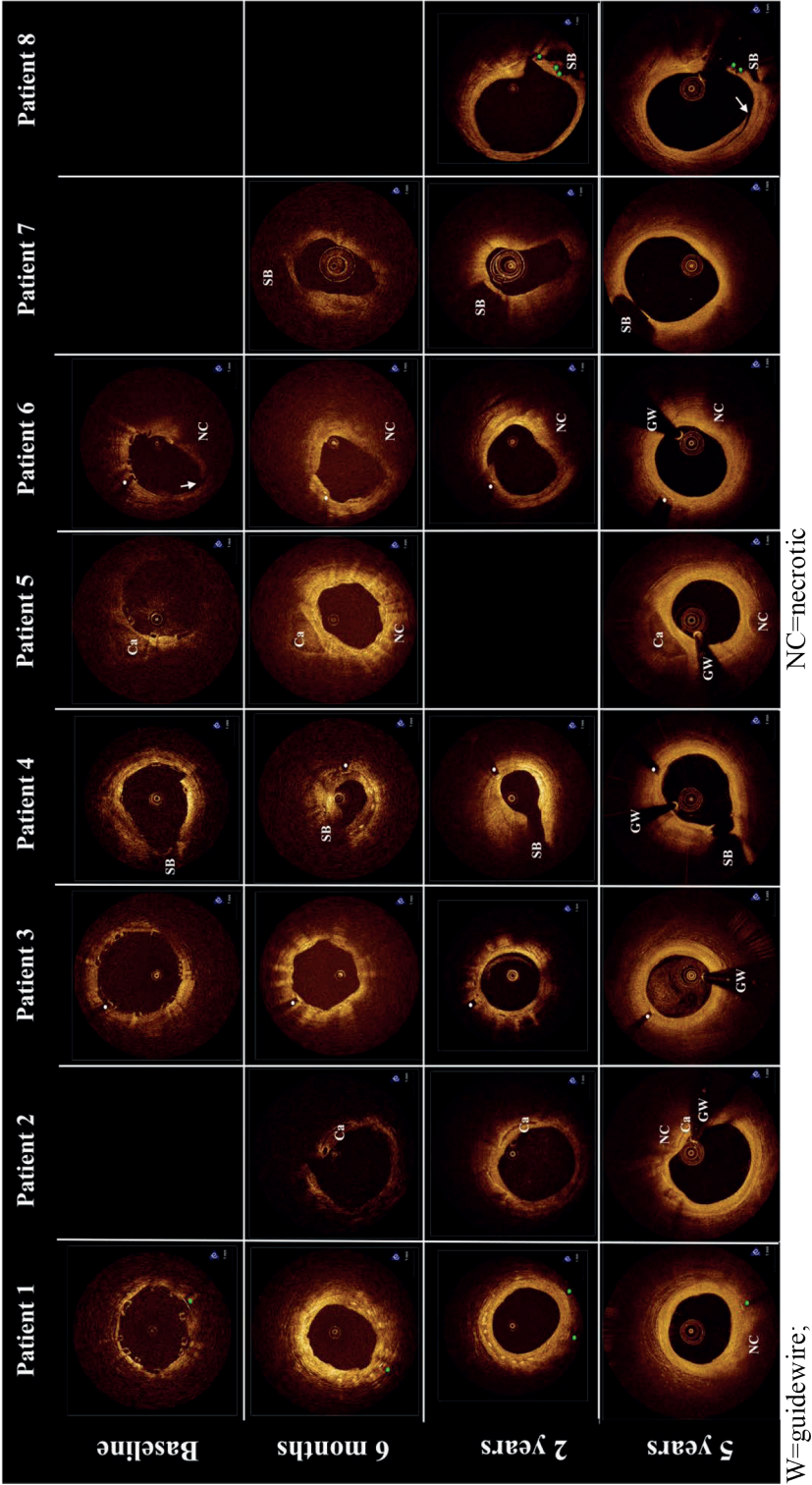


Figure 6.12 | Serial assessment of vascular response. Matched representative images from serial examinations of all patients. Note the complete strut integration at 5 years, together with lumen enlargement compared to the 6-month and 2-year follow-ups. In Patient 8, ‘sealing layer’ discontinuity (arrow), presumably iatrogenic, is observed. Abbreviations: white bullets, scaffold markers; green bullets, metal struts; SB, side-branch; GW, guidewire; NC, necrotic c.

6.4 | Discussion

We present the first in-vivo long-term OCT data 5 years after BVS implantation. Despite the small sample size, these first patients treated with BVS offer a unique opportunity to study the long-term vascular response after BVS implantation (Figure 6.12). Our main findings are that 5 years post BVS 1.0 implantation: 1) there is late lumen enlargement with simultaneous increase in luminal symmetry; 2) all struts have disappeared and been integrated within the neointima and the underlying plaque, forming a homogeneous, signal-rich, low-attenuating layer; 3) this signal-rich layer separates the lumen from the underlying plaque with a minimum thickness of 150 μm (IQR:120 μm –190 μm); 4) this effect is not universal, as there was one case with thinning and disruption of the signal-rich layer; 5) jailed side-branch ostia are preserved, while side-branch related struts have been replaced by thin tissue bridges; and 6) metal DES in the same vessels are lacking a distinct signal-rich layer and show neoatherosclerosis despite good coverage and apposition.

In our series, we observed a consistent luminal enlargement from 2 to 5 years in *all* patients. Late luminal enlargement in bioresorbable scaffolds has been attributed to outward remodeling in animal studies [14], and plaque burden reduction in clinical trials [4,15]. Our findings echo larger scale intravascular ultrasound (IVUS) observations of lumen area increase from 6 months to 2 years after BVS implantation [2,15]. IVUS observations in our study population were consistent with our findings, showing a trend for further lumen enlargement from 2 to 5 years, driven by a persistent decrease in plaque size from 6 months to 2 years either as a result of true plaque regression or pseudo-regression due to strut resorption [2,4]. A similar trend was also observed in the 5-year multi-slice computed tomography follow-up of ABSORB A [3]. Moreover, in our study, we observed a recovery of luminal symmetry. Although its clinical significance is unclear, simultaneous observations of strut bioresorption and signal-rich layer development suggest a potentially favorable biological effect. This is in accordance with IVUS studies showing increased plaque rupture in eccentric vessels [16]. The observed complete strut bioresorption is in line with vasomotion findings demonstrating a lack of mechanical vessel constraint, with positive acetylcholine response in 4 patients, negative response in 2 patients, and absence of significant change in only 2 patients [4].

It has been suggested that neointimal growth after BVS resorption could serve as a mechanical barrier preventing potentially thrombogenic plaque components from reaching the bloodstream, a concept dubbed ‘plaque sealing’ or ‘recapping the plaque’ [5,6]. With this hypothesis in mind, we scrutinized BVS morphology in our cohort, employing sophisticated algorithms for in-depth analysis.

We focused on the developed adluminal signal-rich layer, corresponding to neointima, bioresorbed struts and fibrous components of the underlying plaque. The minimum signal-rich layer thickness was 150 μm and the minimum cap thickness over necrotic core 155 ± 90 μm , which are far beyond the 65 μm threshold generally accepted as high-risk for plaque rupture [17], and suggests that this layer could reliably separate the lumen from potentially thrombogenic plaque components. Importantly, this layer showed remarkable homogeneity in the attenuation analysis, with low attenuation values hinting

to the absence of high-risk wall components such as necrotic core and macrophages within the layer [9,10]. Therefore we speculate that this signal-rich layer could be protective against very late scaffold thrombosis or de novo thrombosis by plaque progression and rupture [1,17].

The complete scaffold integration into the vascular wall has shaped a ‘neo-plaque’ phenotype as a result of the complex interaction of pre-existing plaque, morphological changes of the pre-existing plaque subject to dynamic local rheologic factors [18,19], strut resorption and neointima formation [8]. We visually characterized ‘neo-plaque’ using standardized OCT criteria [7]. Quantitative attenuation analysis corroborated these qualitative findings revealing co-localization of necrotic core regions with high attenuation regions (Supplementary Figure 6.7). High-attenuation regions were generally located deeper into the vessel wall and rarely observed within the first 200 μm from luminal surface. Of note, most patients were under intensive medical therapy (statins: 75%; beta-blockers: 75%; angiotensin receptor blockers: 62.5%), possibly contributing to this favorable phenotype.

Metal stents covered with well-organized and functional neointima can likewise present a mechanical barrier between underlying plaque and lumen. However, neointimal proliferation and neoatherosclerosis development over time have been consistently reported for BMS and even more accelerated for DES. The permanent nature of the metallic structure further massively limits the vessel's ability for remodeling, plaque regression and lumen enlargement over time (as in BVS). In consequence, lumen narrowing develops inevitably over time. Indeed, 3 metal drug-eluting stents in our cohort all showed adluminal neoatherosclerosis, with minimum cap thickness ranging from 70 to 110 μm . This is notable, as thin fibrous cap emerges as risk factor for neointimal rupture and acute coronary syndrome not only in native atherosclerosis, but also in neoatherosclerosis [1].

We analyzed the fate of side-branches jailed by BVS, as high strut thickness and the observation of tissue bridge formation has raised questions regarding long-term patency [12]. Three-dimensional rendering demonstrated side-branch patency, allowed reliable ostial measurements, and identified different intimal bridge patterns. Strut integration into these tissue bridges was completed without visible remnants, accompanied by bridge thinning from 341 ± 106 μm at 2 years to 227 ± 119 μm at 5 years. We consider these findings, together with the angiographically confirmed absence of flow impairment as a favorable long-term outcome. However, the implications of BVS over large side-branches or in true bifurcation lesions, both in terms of implantation technique and long-term patency, have yet to be understood [20,21], as these were excluded per protocol.

Overall, our long-term OCT observations suggest, in these patients treated with BVS and receiving intensive medical therapy, a favorable vascular healing response with late lumen enlargement, increased luminal symmetry, side-branch patency, complete strut resorption and the formation of a potentially protective tissue layer, giving an appearance consistent with the hypothetical concept of plaque sealing.

However, Patient 4 showed a different response capturing our attention. We observed target lesion progression with OCT findings consistent with macrophage infiltration, abluminal necrotic core

accumulation, fibrous cap thinning and plaque rupture at follow-up. The patient was under treatment only with aspirin and clopidogrel. Revision of all available data revealed diffuse disease necessitating non-target lesion revascularization with a metal paclitaxel-eluting stent in the same artery, 106 days after BVS implantation. This paclitaxel-eluting stent developed subsequent neoatherosclerosis with neointimal disruption and micro-thrombus formation (Figure 6.11). This evidence of accelerated atherosclerosis, combined with mechanical factors (baseline incomplete scaffold apposition, followed by late structural discontinuity) might have contributed to this adverse ‘neo-plaque’ phenotype. Notably, the patient did not suffer a clinically apparent acute coronary syndrome regardless of these impressive findings.

Despite the limited scale of our study, it provides crucial information on the long-term vascular response 5 years post BVS implantation. While we consider the overall vascular response favorable and in line with larger-scale clinical reports, there might be lessons to learn from observations in a single patient, who showed a different biological reaction with recurring plaque rupture after BVS implantation. This finding might underscore the need for an optimal acute mechanical result with optimal lesion coverage, while simultaneously raising questions regarding a possible responder/non-responder reaction to BVS and the need for intensified secondary prevention in selected patients in the future [22]. As such, our findings might guide further research for optimizing clinical efficacy of BVS in light of the 1.1 modifications and herald observations in more complex populations [23].

Study limitations: This is a small first-in-man study, containing only a fraction of patients of ABSORB A study. Selection bias cannot be excluded, although the baseline clinical and angiographic characteristics were not different from the entire ABSORB A cohort. BVS 1.0 assessed in our study differs in geometry and resorption rate compared to the currently used BVS 1.1, which might affect temporal course and pattern of the healing response.

Attenuation analysis has only been validated in ex vivo specimens of native atherosclerosis, and not in device-induced tissue responses. However, as attenuation is an optical property of tissue components, we expect the absence of high-attenuating regions to correspond to absence of necrotic core or macrophages also in this setting.

Five-year OCT follow-up was performed with a non-occlusive frequency-domain system, whereas previous OCT examinations with an occlusive time-domain system. Frequency-domain OCT offers better image quality and higher dynamic range, allowing superior visualization of deeply located plaques [24]. Due to these limitations of time-domain systems, serial assessment of plaque morphology behind the BVS was not systematically performed, and only examined with reference to possible neoatherosclerosis, although changes over time would be expected [19]. Occlusive time-domain OCT slightly underestimates lumen area [25]. Nevertheless, 4 patients in our study underwent additional non-occlusive OCT imaging at 2-year follow-up. Comparing non-occlusive data at 2 years to 5-year non-occlusive data, findings of late lumen enlargement were consistent, albeit not reaching significance due to smaller sample size (minimum lumen area: $3.54 \pm 1.43 \text{ mm}^2$ at 2 years versus $4.06 \pm 1.33 \text{ mm}^2$ at 5 years, $p=0.14$; mean lumen area: $5.12 \pm 1.62 \text{ mm}^2$ at 2 years versus $5.95 \pm 1.20 \text{ mm}^2$ at 5 years, $p=0.07$).

6.5 | Conclusions

At long-term follow-up 5 years after BVS implantation, a favorable tissue response is observed with late luminal enlargement, complete strut bioresorption and development of a low-attenuating, signal-rich layer covering underlying potentially thrombogenic plaque components. The small scale of our study and the observation of a different tissue response in one patient warrant the judicious interpretation of our results and further confirmation in larger studies.

6.6 | Acknowledgements

Antonios Karanasos acknowledges funding support from Hellenic Heart Foundation and St Jude Medical. Cihan Simsek and Muthukaruppan Gnanadesigan were supported by research grants from “Nederlandse Hartstichting” (CS:2009B091 and MG:2010B064). We would like to thank Dr. George Sianos for his role in ABSORB A trial, Prof. Johan Reiber and Joan Tuinenburg of ClinFact Core-Lab for the 5-year measurements external validation, and Prof. Guillermo Tearney for his expert review of (neo) plaque morphology.

Perspectives

Competency in Medical Knowledge. At long-term after bioresorbable scaffold implantation, we observed complete strut resorption and a favorable vascular healing response with late lumen enlargement, increased lumen symmetry, side-branch patency and the formation of a potentially protective tissue layer, giving an appearance consistent with the hypothetical concept of plaque sealing.

Competency in Patient Care. While the overall vascular healing response after bioresorbable scaffold implantation was favorable, a single patient showed a different biological reaction with recurring asymptomatic plaque rupture after bioresorbable scaffold implantation. This finding might underscore the need for an optimal acute mechanical result with optimal lesion coverage, while simultaneously raising questions regarding a possible responder/non-responder reaction to bioresorbable scaffolds and the need for intensified secondary prevention in selected patients in the future.

Translational Outlook. Our first-in-man, mechanistic study confirmed the concept of biodegradation accompanied with beneficial structural and compositional plaque changes. We demonstrated late lumen enlargement with development of a layer separating potentially thrombogenic plaque components from the lumen at long-term after bioresorbable scaffold implantation. Our observations warrant a more widespread clinical evaluation of BVS, as these observed effects could be associated with a long-term benefit for the majority of lesions and patients.

References

1. Karanasos A, Ligthart J, Witberg K et al. Association of neointimal morphology by optical coherence tomography with rupture of neoatherosclerotic plaque very late after coronary stent implantation. *SPIE conference proceedings*, 2013;856542-856542-13.
2. Serruys PW, Ormiston JA, Onuma Y et al. A bioabsorbable everolimus-eluting coronary stent system (ABSORB): 2-year outcomes and results from multiple imaging methods. *The Lancet* 2009;373:897-910.
3. Onuma Y, Dudek D, Thuesen L et al. Five-Year Clinical and Functional Multislice Computed Tomography Angiographic Results After Coronary Implantation of the Fully Resorbable Polymeric Everolimus-Eluting Scaffold in Patients With De Novo Coronary Artery Disease: The ABSORB Cohort A Trial. *JACC Cardiovasc Interv* 2013;6:999-1009.
4. Simsek C, Karanasos A, Magro M et al. Long-term Invasive Follow-Up of the Everolimus-Eluting Bioresorbable Vascular Scaffold: Five-year Results of Multiple Invasive Imaging Modalities. *EuroIntervention* 2014;in press.
5. Karanasos A, Simsek C, Serruys P et al. Five-Year Optical Coherence Tomography Follow-Up of an Everolimus-Eluting Bioresorbable Vascular Scaffold Changing the Paradigm of Coronary Stenting? *Circulation* 2012;126:e89-e91.
6. Brugaletta S, Radu MD, Garcia-Garcia HM et al. Circumferential evaluation of the neointima by optical coherence tomography after ABSORB bioresorbable vascular scaffold implantation: can the scaffold cap the plaque? *Atherosclerosis* 2012;221:106-12.
7. Tearney GJ, Regar E, Akasaka T et al. Consensus Standards for Acquisition, Measurement, and Reporting of Intravascular Optical Coherence Tomography Studies: A Report From the International Working Group for Intravascular Optical Coherence Tomography Standardization and Validation. *J Am Coll Cardiol* 2012;59:1058-1072.
8. Onuma Y, Serruys PW, Perkins LEL et al. Intracoronary Optical Coherence Tomography and Histology at 1 Month and 2, 3, and 4 Years After Implantation of Everolimus-Eluting Bioresorbable Vascular Scaffolds in a Porcine Coronary Artery Model An Attempt to Decipher the Human Optical Coherence Tomography Images in the ABSORB Trial. *Circulation* 2010;122:2288-2300.
9. van Soest G, Goderie T, Regar E et al. Atherosclerotic tissue characterization in vivo by optical coherence tomography attenuation imaging. *J Biomed Opt* 2010;15:011105.
10. Ughi GJ, Adriaenssens T, Sinnaeve P, Desmet W, D'Hooge J. Automated tissue characterization of in vivo atherosclerotic plaques by intravascular optical coherence tomography images. *Biomed Opt Express* 2013;4:1014-30.
11. Gnanadesigan M, van Soest G, White S et al. Effect of temperature and fixation on the optical properties of atherosclerotic tissue: a validation study of an ex-vivo whole heart cadaveric model. *Biomed Opt Express* 2014;5:1038-1049.
12. Okamura T, Onuma Y, García-García HM et al. 3-Dimensional Optical Coherence Tomography Assessment of Jailed Side Branches by Bioresorbable Vascular Scaffolds: A Proposal for Classification. *JACC Cardiovasc Interv* 2010;3:836-844.
13. Karanasos A, Tu S, van Ditzhuijzen NS et al. A novel method to assess coronary artery bifurcations by OCT: Cut-plane analysis for side-branch ostial assessment from a main vessel pullback. *Eur Heart J Cardiovasc Imaging*;in press.
14. Strandberg E, Zeltinger J, Schulz DG, Kaluza GL. Late Positive Remodeling and Late Lumen Gain Contribute to Vascular Restoration by a Non-Drug Eluting Bioresorbable Scaffold A Four-Year Intravascular Ultrasound Study in Normal Porcine Coronary Arteries. *Circulation Cardiovasc Interv* 2012;5:39-46.
15. Serruys PW, Onuma Y, Garcia-Garcia HM et al. Dynamics of vessel wall changes following the implantation of the absorb everolimus-eluting bioresorbable vascular scaffold: a multi-imaging modality study at 6, 12, 24 and 36 months. *EuroIntervention* 2014;9:1271-84.
16. von Birgelen C, Klinkhart W, Mintz GS et al. Plaque distribution and vascular remodeling of ruptured and nonruptured coronary plaques in the same vessel: an intravascular ultrasound study in vivo. *J Am Coll Cardiol* 2001;37:1864-1870.
17. Virmani R, Burke AP, Farb A, Kolodgie FD. Pathology of the vulnerable plaque. *J Am Coll Cardiol* 2006;47:C13-8.

18. Wentzel JJ, Schuurbiers JC, Gonzalo Lopez N et al. In vivo assessment of the relationship between shear stress and necrotic core in early and advanced coronary artery disease. *EuroIntervention* 2013;9:989-95.
19. Kubo T, Maehara A, Mintz GS et al. The dynamic nature of coronary artery lesion morphology assessed by serial virtual histology intravascular ultrasound tissue characterization. *J Am Coll Cardiol* 2010;55:1590-1597.
20. Ruzsa Z, van der Linden M, Van Mieghem NM et al. Culotte stenting with bioabsorbable everolimus-eluting stents. *Int J Cardiol* 2013;168:e35-7.
21. van Mieghem NM, Wilschut J, Ligthart J, Witberg K, van Geuns RJ, Regar E. Modified T-Technique with Bioresorbable Scaffolds ensures Complete Carina Coverage – an Optical Coherence Tomography Study. *JACC Cardiovasc Interv* 2014;in press.
22. Karanasos A, van Geuns RJ, Zijlstra F, Regar E. Very late bioresorbable scaffold thrombosis after discontinuation of dual antiplatelet therapy. *Eur Heart J* 2014.
23. Diletti R, Karanasos A, Muramatsu T et al. Everolimus-eluting bioresorbable vascular scaffolds for treatment of patients presenting with ST-segment elevation myocardial infarction: BVS STEMI first study. *Eur Heart J* 2014;35:777-86.
24. Manfrini O, Mont E, Leone O et al. Sources of error and interpretation of plaque morphology by optical coherence tomography. *Am J Cardiol* 2006;98:156-9.
25. Gonzalo N, Serruys PW, García-García HM et al. Quantitative ex vivo and in vivo comparison of lumen dimensions measured by optical coherence tomography and intravascular ultrasound in human coronary arteries. *Rev Esp Cardiol* 2009;62:615-624.

Chapter 7

Qualitative and quantitative evaluation of dynamic changes in non-culprit coronary atherosclerotic lesion morphology. A longitudinal OCT study

Bu-Chun Zhang, Antonios Karanasos, Muthukaruppan Gnanadesigan, Johannes N van der Sijde, Nienke S van Ditzhuijzen, Karen T Witberg, Jurgen MR Ligthart, Roberto Diletti, Robert-Jan van Geuns, Jouke Dijkstra, Felix Zijlstra, Gijs van Soest, Evelyn Regar

Submitted

Abstract

Background: Despite the well-described association between plaque morphology and acute coronary syndromes, there is limited in vivo evidence regarding the temporal evolution of non-culprit coronary plaque morphology. We evaluated changes in non-culprit plaque morphology over time by optical coherence tomography (OCT).

Methods and Results: 119 patients had undergone serial OCT examination of the same vessel in our institution between 1/1/2009 and 31/8/2014. Among those, 72 patients with 257 non-culprit segments fitted the inclusion criteria and were analyzed. Non-culprit coronary segments were matched between baseline and follow-up. OCT plaque characterization including automated attenuation analysis was performed for both time points and changes over a median follow-up of 6.2 months were evaluated. On segment level, lumen area decreased from baseline to follow-up, whereas fibrous cap thickness increased. Similarly, plaque attenuation indexes at follow-up were significantly decreased compared to baseline. In most segments (68.5%), plaque morphology did not change. Favorable change was observed in 18.4% of segments and unfavorable in 12.9%. There were no robust clinical predictors of favorable or unfavorable change in plaque morphology. Attenuation analysis supported the qualitative characterization, showing significantly different attenuation between different plaque types.

Conclusions: In non-culprit coronary segments of patients with coronary artery disease under standard medical therapy, fibrous cap thickness increases over time. However, in individual segments, there are observations of both plaque stabilization and destabilization, even within the same artery and patient. No clinical factor could reliably predict these changes, possibly implying a need for reconsideration of current hypotheses and adaptation of future study designs.

Keywords: thin-cap fibroatheroma; plaque rupture; plaque progression; coronary artery disease; optical coherence tomography

7.1 | Introduction

Vast post-mortem evidence suggests that morphological plaque characteristics such as thin fibrous cap and large necrotic core are implicated in plaque destabilization and triggering of plaque rupture [1,2]. However, despite this well-described association, prospective studies have only demonstrated a modest prognostic significance of plaque morphology for the prediction of future patient-level or lesion-level events in patients receiving optimal medical therapy [3-5]. Reasons for this discrepancy potentially include a high prevalence of such plaques and/or low specificity of intravascular imaging. In order to be able to enhance the prognostic capability of plaque characterization, a better in vivo identification of the true high-risk plaques is a prerequisite. Thus, it is necessary to further define the in vivo morphological characteristics associated with plaque progression, and document the morphological changes of atherosclerotic plaques over time under medical therapy.

Optical coherence tomography (OCT) is a high-resolution intravascular imaging modality which allows a comprehensive morphological characterization of the atherosclerotic plaque⁶. Morphological characterization can be further corroborated by automated plaque characterization software, such as quantitative attenuation analysis that provide a more objective assessment of plaque morphology [7].

We aimed to evaluate the changes in plaque morphology of non-culprit lesions over time by OCT using a qualitative and a quantitative approach, and further identify factors that are associated with these changes.

7.2 | Methods

7.2.1 | Study protocol

The OCT database of Erasmus MC was screened for patients undergoing serial OCT examinations of the same vessel with an interval >3 months. Patients, in whom the same non-culprit native atherosclerotic segment was visualized in both time points, were included in the study. The pullbacks were matched to each other using landmarks and synchronized by an automated algorithm (QCU-CMS, LKEB, Leiden, the Netherlands). OCT analysis was then performed in the matched vessel region, and changes from baseline to follow-up were recorded. Analysis was performed on a patient-level basis (entire imaged vessel) and on a segment-level basis (the imaged region was divided in equal sub-segments of 5mm and OCT morphology was assessed separately for each sub-segment). Additionally to conventional plaque characterization by visual assessment of the intensity map image, quantitative plaque characterization was performed by automated attenuation analysis. Demographic and clinical data were collected retrospectively. Informed consent was acquired from all patients for use of their imaging data and the study complies with the declaration of Helsinki.

7.2.2 | Study population

All patients >18 years old that underwent serial OCT examination of the same vessel for clinical or research purposes in Erasmus MC between 1 January 2009 and 31/8/2014, with an interval of >3 months between the two examinations were screened for inclusion. Patients, in whom the same non-culprit native coronary artery segment of at least 5 mm length and located >5 mm beyond the edge segment of a previously implanted device was identified in both pullbacks, were finally included. Exclusion criteria were invasive treatment of non-culprit lesion in the interval between baseline and follow-up, poor image quality not allowing assessment of plaque morphology in at least 3 quadrants of the cross-sectional image, and saphenous vein graft lesions.

7.2.3 | OCT analysis

7.2.3.1 | Selection of region of interest (ROI) and segment matching

Matching was performed using dedicated software (QCU-CMS). Baseline and follow-up pullbacks were simultaneously reviewed for identification of a matched native coronary segment. Identification of the segment was based on anatomic (side-branches) or device-specific (stent edges) landmarks. As longitudinal catheter motion does not allow precise co-registration by the use of a single landmark and length information [8], multiple landmarks were selected, and segment co-registration was automatically performed. This allowed for a synchronized scrolling between the two pullbacks, used to identify the frame numbers corresponding to the same non-culprit native coronary segment in the two pullbacks, thus comprising the region of interest (ROI). For the segment-level analysis, the baseline ROI was divided in 5 mm sub-segments, which were matched between the two pullbacks after identification of corresponding frames by synchronized scrolling.

7.2.3.2 | Lumen measurements

Lumen measurements were performed at 1mm intervals within the ROI and mean and minimal lumen area were calculated for patient and segment level.

7.2.3.3 | Plaque analysis

Plaque morphology was also assessed for patient and segment level at 1mm intervals within the ROI, using commonly accepted definitions [9]. The presence of necrotic core or calcium was recorded and the corresponding arc (in °) was measured. Measurements included mean and maximum necrotic core and calcium arc, and also relative volumetric indexes of necrotic core and calcium content.

The relative necrotic core index (RNCI) was calculated as:

$$RNCI = (\text{mean necrotic core arc} \times \text{necrotic core length}) / (360 \times \text{analyzed length}).$$

Similarly, the relative calcium index (RCI) was calculated as:

$$RCI = (\text{mean calcium arc} \times \text{calcium length}) / (360 \times \text{analyzed length}).$$

In cases of necrotic core, the overlying cap was measured over its entire surface by a semi-automated algorithm, with subsequent manual corrections if necessary. The minimum and average cap thicknesses

per patient and per segment were then calculated. Presence of macrophages, plaque rupture, and thrombus was also recorded [9,10].

7.2.3.1 | Interstudy variability

As analysis of matched segments might contain some bias of global measurements due to longitudinal catheter displacement [8], inter-study variability of the OCT measurements was calculated and only differences from baseline to follow-up that were higher than the limits of agreement were considered clinically relevant (online supplement).

7.2.3.1 | Hierarchical plaque characterization

Plaque characterization (Figure 7.1) was performed for patient and segment level using a hierarchical definition as follows:

- Thin-cap fibroatheroma (TCFA)*: Maximum necrotic core arc $>90^\circ$ and minimal fibrous cap thickness $\leq 65 \mu\text{m}$.
- Fibroatheroma*: Maximum necrotic core arc $>90^\circ$ and fibrous cap thickness $>65 \mu\text{m}$.
- Fibrocalcific*: Maximum calcium arc $>90^\circ$, with maximum necrotic core arc $\leq 90^\circ$.
- Fibrous*: Maximum necrotic core arc $\leq 90^\circ$ and maximum calcium arc $\leq 90^\circ$.

7.2.4 | Attenuation analysis

We further applied quantitative plaque characterization by attenuation analysis to corroborate findings from conventional OCT analysis [11]. The attenuation coefficient is a robust tissue optical parameter, which is increased in tissue types associated with plaque vulnerability, such as necrotic core and tissue macrophages, compared to more stable tissue types such as calcium and fibrous tissue [11,12]. Values of tissue attenuation for the entire perimeter of each cross-section for the entire studied segment were graphically plotted in a longitudinal attenuation map of the vessel. This mapping display of OCT depicts tissue optical properties in the entire pullback, demonstrating the maximum attenuation between lumen and intima-media border [13]. Thereby, a quantitative metric, namely the Index of Plaque Attenuation (IPA) is derived. IPA is a global metric of attenuation and is calculated as the fraction of pixels in the attenuation map with an attenuation coefficient greater than a certain threshold x , multiplied by a factor of 1000. The calculation of IPA can be represented as a mathematical formula as follows:

$$IPA_x = \frac{N(\mu_t > x)}{N_{\text{total}}} \times 1000 \quad (1)$$

where the numerator includes pixels with attenuation greater than certain threshold x . For this study, the IPA_6 and IPA_{11} indexes were calculated. IPA_6 has been associated with fibroatheroma morphology and IPA_{11} has been associated with TCFA morphology [14].

7.2.5 | Statistical analysis

All analyses were performed with SPSS 20.0 (IBM, Chicago, IL). Continuous variables are presented as mean \pm SD or median [interquartile range], while categorical variables are reported as count and

percentages. Statistical analysis was performed using mixed model regression and is described in the online supplement. All p-values are two-sided with a value <0.05 indicating significance.

7.3 | Results

A total of 119 patients had undergone serial OCT examination of the same vessel with an interval >3 months between 1st January 2009 and 31st August 2014 and were screened for inclusion. Thirty four were excluded due to inadequate length of the matched segments, four due to visualization of a different branch not allowing matching, six due to OCT imaging in a graft, two due to poor image quality, and one patient due to performance of intervention in the studied segment between the two OCT studies. Overall, 72 patients fitted the criteria and were included.

Baseline clinical characteristics are reported in Table 7.1. Mean age was 59.0 ± 11.0 years and 81.9% were male. Initial presentation was stable angina in 40.3% and acute coronary syndrome in 58.4%.

The median follow-up interval was 6.2 months [IQR 6.0–11.1 months]. In total, a mean vessel length of 17.83 ± 9.22 mm and 17.65 ± 9.00 mm were analyzed for baseline and follow-up, respectively.

7.3.1 | Changes in OCT morphological characteristics

7.3.1.1 | Patient-level analysis

Mean lumen area was decreased at follow-up (7.87 ± 3.68 mm² versus 8.22 ± 3.63 mm² at baseline; $p=0.049$). However, no changes were observed in patient-level OCT plaque morphology (Table 7.2). Similarly, there were no differences on patient-level attenuation metrics, with the exception of a borderline decrease of IPA_{11} at follow-up ($p=0.049$). Clinically relevant changes in lumen dimensions, calcium arc and cap thickness were observed in a minority of patients on a patient level (30–35%), however more than half of the patients had significant differences in the maximum necrotic core arc, with one third of the patients presenting with increase of the necrotic core content (Table 7.3).

7.3.1.2 | Segment-level analysis

Overall 257 non-culprit segments were assessed (Table 7.2). Both minimal and mean lumen area were significantly decreased at follow-up compared to baseline ($p=0.018$ and $p=0.005$, respectively). There were no significant differences in necrotic core or calcium metrics between the two intervals. However, both minimum and average cap thickness were increased at follow-up compared to baseline ($p=0.019$ and $p=0.002$, respectively). In addition, IPA_6 and IPA_{11} values at follow-up were significantly decreased compared to baseline ($p=0.036$ and $p=0.022$, respectively). As with patient-level analysis, significant changes of lumen dimensions, and calcium arc were observed in a minority of segments ($<40\%$) (Table 7.3). However, more than half of the segments had significant changes in cap thickness and maximum necrotic core arc.

Table 7.1 | Baseline characteristics.

Age (years)	58.98±10.95
Men n(%)	59(81.9)
Interval (months)	6.2[6.0-11.1]
Clinical presentation, baseline n(%)	
Stable angina	29(40.3)
Unstable angina	11(15.3)
STEMI	28(38.9)
NSTEMI	3(4.2)
Asymptomatic	1(1.4)
Clinical presentation, follow-up n(%)	
Stable angina	12(16.7)
Unstable angina	4(5.6)
NSTEMI	1(1.4)
Asymptomatic	55(76.4)
Hypertension n(%)	34(48.6)
Diabetes n(%)	8(11.1)
Dyslipidemia n(%)	36(52.2)
Current smoker n(%)	27(37.5)
Family history of CAD n(%)	38(53.5)
Prior infarction n(%)	12(16.7)
Prior PCI n(%)	13(18.1)
Prior CABG n(%)	1(1.4)
Chronic kidney disease n(%)	2(2.8)
Vessel n (%)	
LAD	38(52.8)
LCX	20(27.8)
RCA	14(19.4)
Therapy n (%)	
ACE inhibitors/ARBs	37(51.4)
Statins	63(87.5)
Beta-blocker	39(54.2)
Baseline total cholesterol, mmol/L	5.01±1.13
Baseline LDL-C, mmol/L	3.40±1.10
Baseline triglycerides, mmol/L	1.26±0.90
Analyzed length baseline, mm	17.83±9.22
Analyzed length follow-up, mm	17.65±9.00

Values expressed as mean±SD, median[interquartile range], or n(%). *Abbreviations:* STEMI, ST-elevation myocardial infarction; NSTEMI, non-ST-elevation myocardial infarction; CAD, coronary artery disease; PCI, percutaneous coronary interventions; CABG, coronary artery bypass graft surgery; LAD, left anterior descending artery; LCx, left circumflex; RCA, right coronary artery; ACE, acetylcholine converting enzyme; ARB, angiotensin receptor blocker; LDL-C, low-density cholesterol.

Table 7.2 | Patient- and segment-level plaque morphology at baseline and follow-up.

	Baseline	Follow-up	p-value*
Patient-level			
Minimal lumen area, mm ²	5.24±2.86	5.28±2.93	0.76
Mean lumen area, mm ²	8.22±3.63	7.87±3.68	0.049
Plaque morphology n(%)			0.81
Fibroatheroma	30(41.7)	34(47.2)	
Fibrocalcific	0	0	
Fibrous	16(22.2)	16(22.2)	
TCFA	26(36.1)	22(30.6)	
Mean necrotic core arc, (°)	99.9±35.6	96.7±35.4	0.21
Max necrotic core arc, (°)	170.9±67.4	174.1±79.7	0.67
RNCI, %	15.24±10.46	15.18±10.76	0.91
Mean calcium arc, (°)	72.1±51.0	62.0±42.8	0.25
Max calcium arc, (°)	100.7±83.8	90.6±82.9	0.31
RCI, %	1.87±6.03	1.85±6.75	0.92
Minimum cap thickness, µm	88±53	91±65	0.68
Average cap thickness, µm	183±62	209±67	0.01
IPA6, mm ⁻¹	480.71±144.97	464.36±152.76	0.48
IPA11, mm ⁻¹	52.40±41.00	44.73±36.23	0.049
Segment-level			
Minimal lumen area, mm ²	7.07±3.75	6.86±3.73	0.018
Mean lumen area, mm ²	8.15±4.14	7.92±3.98	0.005
Plaque morphology n(%)			0.84
Fibroatheroma	105(40.9)	110(42.8)	
Fibrocalcific	1(0.4)	0	
Fibrous	118(45.9)	123(47.9)	
TCFA	33(12.8)	24(9.3)	
Mean necrotic core arc, (°)	96.7±43.0	94.8±39.1	0.48
Max necrotic core arc, (°)	133.7±65.0	135.4±71.0	0.81
RNCI, %	15.33±15.07	15.15±14.27	0.76
Mean calcium arc, (°)	76.9±59.9	82.5±56.4	0.59
Max calcium arc, (°)	98.4±83.9	108.6±89.5	0.34
RCI, %	1.59±6.11	1.79±7.03	0.38
Minimum cap thickness, µm	120±75	134±81	0.019
Average cap thickness, µm	184±80	206±83	0.002
IPA6, mm ⁻¹	472.77±179.94	444.52±185.86	0.036
IPA11, mm ⁻¹	49.46±52.42	42.72±45.74	0.022

Values expressed as mean±SD, or n(%). P-values derived from mixed model regression for repeated measurements. *Abbreviations:* RNCI, relative necrotic core index; RCI, relative calcium index.

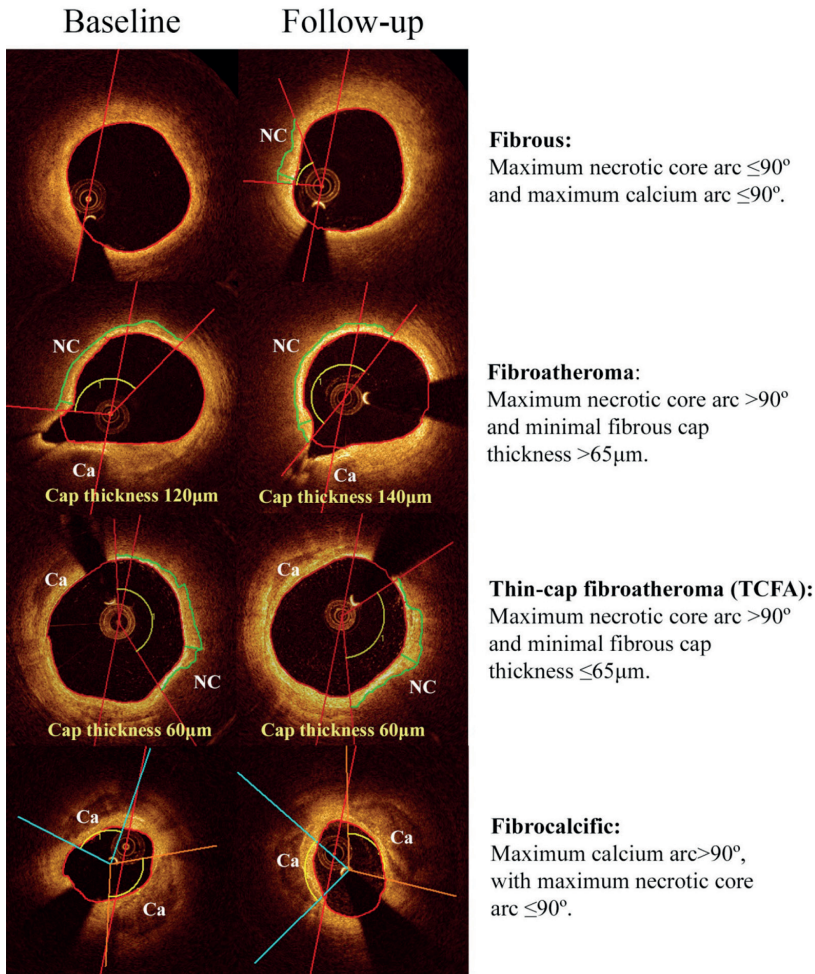


Figure 7.1 | Hierarchical plaque classification. Representative examples of: fibrous plaque, fibroatheroma, thin-cap fibroatheroma and fibrocalcific plaque. Red lines denote the arc of the necrotic core, and the green line the cap segmentation. *Abbreviations:* NC, necrotic core; Ca, calcium.

7.3.2 | Changes in hierarchical plaque morphology

The changes are summarized in Table 7.3 and Figure 7.2.

7.3.2.1 | Patient-level analysis

In most patients (58.3%), plaque morphology did not change. In 25% plaque morphology had a favorable change (i.e. change from TCFA to fibroatheroma, or from fibroatheroma/TCFA to fibrous), while an unfavorable change (i.e. change from fibrous to fibroatheroma/TCFA, or from fibroatheroma to TCFA) was observed in 16.7%. Most fibrous plaques showed no change in morphology (81%). Interestingly, 58% of the TCFA lesions were converted to fibroatheroma, while 30% of fibroatheromas gave rise to new TCFA lesions.

Table 7.3 | Changes in OCT characteristics over time.

	Patient-level (n=72)	Segment-level (n=257)
MLA		
Difference (follow-up – baseline), mm ²	0.05(–0.26 to 0.35)	–0.22(–0.39 to –0.04)
Lumen expansion, n(%)	12(16.7)	35(13.6)
No change, n(%)	47(65.3)	158(61.5)
Lumen narrowing, n(%)	13(18.1)	64(24.9)
Max necrotic core arc		
Difference (follow-up – baseline), °	3.4(–11.5 to 18.4)	1.0(–7.2 to 9.2)
Increase, n(%)	15(20.8)	67(26.1)
No change, n(%)	33(45.8)	124(48.2)
Decrease, n(%)	24(33.3)	66(25.7)
Max calcium arc		
Difference (follow-up – baseline), °	–10.8(–30.3 to 8.7)	7.2(–8.0 to 22.4)
Increase, n(%)	10(13.9)	32(12.5)
No change, n(%)	50(69.4)	202(78.6)
Decrease, n(%)	12(16.7)	23(8.9)
Minimum cap thickness		
Difference (follow-up – baseline), µm	6(–12 to 24)	16(2 to 29)
Increase, n(%)	12(19.0)	52(31.0)
No change, n(%)	40(63.5)	81(48.2)
Decrease, n(%)	11(17.5)	35(20.8)
Hierarchical morphology		
Favorable change, n(%)	18(25.0)	47(18.3)
FA → fibrous	3(4.2)	21(8.2)
TCFA → fibrous	0(0)	3(1.2)
TCFA → FA	15(20.8)	23(8.9)
No change, n(%)	42(58.3)	176(68.5)
Fibrous → Fibrous	13(18.1)	99(38.5)
FA → FA	18(25.0)	70(27.2)
TCFA → TCFA	11(15.3)	7(2.7)
Unfavorable change, n(%)	12(16.7)	33(12.8)
FA → TCFA	9(12.5)	14(5.4)
Fibrous → FA	1(1.4)	16(6.2)
Fibrous → TCFA	2(2.8)	3(1.2)

Values expressed as estimate (95% confidence interval), or n(%).

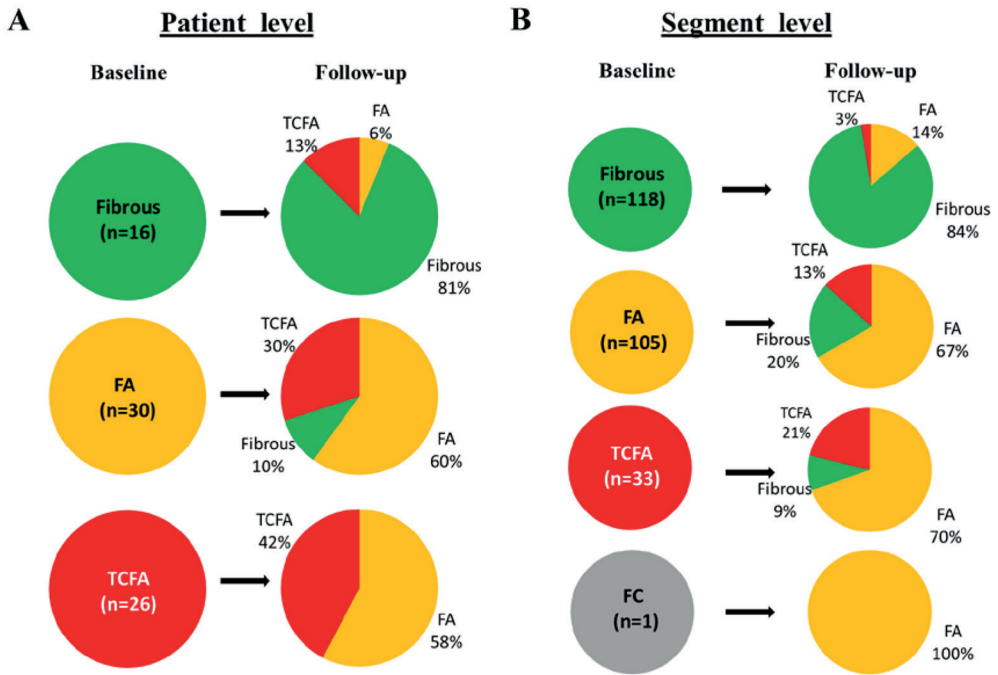


Figure 7.2 | Changes in hierarchical plaque morphology on A) patient level and B) segment level. *Abbreviations:* FA, fibroatheroma; TCFA, thin cap fibroatheroma; FC, fibrocalcific.

7.3.2.2 | Segment-level analysis

In line with patient-level data, 68.5% of segments showed no changes. Favorable change was observed in 18.4% of segments, and unfavorable change in 12.9%. Similarly to patient-level analysis, more than 80% of fibrous plaques had no change in morphology, while the majority of TCFA were converted to fibroatheromas, with the emergence of new TCFA from 13% of the fibroatheromas at baseline. As a result of these dynamic changes, the overall percentage of lesions with a specific morphology did not change over time for patient-level or segment-level (Table 7.2).

7.3.2.3 | Predictors of change in plaque characteristics assessed by OCT

Predictors of change in MLA, maximum necrotic core arc, maximum calcium arc, and minimum cap thickness are reported in Supplementary Table 7.2. Prediction of these changes from clinical factors was poor. Interval between the two follow-ups was associated with decrease in MLA ($p=0.004$), whereas family history of CAD with increase ($p=0.029$). From angiographic variables, LCx lesions had higher MLA increase compared to RCA ($p=0.043$), while location distal to the stented segment was associated with decrease in maximum necrotic core arc compared to proximally located lesions ($p=0.026$).

Factors associated with favorable or unfavorable change in plaque morphology are presented in Table 7.4. The only significant predictor of favorable change in plaque morphology was family history of CAD ($p=0.009$). Lesion location in LAD or LCx predicted less frequent favorable change and more frequent unfavorable change compared to RCA, however this difference did not reach significance.

Table 7.4 | Predictors of favorable and unfavorable change in plaque morphology.

	Favorable Odds ratio (95% CI)	Unfavorable Odds ratio (95% CI)
Age (per year)	1.006(0.972-1.041)	1.003(0.962-1.046)
Male gender	1.485(0.498-4.431)	1.384(0.393-4.871)
Interval (per month)	0.955(0.897-1.018)	1.044(0.984-1.107)
Myocardial infarction at baseline	1.085(0.523-2.251)	1.096(0.467-2.574)
Hypertension	0.894(0.425-1.879)	1.121(0.481-2.615)
Diabetes	1.621(0.452-5.813)	1.039(0.199-5.431)
Dyslipidemia	0.638(0.303-1.346)	1.331(0.560-3.161)
Current smoker	0.936(0.343-2.557)	0.787(0.253-2.452)
Family history of CAD	0.383(0.188-0.781)*	0.617(0.264-1.441)
Statin use	3.188(0.673-15.096)	1.043(0.289-3.762)
Total cholesterol (per mmol/L)	1.447(0.752-2.784)	0.940(0.555-1.590)
Vessel		
LAD	0.457(0.174-1.198)	6.609(0.810-53.913)
LCX	0.692(0.251-1.905)	3.383(0.372-30.747)
RCA	-	-
Location relative to stent		
No stent in artery	1.452(0.418-5.046)	1.449(0.412-5.105)
Distal to stent	1.842(0.855-3.968)	0.662(0.273-1.611)
Proximal to stent	-	-

* $p<0.05$.

7.3.3 | Attenuation analysis and plaque morphology

Attenuation analysis per plaque type for patient- and segment-level analyses are presented in Table 7.5. In both analyses, both IPA_6 and IPA_{11} differed significantly between plaque types, with values of both attenuation coefficients higher for TCFA compared to fibroatheroma or fibrous, and higher for fibroatheroma compared to fibrous (all p -values <0.05). Table 7.6 presents the association of these indexes with OCT variables. Both indexes had a strong positive correlation with necrotic core metrics and a strong negative correlation with cap thickness ($p<0.001$).

Table 7.5 | Association of hierarchical plaque classification with attenuation indexes.

	Plaque morphology	Value	p-value vs. FA	p-value vs. FC	p-value vs. fibrous
Patient-level					
IPA6, mm ⁻¹	TCFA	533.6±134.7	0.019		<0.001
	FA	485.206±122.4			0.015
	Fibrous	364.5±156.4			
IPA11, mm ⁻¹	TCFA	66.9±45.6	0.018		<0.001
	FA	48.7±31.6			0.006
	Fibrous	17.6±14.8			
Segment-level					
IPA6, mm ⁻¹	TCFA	605.3±127.7	0.013	0.163	<0.001
	FA	516.4±143.5		0.315	<0.001
	FC	398.1			0.903
	Fibrous	359.6±189.6			
IPA11, mm ⁻¹	TCFA	89.5±66.5	0.002	0.601	<0.001
	FA	53.4±46.7		0.891	<0.001
	FC	14.0			0.827
	Fibrous	30.0±60.7			

Values expressed as mean±SD. P-values derived from mixed model regression. *Abbreviations:* FA, fibroatheroma; FC, fibrocalcific; TCFA, thin cap fibroatheroma.

Table 7.6 | Association of segment-level OCT variables with attenuation indexes.

Dependent variable	IPA6 (mm ⁻¹)			IPA11 (mm ⁻¹)		
	b	95% CI	p value	b	95% CI	p value
Minimal lumen area, mm ²	0.001	-0.001 to 0.002	0.30	-0.003	-0.007 to 0.001	0.13
Mean lumen area, mm ²	0.001	-0.000 to 0.002	0.14	-0.003	-0.007 to 0.001	0.16
Mean necrotic core arc, (°)	0.089	0.064-0.113	<0.001	0.290	0.207-0.372	<0.001
Max necrotic core arc, (°)	0.139	0.097-0.179	<0.001	0.469	0.339-0.600	<0.001
RNCI, %	0.027	0.021-0.033	<0.001	0.063	0.043-0.084	<0.001
Mean calcium arc, (°)	0.097	0.027-0.167	0.008	0.233	0.045-0.420	0.016
Max calcium arc, (°)	0.063	-0.031 to 0.157	0.19	0.164	-0.089 to 0.419	0.20
RCI, %	0.002	-0.000 to 0.004	0.089	0.004	-0.003 to 0.011	0.27
Minimum cap thickness, μm	-0.157	-0.215 to -0.099	<0.001	-2.44	-0.428 to -0.061	0.009
Average cap thickness, μm	-0.160	-0.221 to -0.099	<0.001	-0.351	-0.543 to -0.160	<0.001

Values express estimates for increase in the dependent variable per unit increase of IPA6 and IPA11, respectively. P-values derived from mixed model regression. *Abbreviations:* CI, confidence intervals; RNCI, relative necrotic core index; RCI, relative calcium index.

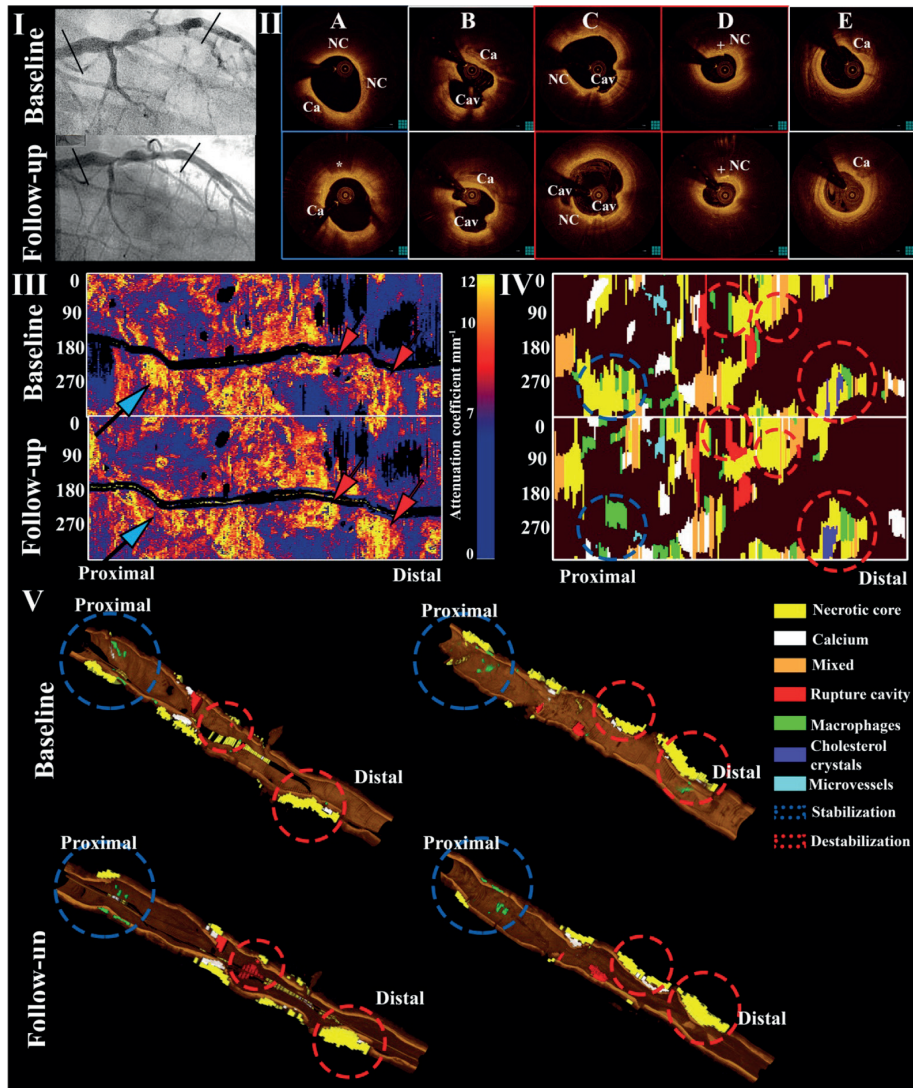


Figure 7.3 | Example of clinically-evident non-culprit lesion progression. I) Angiogram of LAD in a person presenting with new anginal symptoms 20 months after PCI of the LCx for unstable angina. II) Cross-sectional OCT images showing progressive narrowing at the region of a fibroatheroma distally (D). At the mid segment presence of two plaque rupture sites at baseline, and development of a third plaque rupture site at follow-up (B-C). A proximal fibroatheroma with regression of necrotic core at follow-up in comparison with baseline (A). III) Attenuation spread-out maps showing the longitudinal distribution of maximum attenuation coefficient values along the entire segment at baseline and follow-up. One site proximally had reduction (blue arrow), and two sites mid and distally increase (red arrow). IV) Plaque spread-out maps with color-coded tissues demonstrating reduction of the necrotic core proximally (blue circles), a new rupture at the mid segment and increase of the necrotic core distally (red circles). V) Three-dimensional longitudinal cut-away views of the same segment demonstrating the above-mentioned changes in plaque morphology (QAngioOCT 3D, Medis Specials bv, Leiden, NL). *Abbreviations:* Ca, calcium; NC, necrotic core; Cav, cavity; asterisk, macrophages; cross, cholesterol crystals.

7.3.4 | Clinically relevant changes in plaque morphology

There was only one patient with a new clinical syndrome attributed to lesion progression of the imaged segment (Figure 7.3). This patient that had been treated with stent implantation in the RCA due to NSTEMI, presented with stable angina 20 months later due to progression of a moderate mid LAD lesion. Intravascular imaging revealed progressive lumen narrowing in a lesion with fibroatheroma morphology, located distally to a segment with several sites of plaque rupture. Interestingly, in the same patient there was regression of a proximal lesion with reduction of the necrotic core size and lumen expansion.

7.4 | Discussion

In the current study, we performed comprehensive patient-level and segment-level OCT analyses of non-culprit plaque morphology, in order to evaluate the dynamic changes of coronary atherosclerosis under standard medical treatment. Quantitative attenuation analysis was used to corroborate findings from traditional plaque characterization. Our main findings were that in patients with coronary artery disease: 1) change in non-culprit plaque morphology over time occurs frequently, namely in 42% of patients and 31% of segments; 2) there are large differences between individual patients and segments with some demonstrating plaque stabilization and others plaque destabilization; 3) this effect is hidden when globally assessed in the entire cohort, with the exception of cap thickness where a modest thickening is observed; 4) these changes are rarely accompanied by clinical manifestations; and 5) prediction of these changes from clinical factors and based on their initial morphology is poor.

7.4.1 | Changes of non-culprit plaque morphology over time

Although pathologic studies have demonstrated a pivotal role for plaque morphology in ACS pathogenesis [1,2], the processes underlying changes in plaque morphology in vivo are poorly understood. A previous OCT study with single frame analysis of plaque morphology has demonstrated lesion progression and regression over 12 months at a similar incidence of around 30%, with no significant change in around 40% of the lesions. Interestingly, plaque stabilization with reduction of TCFA incidence was observed regardless of the changes in luminal dimensions [15]. In our study, at a median follow-up of 6 months in patients under standard medical therapy, 42% of patients and 31% of the non-culprit native atherosclerotic segments had a change of the plaque phenotype. Notably, despite a higher increase in necrotic core content and decrease in cap thickness, plaque morphology changed only in a minority of fibrous plaques, while TCFA and fibroatheromas often had dynamic changes in morphology. This finding suggests that fibrous plaques should be regarded as relatively stable plaque types with low potential for destabilization in a short time period, while fibroatheromas and TCFA are plaque morphologies prone to dynamic changes including both stabilization and destabilization within short time frame. Consequently, both plaque types could potentially progress to a culprit lesion over time, an observation supported by the finding of plaque rupture also in fibroatheromas with thicker caps [16,17].

7.4.2 | Change in fibrous cap thickness

Fibrous cap thickness is a major determinant of plaque vulnerability². In our study, on a segment level, minimum and average cap thickness increased from baseline to follow-up ($120.4 \pm 75.4 \mu\text{m}$ versus $134.4 \pm 80.8 \mu\text{m}$, $p=0.019$ and $183.5 \pm 80 \mu\text{m}$ versus $206 \pm 82.9 \mu\text{m}$, $p=0.002$, respectively). Increase in cap thickness has been demonstrated after administration of statins, and is considered to be associated with plaque stabilization [18]. This observation is further supported by a higher increase in cap thickness in patients receiving more intensive statin therapy [10]. These observations are in line with our findings, considering that most patients were being treated with statins, in the context of current recommendations for cardiovascular risk reduction in patients with coronary disease. Yet, despite this increase in cap thickness in the overall cohort, a non-negligible percentage of segments (21%) presented with fibrous cap thinning. This suggests that although statin treatment might promote plaque stabilization on a population level, this effect is not observed in all patients and in the entire coronary tree, with individual observations of cap thinning despite intensive systematic therapy. Thus, although medical therapy can promote plaque stabilization, this effect is not universal. This might call for additional or alternative (eventually local) therapeutic concepts and a tailored approach [13].

7.4.3 | Clinical relevance of the observed changes

Previous studies have demonstrated an association of non-culprit plaque morphology by intravascular ultrasound with virtual histology (VH-IVUS) with future adverse coronary events [3-5]. Yet, this association was only modest, considering the low incidence of adverse events, and a high prevalence of VH-TCFA (40-60%) and could in large part be explained by limitations of VH-IVUS in the detection of necrotic core and thin fibrous cap [19,20]. Our study underscores another important limitation of intracoronary imaging in identifying high-risk plaques. Even with high-resolution imaging, such as OCT, that can more accurately identify plaques with high-risk morphology [20], plaque morphology on its own has a poor predictive ability as it is subject to dynamic changes. These morphological changes can occur in the absence of clinical manifestations, while even our observation of clinically relevant progression due to progressive luminal narrowing in a setting of highly inflamed coronaries and non-culprit plaque ruptures, was seen in conjunction with plaque regression in another segment of the same patient, supporting the hypothesis that morphological plaque changes are highly localized and are observed on individual plaque level rather than on patient level.

Moreover, these changes in plaque morphology, were poorly predicted by patient-level or lesion-level factors. This finding implies a limited ability to predict lesion behavior. A possible explanation for this currently unpredictable behavior might be the effect of local hemodynamics on plaque morphology, as the presence of low wall shear stress has been associated with reduction of luminal dimensions and development of high-risk plaque morphology [5,21].

7.4.4 | Automated plaque characterization

For the objective documentation of plaque morphology, we used automated attenuation analysis. Increased attenuation has been associated with high-risk plaque characteristics such as necrotic core and macrophages [12]. The results of this analysis were in line with conventional OCT plaque

characterization showing increasing values of attenuation indexes from fibrous to fibroatheroma to TCFA, corroborating our analysis. Furthermore, the observations of strong correlations of these indexes with increased necrotic core content and reduced cap thickness suggest that such an analysis could be employed for monitoring changes in plaque morphology over time.

7.4.5 | Future perspectives

Our findings add to the current understanding of progression of non-culprit segment atherosclerosis in vivo under standard medical therapy. The finding of dynamic changes occurring even in different segments of the same patient underscores limitations of current imaging methods in detection of high-risk plaques [20], and a need for identification of additional markers of plaque instability. Consequently, the combined assessment of plaque morphology with local hemodynamics, or plaque morphology with local biochemical activity might be able to better identify plaques prone to progression [22,23]. Further, identification of additional morphological factors associated with plaque instability, such as assessment of the collagen content or fibrous cap microcalcifications might provide a better discrimination of high-risk plaques [24].

7.4.6 | Limitations

This is a small retrospective single-center registry investigating the changes in plaque morphology in non-culprit segments in patients under standard medical treatment. As such, our study is prone to the limitations of all retrospective, non-randomized studies. In order to account for the small sample a comprehensive analysis of plaque morphology was performed and further corroborated by quantitative attenuation analysis. Furthermore, the use of meticulously matched sub-segments allowed us to study changes of plaque morphology in a large number of segments and detect within-patient differences, not easy to detect with a patient-level analysis. Moreover, the absence of a pre-specified medical regimen does not allow generalization of our findings in specific populations. Finally, due to the limited patient sample and short follow-up, our study was clearly underpowered for identifying an association between changes in morphology and clinical events.

7.5 | Conclusions

In non-culprit coronary segments of patients with coronary artery disease under standard medical therapy, there is an increase in fibrous cap thickness over time. However, high differences are observed between individual segments with some segments demonstrating plaque stabilization and others plaque destabilization. None of the clinical factors could predict these changes possibly implying a need for reconsideration of current hypotheses and adaptation of future study designs.

7.6 | Disclosures

BCZ received financial support from China Postdoctoral Science Foundation Research Funds (Grant:2013M540468), The Natural Science Foundation of Jiangsu Province (Grant:BK20141137), and China Scholarship Council Fellowship (Grant: 201308310403). AK and JNvdS received research support from St Jude Medical. The Thoraxcenter has received research grants from St Jude Medical and Terumo Europe. No other conflicts of interest to disclose for the rest of the authors.

References

1. Falk E, Nakano M, Bentzon JF, Finn AV, Virmani R. Update on acute coronary syndromes: the pathologists' view. *Eur Heart J*. 2013;34:719-728
2. Virmani R, Burke AP, Farb A, Kolodgie FD. Pathology of the vulnerable plaque. *J Am Coll Cardiol*. 2006;47:C13-18
3. Calvert PA, Obaid DR, O'Sullivan M, Shapiro LM, McNab D, Densem CG, Schofield PM, Braganza D, Clarke SC, Ray KK, West NE, Bennett MR. Association between IVUS findings and adverse outcomes in patients with coronary artery disease: the VIVA (VH-IVUS in Vulnerable Atherosclerosis) Study. *JACC Cardiovasc Imaging*. 2011;4:894-901
4. Cheng JM, Garcia-Garcia HM, de Boer SP, Kardys I, Heo JH, Akkerhuis KM, Oemrawsingh RM, van Domburg RT, Ligthart J, Witberg KT, Regar E, Serruys PW, van Geuns RJ, Boersma E. In vivo detection of high-risk coronary plaques by radiofrequency intravascular ultrasound and cardiovascular outcome: results of the ATHEROREMO-IVUS study. *Eur Heart J*. 2014;35:639-647
5. Stone PH, Saito S, Takahashi S, Makita Y, Nakamura S, Kawasaki T, Takahashi A, Katsuki T, Nakamura S, Namiki A, Hirohata A, Matsumura T, Yamazaki S, Yokoi H, Tanaka S, Otsuji S, Yoshimachi F, Honye J, Harwood D, Reitman M, Coskun AU, Papafaklis MI, Feldman CL, Investigators P. Prediction of progression of coronary artery disease and clinical outcomes using vascular profiling of endothelial shear stress and arterial plaque characteristics: the PREDICTION Study. *Circulation*. 2012;126:172-181
6. Karanasos A, Ligthart J, Witberg K, van Soest G, Bruining N, Regar E. Optical Coherence Tomography: Potential Clinical Applications. *Curr Cardiovasc Imaging Rep*. 2012;5:206-220
7. Regar E, Gnanadesigan M, Van der Steen AF, van Soest G. Quantitative optical coherence tomography tissue-type imaging for lipid-core plaque detection. *JACC Cardiovasc Interv*. 2013;6:891-892
8. van Ditzhuijzen NS, Karanasos A, Bruining N, van den Heuvel M, Sorop O, Ligthart J, Witberg K, Garcia-Garcia HM, Zijlstra F, Duncker DJ, van Beusekom HM, Regar E. The impact of Fourier-Domain optical coherence tomography catheter induced motion artefacts on quantitative measurements of a PLLA-based bioresorbable scaffold. *Int J Cardiovasc Imaging*. 2014;30:1013-1026
9. Jang IK, Tearney GJ, MacNeill B, Takano M, Moselewski F, Iftima N, Shishkov M, Houser S, Aretz HT, Halpern EF, Bouma BE. In vivo characterization of coronary atherosclerotic plaque by use of optical coherence tomography. *Circulation*. 2005;111:1551-1555
10. Komukai K, Kubo T, Kitabata H, Matsuo Y, Ozaki Y, Takarada S, Okumoto Y, Shiono Y, Orii M, Shimamura K, Ueno S, Yamano T, Tanimoto T, Ino Y, Yamaguchi T, Kumiko H, Tanaka A, Imanishi T, Akagi H, Akasaka T. Effect of atorvastatin therapy on fibrous cap thickness in coronary atherosclerotic plaque as assessed by optical coherence tomography: the EASY-FIT study. *J Am Coll Cardiol*. 2014;64:2207-2217
11. Gnanadesigan M, van Soest G, White S, Scoltock S, Ughi GJ, Baumbach A, van der Steen AF, Regar E, Johnson TW. Effect of temperature and fixation on the optical properties of atherosclerotic tissue: a validation study of an ex-vivo whole heart cadaveric model. *Biomedical Optics Express*. 2014;5:1038-1049
12. van Soest G, Goderie T, Regar E, Koljenovic S, van Leenders GL, Gonzalo N, van Noorden S, Okamura T, Bouma BE, Tearney GJ, Oosterhuis JW, Serruys PW, van der Steen AF. Atherosclerotic tissue characterization in vivo by optical coherence tomography attenuation imaging. *J Biomed Opt*. 2010;15:011105
13. Karanasos A, Simsek C, Gnanadesigan M, van Ditzhuijzen NS, Freire R, Dijkstra J, Tu S, Van Mieghem N, van Soest G, de Jaegere P, Serruys PW, Zijlstra F, van Geuns RJ, Regar E. OCT assessment of the long-term vascular healing response 5 years after everolimus-eluting bioresorbable vascular scaffold. *J Am Coll Cardiol*. 2014;64:2343-2356
14. Gnanadesigan M. Optical coherence tomography tissue type (OC3T) imaging: attenuation index for plaque diagnosis (abstract). *Spie Photonics West*. 2015
15. Xie Z, Tian J, Ma L, Du H, Dong N, Hou J, He J, Dai J, Liu X, Pan H, Liu Y, Yu B. Comparison of optical coherence tomography and intravascular ultrasound for evaluation of coronary lipid-rich atherosclerotic plaque progression and regression. *Eur Heart J Cardiovasc Imaging*. 2015
16. Toutouzas K, Karanasos A, Tsiamis E, Riga M, Drakopoulou M, Synetos A, Papanikolaou A, Tsioufis C, Androulakis A, Stefanadi E, Tousoulis D, Stefanadis C. New insights by optical coherence tomography into the differences and similarities of culprit ruptured plaque morphology in non-ST-elevation myocardial infarction and ST-elevation myocardial infarction. *Am Heart J*. 2011;161:1192-1199

17. Toutouzas K, Tsiamis E, Karanasos A, Drakopoulou M, Synetos A, Tsioufis C, Tousoulis D, Davlourous P, Alexopoulos D, Bouki K, Apostolou T, Stefanadis C. Morphological characteristics of culprit atheromatic plaque are associated with coronary flow after thrombolytic therapy: new implications of optical coherence tomography from a multicenter study. *JACC Cardiovasc Interv.* 2010;3:507-514
18. Takarada S, Imanishi T, Kubo T, Tanimoto T, Kitabata H, Nakamura N, Tanaka A, Mizukoshi M, Akasaka T. Effect of statin therapy on coronary fibrous-cap thickness in patients with acute coronary syndrome: assessment by optical coherence tomography study. *Atherosclerosis.* 2009;202:491-497
19. Pu J, Mintz GS, Brilakis ES, Banerjee S, Abdel-Karim AR, Maini B, Biro S, Lee JB, Stone GW, Weisz G, Maehara A. In vivo characterization of coronary plaques: novel findings from comparing greyscale and virtual histology intravascular ultrasound and near-infrared spectroscopy. *Eur Heart J.* 2012;33:372-383
20. Brown AJ, Obaid DR, Costopoulos C, Parker RA, Calvert PA, Teng Z, Hoole SP, West NE, Goddard M, Bennett MR. Direct Comparison of Virtual-Histology Intravascular Ultrasound and Optical Coherence Tomography Imaging for Identification of Thin-Cap Fibroatheroma. *Circ Cardiovasc Imaging.* 2015;8:e003487
21. Vergallo R, Papafaklis MI, Yonetsu T, Bourantas CV, Andreou I, Wang Z, Fujimoto JG, McNulty I, Lee H, Biasucci LM, Crea F, Feldman CL, Michalis LK, Stone PH, Jang IK. Endothelial shear stress and coronary plaque characteristics in humans: combined frequency-domain optical coherence tomography and computational fluid dynamics study. *Circ Cardiovasc Imaging.* 2014;7:905-911
22. Toutouzas K, Chatzizisis YS, Riga M, Giannopoulos A, Antoniadis AP, Tu S, Fujino Y, Mitsouras D, Doulaverakis C, Tsampoulatis I, Koutkias VG, Bouki K, Li Y, Chouvarda I, Cheimariotis G, Maglaveras N, Kompatsiaris I, Nakamura S, Reiber JH, Rybicki F, Karvounis H, Stefanadis C, Tousoulis D, Giannoglou GD. Accurate and reproducible reconstruction of coronary arteries and endothelial shear stress calculation using 3D OCT: comparative study to 3D IVUS and 3D QCA. *Atherosclerosis.* 2015;240:510-519
23. Wang H, Gardecki JA, Ughi GJ, Jacques PV, Hamidi E, Tearney GJ. Ex vivo catheter-based imaging of coronary atherosclerosis using multimodality OCT and NIRAF excited at 633 nm. *Biomedical Optics Express.* 2015;6:1363-1375
24. Toutouzas K, Benetos G, Karanasos A, Chatzizisis YS, Giannopoulos AA, Tousoulis D. Vulnerable plaque imaging: updates on new pathobiological mechanisms. *Eur Heart J.* 2015;36:3147-3154

Chapter 8

OCT-measured plaque free wall angle is indicative for plaque burden: overcoming the main limitation of OCT?

Ayla Hoogendoorn, Muthukaruppan Gnanadesigan, Guillaume Zahnd,
Nienke S. van Ditzhuijzen, Johan C. H. Schuurbiers, Gijs van Soest,
Evelyn Regar, Jolanda J. Wentzel

Submitted

Abstract

Purpose: The aim of this study was to investigate the relationship between the plaque free wall (PFW) measured by optical coherence tomography (OCT) and the plaque burden (PB) measured by intravascular ultrasound (IVUS). We hypothesize that measurement of the PFW could potentially help to estimate the PB, thereby overcoming the limited ability of OCT to visualize the external elastic membrane in the presence of plaque. This could enable selection of the optimal stent-landing zone by OCT, which is traditionally defined by IVUS as a region with a $PB < 40\%$.

Methods: PB (IVUS) and PFW angle (OCT and IVUS) were measured in 18 matched IVUS and OCT pullbacks acquired in the same coronary artery. We determined the relationship between OCT measured PFW (PFW_{OCT}) and IVUS PB (PB_{IVUS}) by non-linear regression analysis. An ROC-curve analysis was used to determine the optimal cut-off value. Sensitivity, specificity, positive predictive value (PPV) and negative predictive value (NPV) were calculated for the detection of $PB < 40\%$.

Results: There is a significant correlation between PFW_{OCT} and PB_{IVUS} ($r^2=0.59$). The optimal cut-off value of the PFW_{OCT} for the prediction of a $PB_{IVUS} < 40\%$ is $\geq 220^\circ$ with a specificity of 78% and an NPV of 88%.

Conclusion: This study shows that PFW_{OCT} can be considered as a surrogate marker for PB_{IVUS} , which is currently a common criterion to determine optimal stent-landing zone.

Keywords: Optical coherence tomography, intravascular ultrasound, plaque free wall, plaque burden, stent-landing zone

8.1 | Introduction

In recent years, intravascular optical coherence tomography (OCT) has emerged as imaging technique for guiding percutaneous coronary intervention (PCI). OCT offers a very high spatial and lateral resolution compared to intravascular ultrasound (IVUS). However, this comes at the expense of penetration depth into the tissue [1]. Based on IVUS studies, the plaque burden (PB) is a leading criterion for a stent-landing zone, where areas with $PB < 40\%$ [2] $p < 0.001$ are considered optima. The ability of OCT to visualize plaque burden is limited by optical attenuation: the signal decrease with depth in tissue. Either a thick layer of fibrous (low-attenuation) plaque or the presence of superficial (high-attenuation) lipids or dense macrophage accumulations [3], may obscure the visibility of the media behind the plaque. This potentially limits the use of OCT to guide stent implantation when it comes to the selection of the optimal stent landing zones within the target artery. More recently, the absence of lipid/necrotic core within the landing zone has been advocated in addition to low plaque burden [4], a criterion which can be very well identified by OCT, in contrast to IVUS.

In a previous study [5] we tested the hypothesis that plaque free wall (PFW, we demonstrated a strong inverse linear relationship between PB and the plaque free wall (PFW) angle using IVUS imaging (PB_{IVUS} and PFW_{IVUS}). In the present study we hypothesize that the angle of the PFW measured in OCT (PFW_{OCT}) can likewise reflect the PB. Second, we postulate that regions with a $PB < 40\%$ can be selected for finding an optimal stent-landing zone. When the PFW angle is small ($< 180^\circ$), it might be instantly clear that disease is present with a $PB > 40\%$, thus forming a suboptimal stent-landing zone. Similarly, sections with a large PFW angle $> 270^\circ$ can be easily and reliably identified by OCT as optimal stent-landing zones with a $PB < 40\%$. However, in the intermediate region between 180° - 270° PFW, the interpretation might be more ambiguous. The aim of this study was to investigate the relationship between PFW_{OCT} and $IVUS_{PB}$ and establish the utility (expressed in predictive values for $PB < 40\%$) of this relationship to detect $PB < 40\%$ for selection of the optimal stent landing zone by OCT.

8.2 | Materials and Methods

8.2.1 | Study population

To study the predictive value of the OCT_{PFW} for determination of the PB, we performed a retrospective observational study. NIRS-IVUS (TVC, InfraRedx, Burlington, Massachusetts, USA) and OCT (St. Jude Medical Inc., St. Paul, MN, USA) pullbacks of the same ROI were used from 18 left anterior descending (LAD) coronary arteries of 18 patients with stable or unstable coronary syndrome included in the OCT study (Erasmus MC, Rotterdam).

The NIRS-IVUS images were acquired using a commercially available hybrid optical/ultrasound catheter with an automated pullback (pullback speed 0.5 mm/sec and 16 frames per second). The OCT images were obtained with C7-XR/Illumien and Dragonfly catheter. Automated OCT pullback (pullback speed 20 mm/s) was performed during simultaneous iso-osmolar X-ray contrast medium (Visipaque 320,

GE Healthcare, Buckinghamshire, U.K.) delivery through the guide catheter, using a power injector (Medrad ProVis, Bayer HealthCare LLC, NJ, U.S.A; typical flush rate 3.0 ml/s).

8.2.3 | Analysis

The OCT and IVUS pullbacks were matched by overlaying the frames with same side branches. The remainder of the frames was linearly interpolated in between the side branches. Matched NIRS-IVUS and OCT images were analyzed every millimeter over a ROI of the most proximal 20 mm of a pullback. On the IVUS images, the external elastic lamina (vessel area=VA) and lumen area (LA) contours were drawn using QCU-CMS software (version 4.69, Leiden University Medical Centre, LKEB, Division of Image Processing). These contours were used for the calculation of the plaque area (PA=VA-LA) and subsequently the PB (PA/VA*100%). PFW angle was defined from the center of the lumen as the arc of the cross-section with a visible, healthy wall having an intima-media thickness of less than 0.5 mm in both imaging modalities. In total, 360 frames were analyzed on both the IVUS and OCT images. The frame data were averaged over 3 mm sections to increase robustness and to compensate for imprecise matching. Images that showed a side branch either on IVUS or OCT, with the wall out of view or a bad flush were excluded. This resulted in 106 matched IVUS and OCT 3mm sections suitable for analysis. A total of 10 out of the 18 pullbacks of OCT and IVUS were analyzed by two independent expert observers for assessment of the reproducibility.

8.2.4 | Statistics

Statistical analysis was performed using SPSS software (version 21.0, SPSS Inc., Chicago, IL, USA). Findings were regarded significant when $p < 0.05$. The reproducibility of all PFW and PB measurements was assessed by performing an inter-observer agreement analysis to calculate the intraclass correlation coefficient.

Both a linear and a non-linear model were used to assess the relation between $PFW_{IVUS/OCT}$ and PB_{IVUS} . The non-linear model was defined as follows:

$$\begin{aligned} PB_{IVUS} &= a \times PFW + b & \text{for } PFW \leq \frac{(e-b)}{(a-d)} \\ PB_{IVUS} &= d \times PFW + e & \text{for } > \frac{(e-b)}{(a-d)} \end{aligned}$$

computed for both PFW_{OCT} and PFW_{IVUS} . For the non-linear regression analysis, the following starting parameters were chosen: $a=0$; $b=55$; $d=-0.2$; $e=100$. We denote the crossover value between both linear regimes as $PFW_c = (e-b)/(a-d)$, resulting from the regression.

To test whether the slope of the relationship between PFW_{OCT} vs PB_{IVUS} and PFW_{IVUS} vs PB_{IVUS} was similar, implying that with PFW_{OCT} and PFW_{IVUS} the same PB is predicted, a student's t-test for two independent samples was used. An ROC-curve analysis was performed to find the optimal cut-off value of PFW_{OCT} to predict a $PB_{IVUS} < 40\%$. Based on the optimal cut-off value, the sensitivity, specificity, positive predictive value (PPV) and negative predictive value (NPV) of PFW_{OCT} for prediction of $PB_{IVUS} < 40\%$ were calculated.

8.3 | Results

8.3.1 | Relation between PFW and PB in IVUS

PFW_{IVUS} and PB_{IVUS} were significantly, inversely related ($r^2=0.78$) which confirmed the findings of our previous publication [5] we tested the hypothesis that plaque free wall (PFW. However, a closer fit to the model was found by applying a non-linear regression line ($r^2=0.82$) (Figure 8.1a), with $PFW_C=183^\circ$.

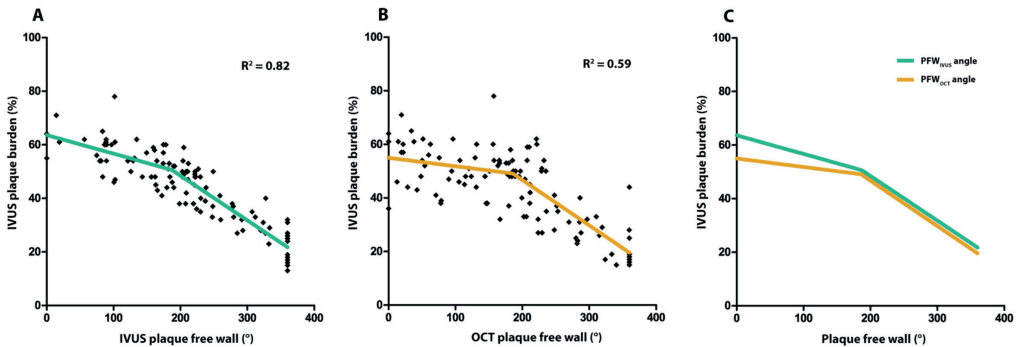


Figure 7.1 | Relationship between the plaque free wall (PFW) angle and plaque burden (PB). A) The PFW_{IVUS} measured shows a strong inverse, non-linear correlation with the IVUS PB with a breakpoint at 183° PFW. B) A similar relationship is seen for the OCT PFW angle and the IVUS PB with a breakpoint at 186° PFW. C) Overlay of regression lines of A) and B). PFW_{OCT} and PFW_{IVUS} perform equally well in predicting PB in the region of PFW angle $>186^\circ$. In the more diseased regions, the predictive value of the OCT PFW angle is reduced compared to IVUS.

8.3.2 | Predictive value of PFW_{OCT}

To assess whether the PFW_{OCT} could serve as a surrogate marker for PB_{IVUS} , the PFW_{OCT} values were plotted against the PB_{IVUS} values. Again, a non-linear regression relationship proved significant ($r^2=0.59$) (Figure 8.1b) with $PFW_C=186^\circ$. Interestingly, both IVUS and OCT show the same slope (student's t-test for inequality of slopes; $p=NS$) to predict PB for $PFW \geq 186^\circ$. For $PFW < 186^\circ$, PFW_{OCT} had no clear relationship with the PB, contrasting the PFW_{IVUS} which still showed a weak relationship with the PB (Figure 8.1c).

To find the optimal cut-off value of the PFW_{OCT} to predict a $PB_{IVUS} < 40\%$, an ROC-curve analysis was performed. Optimization of sensitivity, specificity, PPV and NPV resulted in a PFW_{OCT} cut-off value of $\geq 220^\circ$ (Figure 8.2). With this cut-off value, an optimal stent-landing zone ($PB < 40\%$) could be predicted correctly in 78% of the cases (PPV) (Figure 8.3). Just as important, the NPV was 88%, meaning that if the PFW angle is $< 220^\circ$, $PB > 40\%$ and thus forming a suboptimal stent-landing zone in 88% of the

cases. This high negative predictive value will largely prevent stenting too far into a health vessel region (PB<40%).

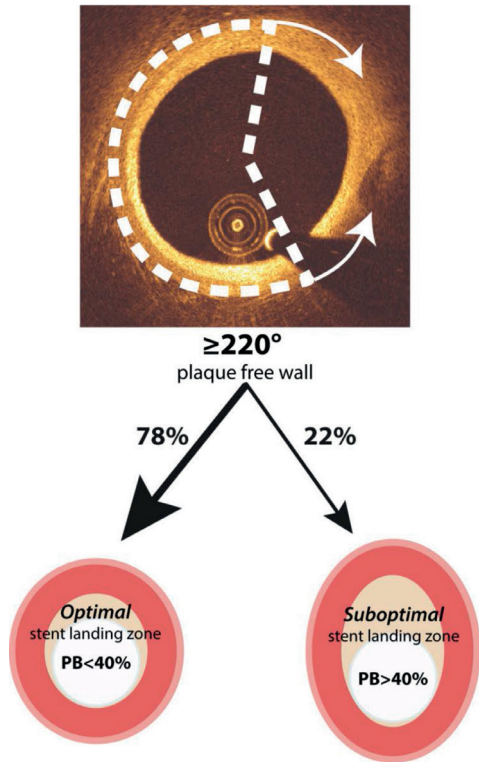


Figure 7.2 | Clinical application of PFW angle detection. When a PFW of $\geq 220^\circ$ is seen on OCT, in 78% of the cases this indicates the presence of a PB<40% and thus an optimal stent landing zone.

As an angle of 220 degrees might be difficult to judge by simple eyeballing in the cathlab, we investigated the predictive value of 180 degrees for PB<40% and thus a suitable stent-landing zone. Despite the strong relationship between PFW_{OCT} and PB_{IVUS} , regions with a PFW angle $>180^\circ$ can be regarded as an optimal stent landing zone with a PB<40% in only 57% of the cases. So strikingly, in 43% of the cases the disease is more severe with a PB>40%, even with only half of the circumference being occupied by plaque.

8.3.3 | Reproducibility

Inter-observer agreement analyses of the PFW measurements were performed in 189 OCT and 177 IVUS frames and showed high intraclass correlation coefficients of respectively 0.956 (95% CI: 0.941-0.967) and 0.912 (95% CI: 0.884-0.934). The intraclass correlation coefficient of the PB_{IVUS} measurements was equally high at 0.886 (95% CI: 0.847-0.915).

8.4 | Discussion

This study shows for the first time that PFW_{OCT} can be considered as a surrogate marker for PB, which is currently a common criterion to determine stent-landing zone. In regions with a PFW angle $>186^\circ$, the PFW_{OCT} has the same predictive value compared to PFW_{IVUS} . The optimized cut-off value to predict optimal stent landing zone ($\text{PB}<40\%$) is $\geq 220^\circ$ PFW_{OCT} . A cut-off value of 180° PFW_{OCT} is not sufficiently specific for $\text{PB}<40\%$, even though it is easier to apply in clinical routine.

There is a precarious balance between adequate lesion coverage and using too long stents. The first strategy poses a risk on plaque disruption and edge dissections when the edge of the stent lands in a plaque area. On the other hand, placing longer stents might prove technically more challenging and might increase the risk on in-stent restenosis and stent thrombosis, even in drug eluting stents [6]. For this reason, determining an optimal stent-landing zone is critical for the prevention of future stent-related adverse events.

An optimal stent-landing zone is a region without lipids and a $\text{PB}<40\%$. In contrast to IVUS, OCT is capable of detecting lipids, but the limited penetration depth hampers PB measurements. OCT can reliably detect the healthy vessel wall, however. Therefore, we wanted to investigate if the presence of a normal wall is helpful to predict PB by OCT. This study showed that a measurement of the PFW angle provides a reliable estimate of the PB, without the need to fully visualize the outer wall of the vessel and together with the fact that OCT is one of the most reliable techniques to structurally assess the presence of a vulnerable plaque [7,8].

The detection of the PFW in OCT can be influenced by the composition of the intima. Plaque components like a lipid/necrotic core and sites of inflammatory activity cause high attenuation and may obscure the vessel wall layers, even in a relatively thin intima. Plaque-free regions ($\text{IMT}<0.5\text{mm}$) with a superficial layer of macrophages or foam cells (intimal xanthoma) can appear as regions with plaque, since the healthy 3-layered structure of the vessel is not visible. This leads to underestimation of the PFW angle and thus overestimation of the plaque burden. The confounding effect of vessel wall composition may explain why the association between PFW_{OCT} and PB almost vanishes in the more diseased sections. We observe a similar trend in the relation between PFW_{IVUS} and PB, although the detection of the PFW by IVUS is usually not affected by attenuation-inducing plaque components, indicating a possible biological phenomenon. In the initial stages of plaque growth, the asymmetric plaque growth results in a simultaneously decreasing PFW angle and increasing PB. Apparently in later stages, the plaque growth becomes more symmetrical, decreasing the PFW angle with only a limited increase in PB and thus weakening the relationship. This explanation should be supported by serial imaging studies.

PCI procedures are always guided by angiography to determine catheter position and lumen narrowing. Currently, it is challenging to identify segments seen on OCT with the corresponding location on angiography which could lead to wrong sizing and positioning of the stent. The recently introduced on-line co-registration of OCT and angiography [9] it may be challenging to identify corresponding

segments between intracoronary imaging and angiography. Computer based online co-registration may aid the target segment identification.

METHODS: The DOCTOR fusion study was a prospective, single arm, observational study including patients admitted for elective PCI. Optical coherence tomography (OCT) could greatly increase the utility of OCT and thereby the application of our findings in the clinical work flow. The most predictive cut-off angle of 220° PFW is hard to determine by eye. This might limit direct clinical application of our findings. New software for the automatic detection of the three wall layers and the determination of the PFW angle is under development in our university.

8.4.1 | Limitations

Some limitations in our study should be taken into account. Despite the use of side branches for optimal matching of OCT and IVUS pullbacks, errors in matching can occur due to intrinsic differences between the two techniques. These include, amongst others, pull back speed, lateral resolution and frame rate. To minimize the impact of these mismatches on the accuracy of the results, the measurements were averaged over a region of 3 mm, which is a larger than the maximum expected longitudinal mismatch. Furthermore, a number of frames were excluded in the proximal regions of the pullbacks due to bad flush or when the vessel wall was out of view.

Only a limited number of matched pullbacks were available for analysis. Since we analyzed the IVUS images per cross-section and not longitudinally, we regarded the 7 data points per pull-back as separate observations. However, these results should still be interpreted as being a proof-of-principle study. We do not expect that our conclusion would be much different with a larger dataset.

8.5 | Conclusion

In conclusion, this study shows that PFW_{OCT} is a good predictor for the PB and gives more insight in the general interpretation of PFW_{OCT} angles. After further clinical validation, this new plaque burden estimation based on OCT could help to identify the optimal landing zone.

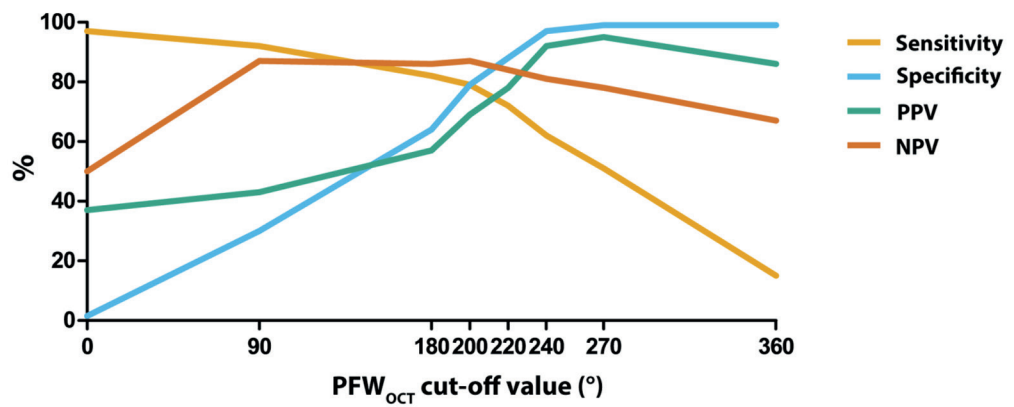
8.6 | Ethical standards

Informed consent was obtained from each patient and the study protocol conforms to the ethical guidelines of the 1975 Declaration of Helsinki as reflected in a priori approval by the institution's human research committee.

References

1. Tearney GJ, Regar E, Akasaka T, et al. (2012) Consensus standards for acquisition, measurement, and reporting of intravascular optical coherence tomography studies: a report from the International Working Group for Intravascular Optical Coherence Tomography Standardization and Validation. *J Am Coll Cardiol* 59:1058–72. doi: 10.1016/j.jacc.2011.09.079
2. Glagov S, Weisenberg E, Zarins CK, et al. (1987) Compensatory Enlargement of Human Atherosclerotic Coronary Arteries. *N Engl J Med* 22:1371–1375.
3. van Soest G, Goderie T, Regar E, et al. Atherosclerotic tissue characterization in vivo by optical coherence tomography attenuation imaging. *J Biomed Opt* 15:011105. doi: 10.1117/1.3280271
4. Gogas BD, Garcia-Garcia HM, Onuma Y, et al. (2013) Edge vascular response after percutaneous coronary intervention: an intracoronary ultrasound and optical coherence tomography appraisal: from radioactive platforms to first- and second-generation drug-eluting stents and bioresorbable scaffolds. *JACC Cardiovasc Interv* 6:211–21. doi: 10.1016/j.jcin.2013.01.132
5. Wentzel JJ, Gijsen FJH, van der Giessen R, et al. (2014) Positive remodeling at 3 year follow up is associated with plaque-free coronary wall segment at baseline: a serial IVUS study. *Atherosclerosis* 236:82–90. doi: 10.1016/j.atherosclerosis.2014.06.013
6. Teirstein PS (2010) Drug-eluting stent restenosis: an uncommon yet pervasive problem. *Circulation* 122:5–7. doi: 10.1161/CIRCULATIONAHA.110.962423
7. Prati F, Romagnoli E, Burzotta F, et al. (2015) Clinical Impact of OCT Findings During PCI: The CLI-OPCI II Study. *JACC Cardiovasc Imaging* 8:1297–305. doi: 10.1016/j.jcmg.2015.08.013
8. Kini AS, Motoyama S, Vengrenyuk Y, et al. (2015) Multimodality Intravascular Imaging to Predict Periprocedural Myocardial Infarction During Percutaneous Coronary Intervention. *JACC Cardiovasc Interv* 8:937–45. doi: 10.1016/j.jcin.2015.03.016
9. Hebsgaard L, Nielsen TM, Tu S, et al. (2015) Co-registration of optical coherence tomography and X-ray angiography in percutaneous coronary intervention. the Does Optical Coherence Tomography Optimize Revascularization (DOCTOR) fusion study. *Int J Cardiol* 182:272–8. doi: 10.1016/j.ijcard.2014.12.088

Supplementary figure



Supplementary figure 8.1 | Sensitivity, specificity, PPV and NPV values for different PFW angle cut-off points to predict a PB<40%. The optimal cut-off point is set at 220° PFW.

Chapter 9

General discussion

Intravascular OCT has demonstrated to be a powerful tool for diagnostic imaging in coronary atherosclerosis. Quantification of the OCT images for characterization of the atherosclerotic tissue types and validating the method was the scope of this thesis. The attenuation coefficient is one such parameter of the OCT signal, which can be quantified and is tissue dependent. Correlation between attenuation imaging of OCT and tissue types has been studied previously [1,2]. In this thesis we did ex-vivo and in-vivo validation of attenuation imaging as a tissue characterization tool and demonstrated some of its clinical research utilities.

En-face attenuation maps

In the second chapter we introduced an analysis method that is robust against common registration errors. The OCT pullback has a disadvantage of large frame pitch ($200\text{ }\mu\text{m}$) that can make it difficult to find the same cross section accurately represented by a $3\text{ }\mu\text{m}$ thick histology section in a vessel, or to register an independent invasive imaging data set to that degree of precision. To overcome this sampling problem, we constructed a longitudinal representation of the pullback to make quantitative comparisons [3]. This is an improvement over the analysis in cross section images as the map depicts tissue features as a whole, along the vessel. This representation also allows for non-rigid registration to correct for non-uniform rotation and variations in effective pullback speed (due to cardiac motion in vivo).

The map was constructed by sampling a user specified depth window for the average or maximum value of attenuation from the lumen border. The drawback of this longitudinal representation is that it is a two-dimensional cross section through a three-dimensional data set, hence sacrifices depth resolution. For detailed analyses, several longitudinal maps at different depths from the lumen boundary can be extracted.

We studied the effects of temperature and tissue fixation on the optical properties specifically the attenuation coefficient of the tissue properties. Ex-vivo validation is an essential step for any new OCT analysis methods, it is important to know how common tissue preparation steps affect the parameters that can be quantified from the OCT images. We observed very small differences induced by temperature and fixation: relative to unfixed tissue at 37°C (close to body temperature conditions), the attenuation coefficient differs by a few percent at most in other conditions.

Index of Plaque attenuation

Based on this en-face attenuation map, we defined an Index of Plaque Attenuation (IPA) in Chapter 3 to quantify the parametric attenuation image. IPA is the ratio of the number of pixels in the attenuation map or a segment of it with an attenuation coefficient greater than a certain threshold x to the total number of pixels, multiplied by a factor of 1000.

We studied the ability of the index of plaque attenuation (IPA), a bias free and reproducible summary measurement of attenuating tissue types, as a lipid-core detection tool. The results show that the OCT-derived index, the $IPA_{8.5}$, have a significant correlation with the manual lipid score in OCT images, which enables automation of the coronary plaque lipid assessment by OCT. Lipid scoring in OCT for clinical research is a time consuming process, where frame-by-frame analysis and measurement is required. The correlation between $IPA_{8.5}$ and manual lipid measurements is significantly higher than the correlation between the lipid score by OCT to automated indices like the near-infrared spectroscopy (NIRS)-based Lipid Core Burden Index (LCBI) [4]. The detection mechanisms of the two modalities and the frame spacing might explain the variability between OCT and NIRS.

The IPA has the potential as a clinical tool as it can indicate the presence and location of lipid rich plaques in an entire vessel. It is the result of automatic computation of plaque attenuation, hence provides an alternative to manual scoring in cardiovascular research. IPA could be displayed as a color-coded block along the vessel indicating probable lipid core. IPA, being an index calculated from a physical parameter, is robust and reproducible.

The study also showed that the thick cap fibroatheroma usually contains variable amount of lipid content that can contribute to attenuation among other components. Hence varying range of IPA values were observed for them. On the contrary the thin cap fibroatheroma which is also typically characterized by dense macrophage infiltration exhibited high IPA. Also the pathological intimal thickenings (PITs) with macrophage exhibited high IPA values even though pathological evidence of lipid was not available. The gap between the PITs with and without macrophages was very significant. PITs without macrophages or lipid droplets and fibrotic plaques had almost zero value for IPA.

Clinical study

In Chapter 4, a study is described that aimed to validate optical attenuation as a plaque characterization tool in vivo. The main finding of the single-center clinical study was that the fraction of image pixels with optical attenuation greater than 11 mm^{-1} (IPA_{11}), can reliably differentiate between thin and thick cap fibroatheroma and is superior compared to LCBI for making this distinction. This discrimination is facilitated by deeper-lying lipids that exhibit reduced attenuation in OCT images. The limited specificity of optical attenuation in overall lipid detection results in a modest correlation between IPA and LCBI. Fibrocalcific plaques in the dataset also had higher IPA and LCBI values suggesting the presence of lipid. The IPA values of TCFA are significantly higher than the fibrocalcific plaques.

The ability of the automatically computed attenuation coefficient to highlight the presence of TCFA in a complete pullback makes it a tool with potential clinical utility. After appropriate validation, IPA analysis may replace the time-consuming and laborious manual measurements. OCT-derived IPA_{11} may be a feasible method to detect LCP with a thin cap, an important indicator for plaque instability [5]. In a clinical application, realistic implementation would include automatic media segmentation, after which

the attenuation analysis can be overlaid on the OCT images. The en-face map display and colour coded IPA_{11} displayed on the longitudinal section (similar to the block chemogram used in NIRS), would enable direct overall assessment of plaque in the artery to guide revascularization procedures.

Comparison of tissue characterization methods

In chapter 5 we qualitatively compared some of the available methods for OCT tissue characterization. Algorithmic OCT tissue type characterization can provide a valuable metric for automated assessment of the extent and severity of atherosclerotic coronary artery disease. The different methodologies were performed on a set of ex-vivo data and compared with the histological annotations by skilled pathologists. Each of the methods of OCT tissue characterization compared, has value as an atherosclerotic tissue component detection tool and could play a significant role in the assessment of the stability of the plaque.

The first few sections of the thesis described the validation of the tissue characterization method using optical attenuation ex and in-vivo. The next few sections show its potential as a clinical research tool in stent follow up and plaque progression studies.

Biovascular scaffold follow-up study

In Chapter 6 we present the first in-vivo long-term OCT data 5 years after BVS implantation. The study included some of the first patients treated with BVS, offering a unique opportunity to study the long-term vascular response after BVS implantation despite small size. Our main findings are that there is late lumen enlargement and all struts have disappeared and been integrated within the neointima. The underlying plaque formed a signal-rich, low-attenuating ‘sealing layer’, while in one exceptional case, thinning and disruption of the ‘sealing layer’ was observed. Metal drug eluting stents in the same vessels are lacking a distinct ‘sealing layer’ and show neoatherosclerosis despite good coverage and apposition.

We observed a consistent luminal enlargement and a recovery of the luminal symmetry from 2 to 5 years in all patients. Our hypothesis is that simultaneous observations of strut bioresorption and ‘sealing layer’ development suggest a potentially favourable biological effect. Based on the suggestion that BVS implantation could induce morphological changes causing a ‘plaque sealing’ or ‘recapping the plaque’ we scrutinized the BVS morphology in our cohort, employing sophisticated algorithms for in-depth analysis.

We focused on the newly formed adluminal signal-rich layer, which we defined as ‘sealing layer’, which could reliably protect the lumen from thrombogenic plaque components. In attenuation analysis the ‘sealing layer’ appears homogeneous with low attenuation, suggesting absence of high-risk wall components such as necrotic core and macrophages [1,6]. Therefore we assume that the sealing layer can be protective against very late scaffold thrombosis or de novo thrombosis by plaque progression and rupture [7,8].

The complete scaffold integration into the vascular wall has shaped a ‘neo-plaque’ phenotype which we visually characterized using standardized OCT criteria [9]. Quantitative attenuation analysis also depicts these necrotic core regions with high attenuation. High attenuation regions were generally located deeper into the vessel wall. In contrast, metal drug-eluting stents in our cohort showed marked adluminal neoatherosclerosis, with significantly thinner cap.

Plaque progression

In Chapter 7, we performed comprehensive patient-level and segment-level OCT analyses of non-culprit plaque morphology in order to evaluate the dynamic changes of coronary atherosclerosis under standard medical therapy. We also performed quantitative attenuation analysis in order to corroborate findings from plaque characterization. In patients with coronary artery disease under standard medical therapy, plaque morphology changes over time in a high percentage of cases. High differences between individual patients and segments were observed with some demonstrating plaque stabilization and others plaque destabilization rather than significant entire cohort differences. Even in the cohort, modest thickening was observed. These changes are rarely accompanied by clinical manifestations. Prediction of these changes from clinical factors and based on their initial morphology is poor.

For short follow-up intervals, fibrous plaques are relatively stable plaque types while fibroatheromas and TCFAs are prone to dynamic changes including both lesion stabilization and destabilization. Over time, both plaque types could potentially progress to a culprit lesion, an observation supported by the finding of plaque rupture also in fibroatheromas with thicker caps [10,11].

Fibrous cap thickness is a major determinant of plaque vulnerability [8]. In our study, on a segment level, minimum and average cap thickness increased from baseline to follow-up but a non-negligible percentage of segments were presented with fibrous cap thinning. This suggests medical therapy can promote plaque stabilization but this effect is not universal, and local therapies could be considered[12]. Our study also suggests morphological plaque changes are highly localized and are observed on individual plaque level rather than on patient level.

We used automated attenuation analysis to study objectively the plaque morphology. High attenuation has been associated with high-risk plaque characteristics such as necrotic core and macrophages [1]. The results of this analysis were in line with traditional OCT plaque characterization showing increasing values of attenuation indexes from fibrous to fibroatheroma to TCFA. Furthermore, the observations of strong correlations of these indexes with increased necrotic core content and reduced cap thickness suggest that an automated analysis could be employed for monitoring of the dynamic changes in plaque morphology.

Registration of OCT and IVUS

In Chapter 8 we studied the relationship between the plaque free wall (PFW) measured in OCT and the plaque burden (PB) measured in the IVUS. This study shows for the first time that PFW angle in OCT can be considered as a surrogate marker for PB, which is currently a common criterion to determine stent-landing zone. The registration of IVUS and OCT was an essential part of the comparison. An in-house registration tool with GUI was developed where physical landmarks like the side branches in the vessel pullbacks from both modalities can be selected and used as control points for registration. Plaque burden and plaque free wall measurements in IVUS are quite common but the detection of the PFW in OCT can be influenced by the presence of plaque components like calcium, macrophages and a lipid/necrotic core, which cause high attenuation. Even a thin layer of highly attenuating macrophage infiltration or lipids can appear similar to an unstable plaque due to the absence of the layered structure of the vessel. This could lead to underestimation of the PFW angle and thus overestimation of the plaque burden. This could explain why the relationship between PFW_{OCT} and PB is very limited in the more diseased sections. The results show that this attenuation effect would not influence the prediction of an optimal stent-landing zone.

One of the downside of the OCT is the penetration depth especially in plaque rich region, which makes it a difficult candidate for PB measurements. We showed that, by looking at the PFW angle, a reliable estimation can be made of the plaque burden without the need to fully visualize the outer wall of the vessel. Apart from the plaque burden, the plaque characteristics play a major role determining stent-landing zone. OCT is currently one of the most reliable techniques to structurally assess the presence of a vulnerable plaque [13] which adds to the reliability and applicability of this technique in PCI procedures.

Outlook

The en-face attenuation maps and IPA, which are the results of automatic computation of plaque attenuation, have the potential as clinical tools as they can indicate the presence and location of lipid rich plaques in an entire pullback, and provides an alternative to manual scoring in cardiovascular research. IPA could be displayed as a color-coded block along the vessel indicating probable lipid core plaques. The utility of such a tool would need to be evaluated in a dedicated study enrolling a larger group of patients. Also extensive ex-vivo studies are needed to establish the correlation of attenuation with more tissue types. Application to large data sets will be facilitated by automated media segmentation, a tool that is currently being developed in our institute [14].

The BVS follow-up study depicted a very good correlation between the manually segmented plaques and the plaques identified by attenuation maps adding strength to its potential clinical utility. The study was conducted in the first few BVS implanted patients and was a single centered. A more detailed and dedicated follow-up study is needed to evaluate the hypothesis developed from this limited scope study.

In our study of the progression of non-culprit segment atherosclerosis, a comprehensive analysis of plaque morphology was performed and further corroborated by quantitative attenuation analysis. This required matching of sub-segments in baseline and follow-up OCT pullbacks. The frame spacing of the commercial OCTs are relatively high which makes the matching very difficult. Currently a very high speed and high resolution OCT is being developed in our institute that has a very significantly low frame spacing. Attenuation analysis on the pullbacks of the OCT system can result in a more accurately matched dataset.

PCI procedures are always done with angiographical guidance to determine catheter position and lumen narrowing. Registering OCT data to angiography is a challenging task, which could lead to wrong sizing and positioning of the stent. The recently developed co-registration software for OCT and angiography [9] it may be challenging to identify corresponding segments between intracoronary imaging and angiography. Computer based online co-registration may aid the target segment identification.

METHODS: The DOCTOR fusion study was a prospective, single arm, observational study including patients admitted for elective PCI. Optical coherence tomography (OCT) could greatly reduce this risk and increases the utility of our findings.

Moreover, manually measuring the cut-off value of 220° PFW is hard, which limits the direct clinical application. New software for the automatic detection of the three wall layers and the determination of the PFW angle is under development in our university [14]. This software would greatly increase the clinical value of our findings.

References

1. G. van Soest, T. Goderie, E. Regar, S. Koljenovic, G. L. van Leenders, N. Gonzalo, S. van Noorden, T. Okamura, B. E. Bouma, G. J. Tearney, J. W. Oosterhuis, P. W. Serruys, and A. F. van der Steen, "Atherosclerotic tissue characterization in vivo by optical coherence tomography attenuation imaging," *J Biomed Opt* 15, 011105 (2010).
2. F. J. van der Meer, D. J. Faber, D. M. Baraznji Sassoon, M. C. Aalders, G. Pasterkamp, and T. G. van Leeuwen, "Localized measurement of optical attenuation coefficients of atherosclerotic plaque constituents by quantitative optical coherence tomography," *IEEE Trans Med Imaging* 24, 1369-1376 (2005).
3. M. Gnanadesigan, G. van Soest, S. White, S. Scoltock, G. J. Ughi, A. Baumbach, A. F. van der Steen, E. Regar, and T. W. Johnson, "Effect of temperature and fixation on the optical properties of atherosclerotic tissue: a validation study of an ex-vivo whole heart cadaveric model," *Biomed Opt Express* 5, 1038-1049 (2014).
4. T. Yonetsu, W. Suh, F. Abtahian, K. Kato, R. Vergallo, S. J. Kim, H. Jia, I. McNulty, H. Lee, and I. K. Jang, "Comparison of near-infrared spectroscopy and optical coherence tomography for detection of lipid," *Catheter Cardiovasc Interv* 84, 710-717 (2014).
5. R. Virmani, F. D. Kolodgie, A. P. Burke, A. Farb, and S. M. Schwartz, "Lessons From Sudden Coronary Death : A Comprehensive Morphological Classification Scheme for Atherosclerotic Lesions," *Arteriosclerosis, thrombosis, and vascular biology* 20, 1262-1275 (2000).
6. G. J. Ughi, T. Adriaenssens, P. Sinnaeve, W. Desmet, and J. D'Hooge, "Automated tissue characterization of in vivo atherosclerotic plaques by intravascular optical coherence tomography images," *Biomed Opt Express* 4, 1014-1030 (2013).
7. A. Karanasos, J. Ligthart, K. Witberg, K. Toutouzas, J. Daemen, G. van Soest, M. Gnanadesigan, R.-J. van Geuns, P. de Jaegere, and E. Regar, "Association of neointimal morphology by optical coherence tomography with rupture of neoatherosclerotic plaque very late after coronary stent implantation," in *SPIE conference proceedings*(2013), pp. 856542-856542-856513.
8. R. Virmani, A. P. Burke, A. Farb, and F. D. Kolodgie, "Pathology of the vulnerable plaque," *Journal of the American College of Cardiology* 47, C13-18 (2006).
9. G. J. Tearney, E. Regar, T. Akasaka, T. Adriaenssens, P. Barlis, H. G. Bezerra, B. Bouma, N. Bruining, J.-m. Cho, S. Chowdhary, M. A. Costa, R. de Silva, J. Dijkstra, C. Di Mario, D. Dudeck, E. Falk, M. D. Feldman, P. Fitzgerald, H. Garcia, N. Gonzalo, J. F. Granada, G. Guagliumi, N. R. Holm, Y. Honda, F. Ikeno, M. Kawasaki, J. Kochman, L. Koltowski, T. Kubo, T. Kume, H. Kyono, C. C. S. Lam, G. Lamouche, D. P. Lee, M. B. Leon, A. Maehara, O. Manfrini, G. S. Mintz, K. Mizuno, M.-a. Morel, S. Nadkarni, H. Okura, H. Otake, A. Pietrasik, F. Prati, L. Räber, M. D. Radu, J. Rieber, M. Riga, A. Rollins, M. Rosenberg, V. Sirbu, P. W. J. C. Serruys, K. Shimada, T. Shinke, J. Shite, E. Siegel, S. Sonada, M. Suter, S. Takarada, A. Tanaka, M. Terashima, T. Troels, S. Uemura, G. J. Ughi, H. M. M. van Beusekom, A. F. W. van der Steen, G.-A. van Es, G. van Soest, R. Virmani, S. Waxman, N. J. Weissman, and G. Weisz, "Consensus Standards for Acquisition, Measurement, and Reporting of Intravascular Optical Coherence Tomography Studies: A Report From the International Working Group for Intravascular Optical Coherence Tomography Standardization and Validation," *Journal of the American College of Cardiology* 59, 1058-1072 (2012).
10. K. Toutouzas, A. Karanasos, E. Tsiamis, M. Riga, M. Drakopoulou, A. Synetos, A. Papanikolaou, C. Tsioufis, A. Androulakis, E. Stefanadi, D. Tousoulis, and C. Stefanadis, "New insights by optical coherence tomography into the differences and similarities of culprit ruptured plaque morphology in non-ST-elevation myocardial infarction and ST-elevation myocardial infarction," *Am Heart J* 161, 1192-1199 (2011).
11. K. Toutouzas, E. Tsiamis, A. Karanasos, M. Drakopoulou, A. Synetos, C. Tsioufis, D. Tousoulis, P. Davlouros, D. Alexopoulos, K. Bouki, T. Apostolou, and C. Stefanadis, "Morphological characteristics of culprit atheromatic plaque are associated with coronary flow after thrombolytic therapy: new implications of optical coherence tomography from a multicenter study," *JACC Cardiovasc Interv* 3, 507-514 (2010).
12. A. Karanasos, C. Simsek, M. Gnanadesigan, N. S. van Ditzhuijzen, R. Freire, J. Dijkstra, S. Tu, N. Van Mieghem, G. van Soest, P. de Jaegere, P. W. Serruys, F. Zijlstra, R. J. van Geuns, and E. Regar, "OCT assessment of the long-term vascular healing response 5 years after everolimus-eluting bioresorbable vascular scaffold," *J Am Coll Cardiol* 64, 2343-2356 (2014).

13. B. D. MacNeill, H. C. Lowe, M. Takano, V. Fuster, and I. K. Jang, "Intravascular modalities for detection of vulnerable plaque: current status," *Arterioscler Thromb Vasc Biol* 23, 1333-1342 (2003).
14. G. Zahnd, A. Karanasos, G. van Soest, E. Regar, W. Niessen, F. Gijsen, and T. van Walsum, "Quantification of fibrous cap thickness in intracoronary optical coherence tomography with a contour segmentation method based on dynamic programming," *Int J Comput Assist Radiol Surg* 10, 1383-1394 (2015).

Summary

Intravascular OCT is a popular tool for PCI guidance and diagnostic imaging. Atherosclerosis is a progressive disease of the arterial wall and the sudden rupture of an unstable lipid rich plaque causes acute myocardial infarction. The tissue composition of the atherosclerotic plaque is a major factor for its instability. Quantification of optical parameters in OCT images can be a tool for atherosclerotic tissue characterization. The attenuation coefficient, a tissue dependent parameter of the OCT has been demonstrated to have good correlation with tissue types.

Within the scope of this thesis we did ex and in-vivo validation of attenuation imaging as a tissue characterization tool and demonstrated some of its clinical research utilities.

In **Chapter 2** we studied the effect of temperature and fixation on the attenuation coefficient of tissue properties. We compared the en-face attenuation maps at different conditions. The results show that the tissue fixation and temperature do not systematically affect the optical attenuation properties of the tissues.

Chapter 3 is an ex-vivo study where we introduced an index of plaque attenuation (IPA) based on the en-face attenuation maps. We studied the potential of IPA as a lipid detection tool. The results show that the IPA has a correlation with manual lipid scores and hence has the potential to adequately replace laborious and time-consuming manual measurements.

In **Chapter 4** we describe a clinical study that aimed to validate attenuation imaging as a plaque characterization tool in vivo. The study showed that IPA can significantly differentiate thin and thick cap fibroatheroma.

In **Chapter 5** we qualitatively compared some of the available methods for OCT tissue characterization. The algorithms were used to analyze an ex-vivo data set and compared with the histological tissue type characterization. The methods included in this study all have assets that make them valuable contributions to the image analysis toolbox in clinical OCT imaging.

In **Chapter 6** we present the first in-vivo long-term OCT data 5 years after BVS implantation. The attenuation maps and IPA prove to be potential clinical research tools depicting plaque ‘passivation’, including the formation of a potentially protective ‘sealing layer’ in the long-term BVS follow-up.

In **Chapter 7**, we performed comprehensive patient-level and segment-level OCT analyses of non-culprit plaque morphology in order to evaluate the dynamic changes of coronary atherosclerosis under standard medical therapy. We also performed quantitative attenuation analysis in order to corroborate findings from plaque characterization. The study show a good relation between plaque changes and

tissue type identified by attenuation. IPA is not an independent predictor but is correlated with plaque type, which does relate to change.

We studied the relationship between the plaque free wall (PFW) measured in OCT and the plaque burden (PB) measured in the IVUS in Chapter 8. OCT measured PFW angle is a good predictor for the PB and hence increasing the feasibility to use an OCT catheter only, instead of the combination with IVUS during a stenting procedure, reducing patient risk, procedure length and costs.

Samenvatting

Intravasculaire OCT is een populair hulpmiddel tijdens het sturen van PCI's en voor diagnostische beeldvorming. Atherosclerose is een progressieve ziekte van de vaatwand en het plotseling scheuren van een onstabiele lipide-rijke plaque veroorzaakt myocardiale infarctering. De weefselsamenstelling van de atherosclerotische plaque is een grote factor voor zijn instabiliteit. Het kwantificeren van optische parameters in OCT-beelden kan een methode zijn voor atherosclerotische plaque typering. De verzwakkingscoëfficiënt, een weefselafhankelijke parameter van OCT, is een bewezen goede afspiegeling van weefsel types.

Binnen het kader van deze thesis hebben we ex- en in-vivo validatie van verzwakkingsbeeldvorming als een weefseltyperingsmethode uitgevoerd en hebben enkele klinische toepassingen aangetoond.

In **hoofdstuk 2** hebben we het effect van temperatuur en fixatie op de verzwakkingscoëfficiënt van weefseleigenschappen bestudeerd. We vergeleken de 'en-face' verzwakkingskaarten onder verschillende omstandigheden. De resultaten laten zien dat weefselfixatie en temperatuur geen systematische invloed hebben op de optische verzwakkingseigenschappen van weefsel.

Hoofdstuk 3 is een ex-vivo studie waar we een index van plaque verzwakking (IPA) gebaseerd op 'en-face' verzwakkingskaarten hebben geïntroduceerd. We bestuurden de potentie van IPA als een lipiden detectiemethode. De resultaten laten zien dat de IPA een correlatie heeft met handmatig uitgevoerde lipide scores en dus de potentie heeft om intensieve en tijdrovende handmatige metingen te vervangen.

In **hoofdstuk 4** beschrijven we een klinische studie die beoogde om verzwakkingsbeeldvorming als plaque typering in-vivo te valideren. De studie laat zien dat IPA op een significante manier kan differentiëren tussen een dunne en dikke kap fibroatheroom.

In **hoofdstuk 5** hebben we op kwalitatieve manier de beschikbare methodes van OCT-weefseltypering vergeleken. De algoritmen werden gebruikt om ex-vivo data te analyseren en werden vergeleken met histologische weefseltypering. De getoetste methodes in deze studie hebben allemaal eigenschappen die waardevolle toevoegingen kunnen zijn voor het analyseren van beelden bij het gebruik van OCT in de klinische praktijk.

In **hoofdstuk 6** presenteren we de eerste lange-termijn in-vivo OCT- data 5 jaar na BVS-implantatie. De verzwakkingskaarten en IPA bleken potentiële klinische onderzoeksmethoden die plaque passiviteit kunnen aantonen, inclusief de formatie van een potentiële beschermende 'sealing layer' tijdens de lange-termijn BVS follow-up.

In **hoofdstuk 7**, voerden we een uitgebreide OCT-analyse uit op patiënt-niveau en segment-niveau van ‘non-culprit’ plaque morfologie, om zo de dynamische veranderingen van coronaire atherosclerose onder standaard medische therapie te evalueren. We hebben ook een kwantitatieve verzwakkingsanalyse gedaan om de bevindingen van de plaque typering te bevestigen. De studie liet een goede relatie tussen plaque veranderingen en weefsel type, geïdentificeerd door verzwakking, zien. IPA is niet een onafhankelijke voorspeller, maar is gecorreleerd met plaque type, welke in relatie staat met verandering.

We bestuurden de relatie tussen plaque-vrije vaatwand (PFW), gemeten op OCT-beelden, en de plaque grootte (PB), gemeten op IVUS-beelden, in **hoofdstuk 8**. PFW-hoek gemeten door OCT is een goede voorspeller voor de PB en verhoogd dus de haalbaarheid van het gebruik van alleen OCT-katheters, in plaats van een combinatie met IVUS tijdens een stent procedure. Hiermee kunnen het risico voor de patiënt, de lengte van de procedure en de kosten worden teruggebracht.

Acknowledgements

I would like to gratefully acknowledge various people who have journeyed with me throughout this thesis work. First, I would like to thank Gijs for giving me an opportunity to work on this thesis and for the supervision and encouragement during the project. Also I am grateful to Ton for giving me the opportunity, enormous support and valuable suggestions.

Secondly, I would like to thank all my colleagues who made my time in the department a delight. I have to mention Tianshi and Pieter who have been a constant source of joy through the struggles and trials of this thesis. Also I have to thank Evelyn, Antonis, Jors and Nienke from Thorax center, Erasmus MC for the valuable discussions and contributions to this thesis. I would also like to thank Heleen and Jan for their valuable inputs and contributions. I am gratefully thankful to Jorgen, Karen and all the technicians of the Thorax center for their help and contributions in the clinical study.

Next I would like to thank all my friends in Rotterdam who made my life easy and joyful. Thank you Mahipal, Saravanan, Deep, Prakash and Vinay for all the time spent and the trips taken together.

Finally I would like to thank my parents for their unending love and support and my wife, Vidya, for her love and support.

Curriculum Vitae



Muthukaruppan Gnanadesigan was born on January 21, 1985 in Palayamkottai, India. He did his Bachelors of technology in Biomedical instrumentation from Dr. M.G.R University, Chennai, India. He was awarded 'First class with honours' degree and gold medal. After obtaining bachelor's degree he completed Masters in Biomedical engineering from Hochschule Furtwangen University, Germany. In 2011, he joined the biomedical engineering department of thorax center, ErasmusMC as a PhD researcher in the project 'Atherosclerotic tissue type imaging'.

Publications

Gnanadesigan M, van Soest G, White S, Scoltock S, Ughi GJ, Baumbach A, van der Steen AFW, Regar E, Johnson TW. “Effect of temperature and fixation on the optical properties of atherosclerotic tissue: a validation study of an ex-vivo whole heart cadaveric model”. *Biomedical optics express* 2014; 5:1038-1049.

Muthukaruppan Gnanadesigan, Ali S Hussain, Stephen White, Simon Scoltock, Andreas Baumbach, Antonius FW van der Steen, Evelyn Regar, Thomas W Johnson, and Gijs van Soest. “Optical coherence tomography attenuation imaging for lipid core detection: an ex-vivo validation study”. *The International journal of Cardiovascular Imaging* 2016, *accepted*.

M. Gnanadesigan, T. Kameyama, Antonios Karanasos, N. S. van Ditzhuijzen, J. van der Sijde, MD¹, R.J. van Geuns, Jurgen Ligthart, Karen Witberg, Giovanni J. Ughi, A.F.W. van der Steen, E. Regar, and G. van Soest. “Automated characterization of lipid-core plaques in vivo by quantitative optical coherence tomography tissue type imaging” *EuroIntervention* 2016, *accepted*.

Muthukaruppan Gnanadesigan, Steve White, Giovanni Ughi, Lambros Athanasiou, Taylor Hoyt, Jan van der Thüsen, Heleen van Beusekom, Thomas W Johnson, Dimitrios Fotiadis, Jeniffer Phipps, Marc Feldman, Gary Tearney and Antonius FW van der Steen, Gijs van Soest. “Qualitative comparison of automated tissue characterization methods in intravascular optical coherence tomography ex-vivo” *Manuscript in preparation*.

Antonios Karanasos, Cihan Simsek, **Muthukaruppan Gnanadesigan**, Nienke S van Ditzhuijzen, Raphael Freire, Jouke Dijkstra, Shengxian Tu, Nicolas Van Mieghem, Gijs van Soest, Peter de Jaegere, Patrick W Serruys, Felix Zijlstra, Robert-Jan van Geuns, Evelyn Regar. “OCT Assessment of the Long-Term Vascular Healing Response 5 Years After Everolimus-Eluting Bioresorbable Vascular Scaffold” *J Am Coll Cardiol* **64**, 2343-2356 (2014).

Bu-Chun Zhang, Antonios Karanasos, **Muthukaruppan Gnanadesigan**, Johannes N van der Sijde, Nienke S van Ditzhuijzen, Karen T Witberg, Jurgen MR Ligthart, Roberto Diletti, Robert-Jan van Geuns, Jouke Dijkstra, Felix Zijlstra, Gijs van Soest, Evelyn Regar. “Qualitative and quantitative evaluation of dynamic changes in non-culprit coronary atherosclerotic lesion morphology. A longitudinal OCT study”. *Submitted*.

Ayla Hoogendoorn, **Muthukaruppan Gnanadesigan**, Guillaume Zahnd, Nienke S. van Ditzhuijzen, Johan C. H. Schuurbiers, Gijs van Soest, Evelyn Regar, Jolanda J. Wentzel. “OCT-measured plaque free wall angle is indicative for plaque burden: overcoming the main limitation of OCT?”. *Submitted*.

Regar E, **Gnanadesigan M**, Van der Steen AF, van Soest G. Quantitative optical coherence tomography tissue-type imaging for lipid-core plaque detection. *JACC Cardiovasc Interv* 2013; 6:891-892.

T. W. Johnson, S. White, **M. Gnanadesigan**, H. Bourenane, J. W. Strange, A. C. Newby, G. van Soest, and A. Baumbach, “An ex-vivo “whole human heart model” for the development of intravascular imaging,” *Heart* 98, 15-A16 (2012).

PhD Portfolio

PhD training	Year	ECTS
<i>General and specific courses</i>		
• Biomedical English Writing	2014	4.0
• Vascular Biology, NHS, Papendal	2013	3.8
• Tissue Optics, SPIE photonics West	2012	0.3
• OCT Principles, SPIE Photonics West	2013	0.3
• Photoshop and illustrator workshop, MolMed	2014	0.3
<i>Presentations</i>		
• Oral presentation – 2013 BioS, SPIE Photonics West	2013	2.0
• Oral presentation – 2015 BioS, SPIE Photonics West	2015	2.0
• Poster presentation – 2014 BioS, SPIE Photonics West	2014	1.8
• Oral presentation – 2015 ABP, Yokohama, Japan	2015	2.0
• Oral presentation – 2015 ECBO, Munich, Germany	2015	2.0
• Poster presentation – 2013 Optics in Cardiology	2013	1.4
• Poster presentation – 2015 Optics in Cardiology	2015	1.4
<i>International conference attendance</i>		
• 2012 BioS, Photonics West, San Francisco, U.S.A	2012	1.8
• 2013 BioS, Photonics West, San Francisco, U.S.A	2013	1.8
• 2014 BioS, Photonics West, San Francisco, U.S.A	2014	1.8
• 2015 BioS, Photonics West, San Francisco, U.S.A	2015	1.8
• European conference on Biomedical Optics, Munich, Germany	2015	1.4
• APBP conference, Yokohama, Japan	2015	1.8
Total ECTS	31.7	

